DENSIFICATION BEHAVIOR OF CERAMIC AND CRYSTALLIZABLE GLASS MATERIALS CONSTRAINED ON A RIGID SUBSTRATE

Jesus N. Calata

Dissertation submitted to the faculty of the Virginia Polytechnic Institute and State University in partial fulfillment of the requirements for the degree of

Doctor of Philosophy
In
Materials Science and Engineering

Guo-Quan Lu, Committee Chair
Alex O. Aning
Stephen L. Kampe
Kathleen Meehan
Carlos T. A. Suchicital

May 4, 2005
Blacksburg, Virginia

Keywords: constrained sintering, rigid substrate, zinc oxide, ceramic, crystallizable glass, in-plane stress

Densification Behavior of Ceramic and Crystallizable Glass Materials Constrained on a Rigid Substrate

Jesus N. Calata

Abstract

Constrained sintering is an important process for many applications. The sintering process almost always involves some form of constraint, both internal and external, such as rigid particles, reinforcing fibers and substrates to which the porous body adheres. The densification behavior of zinc oxide and cordierite-base crystallizable glass constrained on a rigid substrate was studied to add to the understanding of the behavior of various materials undergoing sintering when subjected to external substrate constraint.

Porous ZnO films were isothermally sintered at temperatures between 900°C and 1050°C. The results showed that the densification of films constrained on substrates is severely reduced. This was evident in the sintered microstructures where the particles are joined together by narrower necks forming a more open structure, instead of the equiaxed grains with wide grain boundaries observed in the freestanding films. The calculated activation energies of densification were also different. For the density range of 60 to 64%, the constrained film had an activation energy of 391 ± 34 kJ/mole compared to 242 ± 21 kJ/mole for the freestanding film, indicating a change in the densification mechanism. In-plane stresses were observed during the sintering of the constrained films. Yielding of the films, in which the stresses dropped slight or remained unchanged, occurred at relative densities below 60% before the stresses climbed linearly with increasing density followed by a gradual relaxation. A substantial amount of the stresses remained after cooling.

Free and constrained films of the cordierite-base crystallizable glass (glass-ceramic) were sintered between 900°C and 1000°C. The substrate constraint did not

have a significant effect on the densification rate but the constrained films eventually underwent expansion. Calculations of the densification activation energy showed that, on average, it was close to 1077 kJ/mole, the activation energy of the glass, indicating that the prevailing mechanism was still viscous flow. The films expanded earlier and faster with increasing sintering temperature. The expansion was traced to the formation of pores at the interface with the silicon substrate and to a lesser extent on aluminum nitride. It was significantly reduced when the silicon substrate was pre-oxidized at 900°C, leading to the conclusion that the pore formation at the interface was due to poor wetting, which in turn was caused by the loss of the thin oxide layer through a reaction with the glass.

Acknowledgments

I would like to extend my gratitude to all individuals and institutions that in various ways and capacities enabled me to pursue and complete this research work. Foremost among them is my thesis adviser, Dr. Guo-Quan Lu. With his guidance and support, I was able to engage in a broad range of research to complement the work that I performed for this dissertation. His methods of conducting research and ways of tackling problems spurred me to think outside of the box in order to solve various technical issues I encountered while conducting my research. I am also grateful to Dr. Carlos Suchicital, who graciously included me in some of his research projects, and in a way acted as my other adviser. I also thank the rest of my examination committee members for agreeing to help oversee the completion of my dissertation.

I would also like to acknowledge the support and assistance of my graduate student colleagues who were always willing to show me how to perform tests and experiments that were new to me as I took on various projects. They include Jaecheol Bang, with whom I worked closely on sintering related projects, Tom Kuhr, who did significant work on the electrostatic chuck project within our group, Simon Wen, Victor Liu, Kelly Stinson-Bagby, John Bai, and Zach Zhang for their assistance on some of the packaging projects. I would like to acknowledge the rest of the undergraduate and graduate students who worked in our research group over the years and who enriched my research and social environment.

I am grateful for the assistance provided by various laboratory managers, engineers and technicians who helped me with my research. They include Dave Berry in the MSE department, Mac MacCord in ESM for providing valuable training in the scanning acoustic microscope, Steve McCartney in the materials characterization lab, and Dan Huff of the packaging lab.

I extend my gratitude to my father, late mother, brother and sister for their unfailing support of my endeavors, even while they are halfway around the world. They have always shown concern about my well-being and my studies. In the same breadth, I

would like to mention my relatives in Pennsylvania (uncle, aunt and cousins) who practically served as my immediate family here in the United States. Without their presence, my life here would have been different.

The Filipino students here in Blacksburg have served as my connection to my home country by providing the camaraderie that is unique among Filipinos and I am very grateful for that.

Finally, I would like to acknowledge two institutions from my home country that were instrumental in sending me here, namely the University of the Philippines and the Department of Science and Technology.

Table of Contents

List of Figures

List of Tables

Symbols

D_{gb}, D_l, D_s	grain boundary, lattice, and surface diffusion coefficient
$\dot{\varepsilon}_x$, $\dot{\varepsilon}_y$, $\dot{\varepsilon}_z$	principal strain rates
$\dot{\varepsilon}_f$	free linear strain rate
ε_o	permittivity of free space
E_p	uniaxial viscosity of porous body
E_s	Young's modulus of substrate
δ_s, δ_{gb}	width of surface region, grain boundary region
G	grain size
G_p	shear viscosity
γ_{sv}, γ_{gb}	surface energy, grain boundary energy
η	viscosity
k	relative dielectric constant
K_p	bulk viscosity
κ	curvature
ν_p	Poisson's ratio of porous body
ν_s	Poisson's ratio of substrate
ϕ	stress intensification factor
Q	activation energy
ρ	density
$\overline{\rho}$	relative density
$\dot{\overline{\rho}}$	relative densification rate
σ_x, σ_y, σ_z	principal stresses
V	volume, voltage
Ω	atomic volume

Chapter 1
Introduction

The sintering process has been an important tool in the fabrication of various materials into useful articles. For thousands of years, it was used to create tools and implements out of naturally occurring ceramic materials. Today, it is used to manufacture a wide range of products for consumers, electronics, transportation and biomedical systems and applications, e.g., rocket nozzles, ultrasonic transducers, automobile engines, semiconductor packaging substrate, and dental implants. For ceramic materials including many glasses, sintering remains the most important, if not the only viable fabrication process. It is also used for other materials such as refractory metals and alloys where melting is not a practical method because of the extreme temperature required. Unlike melting, the material(s) need not be transformed into liquid for consolidation and densification to take place and it can be done at temperatures hundreds of degrees below the melting point. The preform essentially retains its shape, albeit with reduced dimensions. Advances in technology require multi-component structures, an area where sintering is a suitable process. Maintaining the structural features is difficult in a melt because of accelerated reaction kinetics that can obliterate the identity of individual component materials. Sintering is not only used for high-temperature materials but also for other materials that can be densified below 1000°C. A good example is the firing of glass-based substrates and of screen-printed metallic inks or paste for microelectronic applications. It is usually during sintering that the properties of the final products are determined and its importance cannot be understated. Generally, the properties are enhanced by the changes that occur during the sintering process.

1.1 Significance of Research

In recent years, sintering has been applied to more advanced applications such as in microelectronics technology[1] and introduced a new set of processing challenges. These applications require the combination of two or more types of materials to gain the desired properties or functional structures. The integration of different materials into a single piece or device introduced conditions that have profound effects on the processing and properties of the materials involved. This is particularly true in microelectronic applications where the dimensional scale is such that changes in the sintering behavior of the materials can cause serious problems from processing to reliability of the finished products.

In monolithic structures, the main concern is the production of a uniform green microstructure conducive to the formation of dense, defect-free bodies. In articles combining various materials, other conditions can have an adverse effect on the densification processes. One such condition is the introduction of a constraint on the materials during sintering. Constrained sintering has been found to retard the densification of powder compacts, leading to lower final densities and different microstructure, i.e., pore size[2-4]. The presence of in-plane stresses and differential sintering rates can lead to camber, warping and distortion [5]. On a more fundamental level, it is also believed to cause a shift in the densification mechanisms, which retards the sintering process[6].

The constraint on the sintering body can be either internal, such as in ceramic matrix composites, or external. The sintering of a film on a rigid substrate and the sintering of laminated layers are examples of externally constrained systems. These structures are obtained readily by tape casting[7,8] and/or screen printing and are commonly found in multilayer cofired ceramic packages[9], hybrid electronic packages[10] and multilayer ceramic capacitors. A multilayer ceramic package consists of laminated thin ceramic sheets screen-printed with metal ink to form the circuit patterns. In general, the two types of materials have different densification kinetics[5] with one material undergoing rapid densification at a lower temperature ahead of the other. Although the densifying layers are not really constrained on a rigid substrate, they

are effectively constrained by the other layers that have yet to begin densifying. In hybrid packages, the rigid substrate effectively prevents the porous layers from shrinking along the substrate plane such that densification is limited mainly to shrinkage normal to the substrate.

As mentioned earlier, constrained-film sintering can lead to defective components. Common defects in hybrid packages include high porosity in the sintered films or layers, delamination and cracking at the film-substrate interface[10]. In multilayer ceramic packages, camber, distortion and via defects cause problems in manufacturing and degrade the reliability of these devices[11]. A better understanding of the densification behavior of constrained films is necessary in order to determine the mechanisms that give rise to these defects. Ultimately, the knowledge gained from these studies will help engineers optimize the design and manufacturing process that in turn will lead to higher production yields, lower costs and more reliable devices.

1.2 Motivation and Goals

Although sintering of constrained films is a common manufacturing process, there is very little experimental work that can be found in the literature on the sintering behavior of constrained films, as Bordia and Scherer[12] pointed out. This is mainly due to the difficulty involved in conducting the necessary experiments and the lack of suitable equipment for investigating constrained-film sintering. This work was performed to obtain some of the needed experimental data and provide further insight into the densification of constrained films.

1.3 Research Objectives

In this study, a custom-built optical setup was used to obtain the experimental sintering data. This technique has already been used with considerable success in determining the experimental curves for non-crystallizing borosilicate glass[3] and gold paste or ink[4]. In order to determine the influence of constraint by a rigid substrate on

the densification behavior of ceramic and glass-ceramic materials, sintering experiments were performed on representative materials. Zinc oxide was used as a representative material to study the densification of polycrystalline ceramic materials. Unlike some of the commonly used systems like alumina, ZnO can be densified at temperatures within the range of the hot stage used in the optical setup. Zinc oxide is also a major component in a class of devices known as varistors[13,14]. Experimental densification curves were also obtained for a low-expansion crystallizable cordierite-base glass-ceramic, which sinters at less than 1000°C and can be a suitable base material for low-temperature cofired packages because its coefficient of thermal expansion (CTE) is close to that of silicon.

The specific objectives of this research involving the two types of materials are as follows.

1. **Study the effect of constraint by a rigid substrate on the densification behavior of ZnO powder.** Under this objective, sintering of free tapes and constrained coatings of zinc oxide was carried out at various temperatures to obtain the densification rates. From these experiments, the effect of temperature on sintering rate, the variation in densification rate at various densities, and activation energies at various densities can be obtained. The results were used to compare densification of free samples and constrained coatings.
2. **Investigate the densification behavior of crystallizable glass (glass-ceramic) powder coatings on rigid substrates.** Freestanding tapes and coatings on silicon and aluminum nitride substrates were isothermally sintered at various temperatures to obtain densification profiles. Results from these experiments were used to determine the effects of sintering temperature, constraint by a rigid substrate, and type of substrate. The effect of constraint on densification mechanism, as manifested by activation energy values, may also be determined. The results will be used to compare the sintering of glass-ceramic to non-crystallizing glass.
3. **Study and measure the in-plane stress development during the constrained sintering of ZnO and glass-ceramic powder coatings constrained on rigid substrate.** In the absence of chemical reactions and/or external applied pressure,

the driving force of sintering originates from excess surface energy in the powder compact manifested by a surface tension that pulls the sintering body together. Rigid constraint provides an opposing force to the tendency to shrink (or expand), causing a buildup of in-plane stresses in the film. The curvatures of the constrained samples were obtained to determine the in-plane stresses in the coatings during sintering. Determination of the in-plane stress profile during sintering could help explain differences between free sintering and constrained sintering.

4. **Investigate and demonstrate some potential applications of constrained films and coatings of glass and ceramic materials.** The application of constrained films as dielectric layers in devices such as electrostatic chucks for semiconductor wafer handling and ceramic plate heaters were explored resulting in the fabrication of prototype structures for these devices.

1.4 Organization of the Dissertation

The dissertation is organized according to the following scheme. The current chapter (Chapter 1) provides a brief introduction into the research topic and a statement of the motivation and objectives of the research. In Chapter 2, a theoretical framework of the research area is provided through a survey of the literature on constrained sintering of porous materials. The details of the experimental procedures performed in this work can be found in Chapter 3. The results and discussion is actually divided into two chapters, reflecting the fact that, although the dissertation topic is on constrained sintering, the work done covers two different materials that deserve to be discussed in two separate sections. Chapter 4 is about the sintering of zinc oxide while Chapter 5 tackles the sintering of crystallizing glass or glass-ceramic. In Chapter 6, fabrication of electrostatic chucks and ceramic plate heaters with glass and glass-ceramic coatings as the dielectric layers are discussed as applications of constrained sintered films. Chapter 7 contains the conclusions on the constrained sintering of zinc oxide and the glass-ceramic, as well as recommendations for future work and refinements that can be done on the experimental

procedures that were followed in this study. The compilation of references follows. Two appendices are included that contain past research involving constrained sintering and materials synthesis. Appendix A covers work done on electrostatic chucks fabricated from stainless steel coated with borosilicate glass (BSG). Appendix B contains work done on the synthesis of nanoscale multifunctional composite materials out of ferroelectric and ceramic ferrite for possible use in passive components for power electronics applications, as well as applications yet to be identified. The dissertation ends with the vita of the author.

Chapter 2
Literature Review

Sintering is the most important step in powder processing because it is at this stage that the material is subjected to very high temperatures, causing the particles to form bonds that are needed to hold the mass together. Sintering occurs by atomic diffusion processes that are stimulated by high temperatures[15-18]; substantial particle rearrangement and consolidation may occur initially, especially in loosely packed bodies[19]. The transport mechanisms that subsequently follow will depend on the type of material being sintered. Amorphous materials generally sinter by viscous flow, which has been extensively studied by numerous investigators.[20]. On the other hand, polycrystalline materials sinter by one or more mechanisms occurring singly or in parallel, depending on the materials system and sintering conditions[21]. This makes it difficult to isolate the mechanisms involved and adds to the complexity of the sintering process. In general, bulk transport mechanisms such as volume diffusion, grain boundary diffusion, plastic flow, and viscous flow result in shrinkage or densification while surface transport does not. However, surface transport is recognized to be important in interparticle neck growth and the sintering of some covalent solids and low-stability ceramics.

2.1. Overview of Sintering Theory

Sintering is usually classified into several types based on the mechanisms that are thought to be responsible for shrinkage or densification. Sintering that proceeds mainly by solid-state diffusion falls under *solid state sintering*. Polycrystalline materials usually sinter by this process. On the other hand, amorphous materials sinter by viscous flow and are thus considered to undergo *viscous sintering*. Another type of sintering that

makes use of a transient second phase that exists as a liquid at the sintering temperature is known as *liquid phase sintering*[22,23]. The liquid phase under the right conditions can provide a path for rapid transport and, therefore, rapid sintering. Finally, processes that make use of an externally applied pressure to enhance densification are classified under *pressure sintering*.

The entire sintering process is generally considered to occur in three stages[19,24]: (i) initial stage, (ii) intermediate stage, (iii) and final stage. There is no clear-cut distinction between the stages since the processes that are associated with each stage tend to overlap each other. However, some generalizations can be made to distinguish one stage from the next. In the initial stage, particles can rearrange by rotating and sliding into more stable positions in response to the sintering forces. This contributes to shrinkage and an overall increase in density. During particle rearrangement, there is an increase in interparticle contact, enabling the formation of necks between particles. Neck formation and growth can take place by diffusion, vapor transport, plastic flow, or viscous flow. The initial stage is assumed to last until a neck radius of around 0.4 to 0.5 of the particle radius is attained.

The intermediate stage is considered to begin when the pores have attained their equilibrium shapes as dictated by surface and interfacial energies. Because the density remains low at this point, the pores are still continuous or interconnected. Densification is assumed to take place by the reduction in cross section of the pores. Eventually, pores become unstable and are pinched off from each other, leading to the final stage of sintering. Of the three stages, the intermediate stage covers the majority of the sintering process.

The final stage covers the elimination of the isolated pores until the theoretical density is reached. This stage is also characterized by grain growth in which the larger grains tend to increase in size at the expense of the smaller grains. The extent of grain growth is dependent on both the material and the sintering condition.

Sintering Mechanisms

Polycrystalline materials generally sinter by diffusional processes while amorphous materials densify by viscous flow. The driving force for all these

mechanisms is the tendency of the material to reduce its chemical potential or energy. This is accomplished by material transport from regions of high energy to regions of lower energy. Surfaces, interfaces and grain boundaries have associated energies that depend on surface or boundary curvature. By eliminating or minimizing these surfaces or by reducing their curvature, the overall energy of the material is reduced. There are at least six different mechanisms of sintering in polycrystalline materials and they are summarized in Table 2.1. Only volume diffusion of matter from the grain boundaries or from dislocations in the neck region can produce densification. The other mechanisms, though, cannot be ignored because they can reduce the neck curvature and reduce the driving force and densification rate.

Table 2.1. Sintering Mechanisms in Polycrystalline and Amorphous Solids [19,21].

Type of solid	Mechanism	Source of matter	Sink of matter	Densifying
Polycrystalline	Surface diffusion	Surface		No
	Lattice diffusion	Surface		No
	Vapor transport	Surface		No
	Grain boundary diffusion	Grain boundary		Yes
	Lattice diffusion	Grain boundary		Yes
	Lattice diffusion	Dislocations		Yes
Amorphous	Viscous flow	Unspecified	Unspecified	Yes

Theoretical Analyses of Sintering

Several approaches have been used to analyze sintering. These include the scaling laws[25], analytical models, empirical or phenomenological equations, and statistical and numerical techniques. Sintering models are often simplified, idealized representations of the particles in a sintering body. It was necessary to assume an idealized structure of the powder system to facilitate the mathematical analysis of what are clearly complex phenomena. Therein lies the problem with these analytical models because real systems are far from being ideal. In these models, the particles are assumed

to have a spherical shape and the same size and are uniformly packed. A unit of the powder, referred to as the *geometric model*, is then taken to represent the entire system. For the assumed model, the sintering equations are then obtained by formulating the corresponding mass transport equations and solving them using the appropriate boundary conditions.

In the analysis of the initial stage of sintering, a model consisting of two equal-sized spheres of radius R that are in contact is usually assumed[21,26]. The models for densifying and non-densifying mechanisms are slightly different to reflect the changes that arise from the mechanisms concerned. The geometrical models are shown in Figure 2.1. The equation for neck growth can be expressed in the general form[26-29]

$$\left(\frac{X}{R}\right)^m = \frac{H}{R^n}t \tag{2.1}$$

where X is the of the neck formed between the particles, r is the radius of the neck surface, *m* and *n* are constants that depend on the mechanism involved, H is a coefficient characteristic of the mechanism, and *t* is the time. The equation for neck growth by viscous flow was first derived by Frenkel[30]. and also follows the form of Eq. (2.1). Table 2.2 summarizes the coefficients and constants for the various mechanisms.

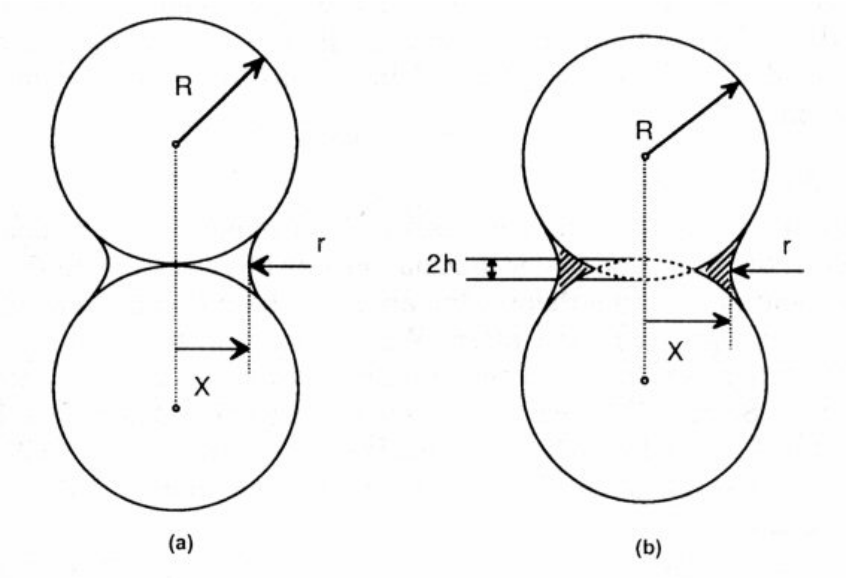

Figure 2.1. Two-particle geometric model for the initial stage of sintering.

Table 2.2. Values for the constants m and n in Eq. (2.1)[21].

Mechanism	*m*	*n*	H^a
Surface diffusion	7	4	$56D_s\delta_s\gamma_{sv}\Omega/kT$
Lattice diffusion from the surface	4	3	$20D_l\gamma_{sv}\Omega/kT$
Vapor transport	3	2	$3p_o\gamma_{sv}\Omega/(2\pi mkT)^{1/2}kT$
Grain boundary diffusion	6	4	$96D_{gb}\delta_{gb}\gamma_{sv}\Omega/kT$
Lattice diffusion from the grain boundary	5	3	$80\pi D_l\gamma_{sv}\Omega/kT$
Viscous flow	2	1	$3\gamma_{sv}/2\eta$

[a] D_s, D_l, D_{gb}, diffusion coefficients for surface, lattice, and grain boundary diffusion; δ_s, δ_{gb}, thickness for surface and grain boundary diffusion; γ_{sv}, specific surface energy; Ω, atomic volume; k, Boltzmann constant; T, absolute temperature, m, mass of atom; p_o vapor pressure over a flat surface, η, viscosity.

The geometrical model for intermediate stage sintering of polycrystalline materials is different from that of amorphous systems. The model that is most commonly used was proposed by Coble[31], where he derived equations for lattice and grain boundary diffusion. The powder compact is assumed to consists of equal-sized particles with the shape of a tetrakaidecahedron, with cylindrical pores along the edges. A tetrakaidecahedron is constructed by trisecting the edges of an octahedron and discarding the six vertices. The resulting structure has 36 edges, 24 corners, and 14 faces with 8 being hexagonal and 6 square. Based on Coble's derivation, the densification rates for lattice and grain boundary diffusion can be approximated as follow

Lattice diffusion:
$$\frac{1}{\rho}\frac{d\rho}{dt}\approx\frac{AD_l\gamma_{sv}\Omega}{\rho G^3kT} \tag{2.2}$$

Grain boundary diffusion:
$$\frac{1}{\rho}\frac{d\rho}{dt}\approx\frac{4}{3}\left(\frac{D_{gb}\delta_{gb}\gamma_{sv}\Omega}{G^4kT\rho(1-\rho)^{1/2}}\right) \tag{2.3}$$

where ρ is the density, A is a constant and G is the grain size. Because of the approximations made by Coble, these equations are no more than order-of-magnitude

calculations. Refinements to Coble's model have since been made to account for the more complex pore structure[32,33].

For the densification of amorphous systems, a structure consisting of a cubic array of intersecting cylinders was proposed by Scherer[34]. The equation is rather complex and does not explicitly express the density or densification rate as a function of time. However, it has been shown experimentally to predict well the densification of materials such as colloidal gels, polymeric gels, and consolidated glass particles.

Coble[31] used a procedure similar to that used in deriving intermediate stage equations to obtain the final stage sintering equations. From his derivation, the densification rate for lattice diffusion for the final stage can be expressed as

$$\frac{1}{\rho}\frac{d\rho}{dt} \approx \frac{BD_l \gamma_{sv} \Omega}{\rho G^3 kT} \tag{2.4}$$

where B is a constant. Note that this is strikingly similar to the equation for intermediate stage sintering, Eq. (2.2), except in the numerical constants. Coble did not derive the equation for grain boundary diffusion but this can be obtained from the models that he developed for diffusional sintering under applied pressure[35,36].

For viscous flow, the work done by Mackenzie and Shuttleworth[37] using a concentric sphere model seems to be appropriate. The densification rate is

$$\frac{d\rho}{dt} = \frac{3}{4}\frac{p}{\eta}(1-\rho) \tag{2.5}$$

where p is $2\gamma/r$, with r being the pore radius. This equation is considered a reasonable representation of the last stage of sintering when the pores are closed and isolated.

Based on the preceding discussions of the analytical models, it is clear that the sintering phenomenon in polycrystalline solids is much more complex than that in amorphous materials. The sintering of polycrystalline materials is more dependent on the microstructure of the powder system. The result is that simplifications in the models make the corresponding sintering equations mere approximations and tend to be more useful in making qualitative descriptions. However, this does not detract from their usefulness. For example, with the temperature dependence of the process known beforehand, they can be used to determine from experimental data the dominant mechanism through the activation energy values. On the other hand, amorphous

materials are less sensitive to microstructure such that idealization of the structure can lead to analytical solutions that can quantify the sintering behavior satisfactorily. It is this simplicity that has led others to extend viscous sintering concepts to the analysis of data from polycrystalline materials[38-40]. More recently, a combined-stage sintering model was proposed wherein a single equation was derived to represent the sintering process from beginning to end[41].

Driving Forces for Sintering and Sintering Stress

As mentioned earlier, sintering is accompanied by a lowering of the free energy of the system. The processes and other phenomena that provide the impetus for reducing the free energy are usually referred to as the driving forces for sintering and include the force associated with the curved surfaces of particles, externally applied pressure, and chemical reaction(s). While the effect of the latter two sources appears straightforward by "pumping" mechanical energy and heat directly into the process, the surface curvature does not add energy to the system but instead works by reducing the total interfacial and surface energies. During sintering, necks forming between particles substitute grain boundary area for surface area, always with a net reduction in total energy.

Excluding externally applied pressure and chemical reactions, the driving forces that cause materials to be transported are the chemical potential gradient and the stress generated at the contacts between particles. In the former, material flows into the neck area under the influence of a chemical potential gradient arising from the differences in curvature of the surface. The chemical potential, μ, of an atom beneath a curved surface is altered by the surface curvature. For a curved surface with principal radii of curvature r_1 and r_2, the potential difference is given by

$$\Delta\mu = \mu - \mu_o = \gamma\Omega\left(\frac{1}{r_1} + \frac{1}{r_2}\right) \tag{2.6}$$

where Ω is the atomic volume and γ is the surface energy of powder particle. The radius is positive when the surface is convex and negative if the surface is concave. The chemical potential gradient also produces a gradient in the vapor pressure above these two surfaces such that

$$\Delta\mu = kT \ln\left(\frac{P_v}{P_o}\right) \tag{2.7}$$

where P_v is the partial vapor pressure over a curved surface, P_o is the partial vapor pressure over a flat surface. Atoms move from the convex to the concave regions to decrease the potential gradient. The vacancies move countercurrent to the diffusion of the atoms and therefore, diffuse away from the contact area between the solid particles and sink at the dislocations or grain boundaries.

Referring to Figure 2.1, the outer edge of the contact is subjected to a stress, σ, given by[42]

$$\sigma = \gamma\left(\frac{1}{r} - \frac{1}{x}\right) \tag{2.8}$$

where γ is the surface tension. Under a concave surface, this stress is tensile and under a convex surface, compressive. The stress gradient between the particle interior and the neck causes material transport to relieve the stress.

The stress can be related to the densification rate for diffusion-controlled mechanism by the general form that includes an externally applied pressure, p_a

$$\frac{1}{\rho}\frac{d\rho}{dt} = -\frac{3}{L}\frac{dL}{dt} = \frac{3}{\eta_\rho}\left(p_a\phi + \sigma\right) \tag{2.9}$$

where (1/L)dL/dt is the linear strain rate for sintering, ϕ is the stress intensification factor, and η_ρ has the dimensions of viscosity and is referred to as the densification viscosity. The quantity σ is the thermodynamic driving force with the units of pressure or stress and is referred to either as the sintering pressure or sintering potential. The equation for σ is actually more complex for a polycrystalline ceramic than that given in Eq. (2.8) because the pores are in contact with grain boundaries and may be of the form[43]

$$\sigma = \frac{2\gamma_{gb}}{G} + \frac{2\gamma_{sv}}{r} \tag{2.10}$$

where γ_{gb} is the grain boundary energy, γ_{sv} is the surface energy, G is the grain size and r is the pore radius. Equation (2.9) can be rewritten as

$$\frac{1}{\rho}\frac{d\rho}{dt} = \frac{3\phi}{\eta_\rho}\left(p_a + \Sigma\right) \tag{2.11}$$

where $\Sigma = \sigma/\phi$ has the units of stress and is referred to as the sintering stress. It occurs in linear combination with the externally applied pressure, p_a, and may be considered as the *equivalent externally applied stress* with the same effect on the sintering as the curved surfaces of the pores and grain boundaries. The definition is useful in analyzing cases where mechanical stresses are present such as in pressure sintering and constrained sintering. It provides a basis for the experimental measurement of the driving force for sintering.

2.2. Constrained Sintering on Substrates

When a porous film is sintered on a rigid substrate, shrinkage does not occur along the substrate plane. The shrinkage is limited to the direction normal to the substrate. As a consequence, tensile stress could develop in the film that not only retards densification but also induce the formation of flaws in the film. Other factors may also be responsible for reduced densification. There are, however, only a few experimental works on constrained-film sintering and that the process itself is not well understood. Among these are the works of Garino and Bowen[2], Bordia and Jagota[44], Lu, et al.[5] and, more recently, by Bang and Lu[3] and Choe, et al[4].

Viscous Analysis

The problem of constrained sintering can be analyzed using the viscoelastic (VE) analogy [45,46] that relates stresses and strains in the sintering body. However, it was recognized that the VE analogy is difficult to apply to the process because the sintering materials do not follow linear viscoelasticity [12,47]. The application of constitutive equations for viscous sintering was developed independently by Scherer[48]. Although it was originally developed for materials that sinter by viscous flow, it has been applied to the analysis of materials that densify both by viscous flow and solid state diffusion [2,49,50]. The expressions for the apparent Young's modulus and Poisson's ratio, *E* and

ν, respectively, were derived directly for a cubic array of viscous cylinders instead of using some empirical equations. The constitutive equations can be written as

$$\dot{\varepsilon}_x = \dot{\varepsilon}_x + E_p^{-1}\left[\sigma_x - \nu_p\left(\sigma_y + \sigma_z\right)\right] \tag{2.12a}$$

$$\dot{\varepsilon}_y = \dot{\varepsilon}_f + E_p^{-1}\left[\sigma_y - \nu_p\left(\sigma_x + \sigma_z\right)\right] \tag{2.6b}$$

$$\dot{\varepsilon}_z = \dot{\varepsilon}_f + E_p^{-1}\left[\sigma_z - \nu_p\left(\sigma_x + \sigma_y\right)\right] \tag{2.6c}$$

where σ_x, σ_y, and σ_z are the principal stresses; $\dot{\varepsilon}_x, \dot{\varepsilon}_y$, and $\dot{\varepsilon}_z$ are the principal strain rates, and $\dot{\varepsilon}_f$ is the free linear strain rate obtained from free sintering ($\dot{\varepsilon}_f = \dot{\rho}/(3\rho)$ where $\dot{\rho}$ is the densification rate). E_p and ν_p are the uniaxial viscosity and Poisson's ratio of the porous body, respectively. Because the elastic response of the body is small compared to the overall strain, it is conveniently ignored in the equations above. Equations ((2.12a-c) look very similar to the equations for an incompressible fluid except that the porous body is compressible. Analogous to the elastic case, the shear, G_p, and bulk, K_p, viscosities can be expressed as[47]

$$G_p = \frac{E_p}{2\left(1+\nu_p\right)} \tag{2.13}$$

$$K_p = \frac{E_p}{3\left(1-2\nu_p\right)} \tag{2.14}$$

The uniaxial viscosity for a porous sintering body are related to the shear and bulk viscosities, G_p and K_p by

$$E_p = \frac{9K_pG_p}{3K_p + G_p} \tag{2.15}$$

$$\nu_p = \frac{3K_p - 2G_p}{2\left(3K_p + G_p\right)} \tag{2.16}$$

Application to Constrained-film Sintering

During the firing process, the film can shrink significantly in the normal direction (z) but hardly in the planar directions (x, y). This is expected to lead to the development of stresses in the film, specifically in the x-y plane but not in the z-direction. By letting

$\dot{\varepsilon}_x = \dot{\varepsilon}_y = 0$, and $\sigma_z = 0$ in Eqs. (2.12a-c), the in-plane stress, σ, (= σ_x = σ_z) can be found by

$$\sigma = \frac{-\dot{\varepsilon}_f E_p}{1-\nu_p} \tag{2.17}$$

Densification proceeds entirely by shrinkage in the z-direction, such that for a constrained film

$$\left[\frac{\dot{\rho}}{\rho}\right]_c = -\dot{\varepsilon}_z = -\frac{(1+\nu)\dot{\varepsilon}_f}{(1-\nu)} \tag{2.18}$$

and for a free film

$$\left[\frac{\dot{\rho}}{\rho}\right]_f = -3\dot{\varepsilon}_f \tag{2.19}$$

Combining Eqs. ((2.16), ((2.18), and ((2.19), the densification rate of the constrained film can be related to that of the free body by

$$\left[\frac{\dot{\rho}}{\rho}\right]_c = \frac{(1+\nu_p)}{3(1-\nu_p)}\left[\frac{\dot{\rho}}{\rho}\right]_f = \frac{3K_p}{(3K_p+4G_p)}\left[\frac{\dot{\rho}}{\rho}\right]_f \tag{2.20}$$

Finally, by combining Eqs. (2.13), (2.17), (2.19) and (2.20), the in-plane stress can be expressed in the following form

$$\sigma = 2G_p\left[\frac{\dot{\rho}}{\rho}\right]_c \tag{2.21}$$

This is a tensile stress that develops in the material because of the constraint and is believed to be responsible for the camber that is observed to develop during the cosintering process. If the stress can be obtained experimentally, it is then possible to calculate the shear viscosity of the material as a function of relative density and at a given temperature.

Chapter 3
Experimental Methods

The experimental work involved the preparation of tapes and constrained films of the ceramic and crystallizable glass (glass-ceramic), which were used to obtain densification curves and curvatures. The slurries consisted of the raw powder milled with organic binder vehicles to form a mixture suitable for casting. Sintering experiments to obtain the sintering curves were carried out in a custom-built optical system that allows the collection of shrinkage data continuously during the sintering run at pre-programmed intervals.

3.1 Experimental Setup

The primary experimental apparatus for the research is a non-contact optically-based system where the dimensional changes of the sample undergoing sintering are monitored by shining a laser beam into the hot stage. It consists of two sections: the optical section and the sintering section. The optical section consists of a 10 mW HeNe laser, which provides the optical signal that is used to monitor/measure the dimensions of the sample. Mirrors, lenses and beam splitters are used to direct the laser beam to the sample and eventually to photodetectors to record the signals. Sintering is carried out in a water-cooled hot stage with a vertical cavity about a quarter of an inch across. The cavity is covered with a quartz (or sapphire) glass to allow optical access to the sample. The hot stage is mounted on a translation stage to enable sample positioning and scanning by the optical beam.

Free Sintering

For freestanding sample sintering experiments, the principle of operation is shown schematically in Figure 3.1. A focused laser beam is directed into the hot stage and bounced back to an intensity-sensitive silicon photodetector. The sample sits on a polished setter such as alumina or silicon to enhance the contrast between the laser beam signals reflected by the sample and setter. Scanning is done by moving the hot stage a fixed distance via a high-precision translation stage on which the hot stage sits. The edges of the sample are marked by a big drop in the brightness or intensity of the detected signal. Determination of the density from the scans is explained in a later section.

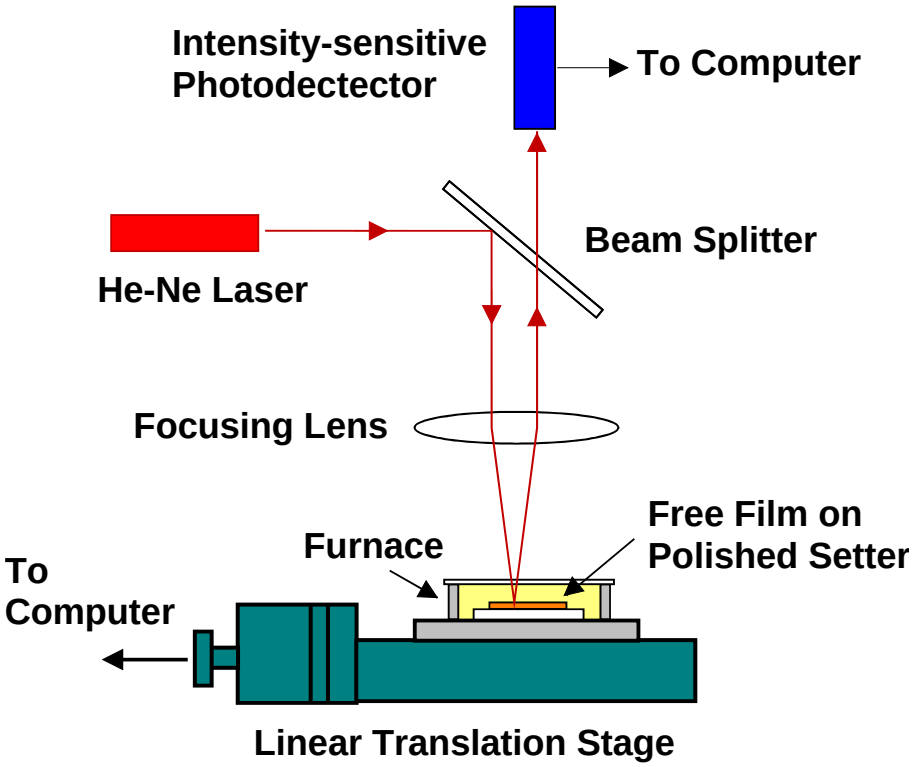

Figure 3.1. Schematic diagram of the free sintering setup consisting of a hot stage mounted on a translation stage and an optical section with a HeNe laser for scanning the sample.

Constrained Sintering

For a constrained film or coating, shrinkage is limited to the thickness of the film. Measurement of the shrinkage of a constrained film is done indirectly by bouncing the laser beam from the surface of a silicon strip, with one end resting on the surface of the coating, onto a position-sensitive photodetector (Figure 3.2). As the schematic shows, the coated substrate sits on top of the flat thermocouple surface with the constrained film or coating facing up. Two pieces of alumina are placed on top of the sample, a thin plate on the coating and a thicker piece on the bare substrate. A sliver of polished silicon is positioned on top of the alumina pieces forming an angled reflecting surface. As the film shrinks, the angle of the silicon piece changes and causes a corresponding shift in the position of the beam spot on the position-sensitive photodetector. Geometrical distortion of the beam path is negligible, considering the very small shrinkage involved and the length of the beam path, such that the shrinkage scales proportionally with the length on the detector. The distance between the sample and the detector serves to amplify the small incremental shrinkage of the film. The amount of amplification of the film shrinkage depends on the angle of the mirror that reflects the beam to the detector and it can be adjusted accordingly to achieve the desired sensitivity. The linear shrinkage is determined by converting the voltage signal into the equivalent distance based on the initial and final thickness of the coating and the length of the detector surface.

Curvature Measurement

Determination of the in-plane stresses during sintering requires the measurement of the curvature of the coated silicon substrate along with the film thickness at any given time during sintering. Unlike samples made for film shrinkage measurements, the substrate thickness chosen is such that a measurable (e.g., exceeds the noise from the setup) curvature develops due to shrinkage of the coating. This is typically of the order of 25 to 50 μm (1 to 2 mils). The setup for obtaining the curvature of the coated silicon substrate is shown schematically in Figure 3.3. Just as it is in the setup for shrinkage measurement, the curvature measurement optical bench consists of two parts: the optical scanning component and the hot stage mounted on the translation stage. This is similar

to experimental setups used by others to obtain substrate curvature[4,51-53]. The coated silicon substrate is placed on the setter in the hot stage with the coated surface facing down. During sintering, the translation stage moves, allowing the focused laser beam to scan a fixed distance along the length of the sample. The reflected beam is directed to the position sensitive photodetector and the signal is recorded as a voltage versus scan length. The recorded voltage readings are converted to equivalent lengths on the detector by a simple proportionality. The signals are converted into the appropriate curvature values using an appropriate geometrical equation. The in-plane stress is determined by treating the sample as a bilayer structure and using an approximation similar to the Stoney formula for thin films[54]. These are discussed in more detail in the later sections.

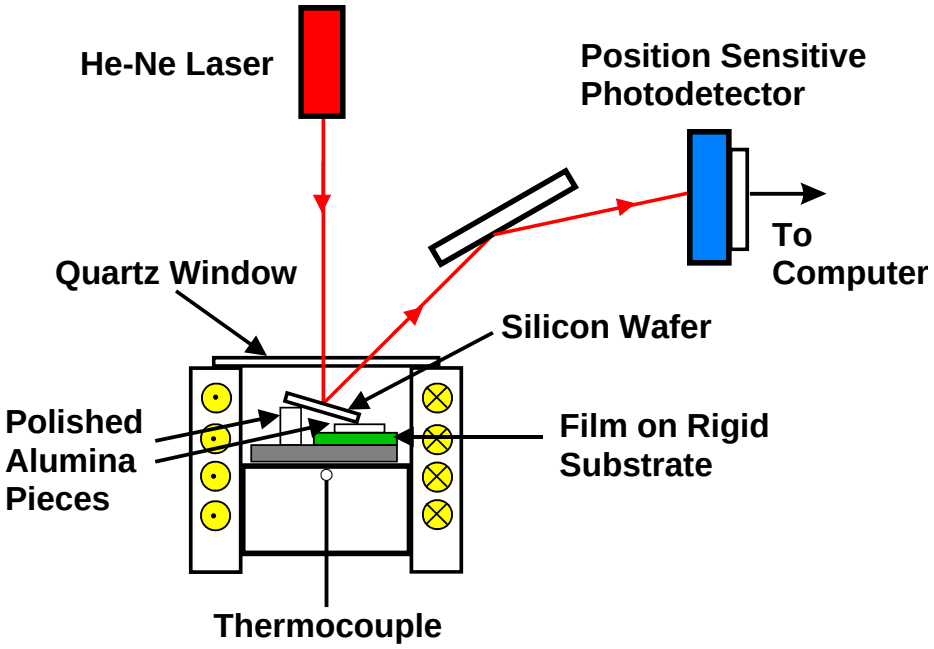

Figure 3.2. Schematic of the constrained sintering setup. The hot stage position is fixed and the change in signal position is detected by a position sensitive photodetector.

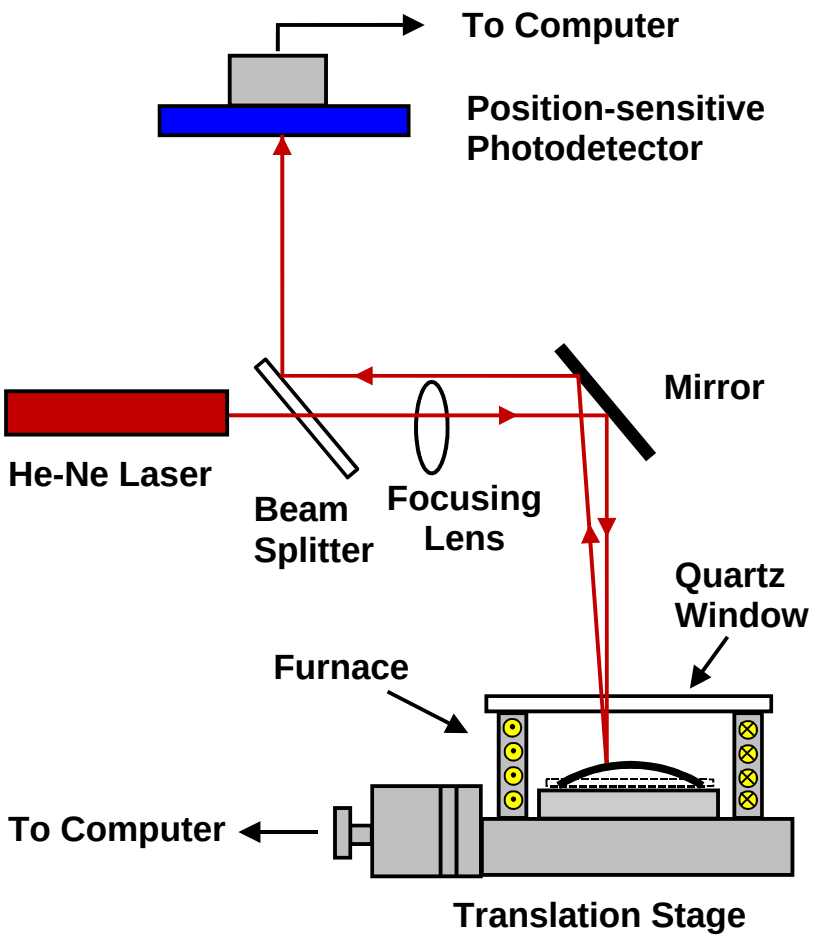

Figure 3.3. Schematic of the experimental setup for measuring the curvature of the coated substrate during sintering.

3.2 Sample Preparation

Zinc oxide samples were prepared from reagent grade crystalline powder from Fisher Scientific with a mean particle size of about 0.2 to 0.4 μm. The crystallizable glass is a MgO-Al_2O_3-SiO_2 based composition obtained from Sem-Com Co. with an average particle size of about 10 μm. A second set of samples was made from glass-ceramic powder with mean particle size of 3.97 μm to allow sintering at even lower temperatures (below nucleation and recrystallization range). The composition of the raw glass powder is listed in Table 3.1. The glass (SCE-505) is an off-stoichiometric composition that transforms primarily into cordierite ($2MgO{\cdot}2Al_2O_3{\cdot}5SiO_2$) (Figure 3.4)

[55,56]. The off-stoichiometric composition has been found to sinter at lower temperatures than stoichiometric cordierite and this is highly desirable from a processing standpoint. P_2O_5 serves as the nucleating agent in the glass. In its amorphous form, it has a coefficient of thermal expansion (CTE) of 4.6 while the crystalline form has a CTE of 4.1. It has a density of 2.66. The glass has an annealing point of 757°C and a softening point of 870°C, which were determined from DTA measurements (Sem-com, Inc. product data sheet).

Samples were prepared from the ZnO and glass powders by milling with an organic binder system and tape casting using a doctor blade with an adjustable knife setting. Freestanding and constrained samples were cast from the same slurry to ensure identical initial green density and microstructure.

Table 3.1. Chemical composition of the cordierite-base crystallizable glass (SCE-505).

Component	Weight Percent
SiO_2	51
MgO	24
Al_2O_3	21
P_2O_5	2~3
B_2O_3	2~3

Slurry Preparation

To produce the zinc oxide slurry, a fixed amount of powder was mixed with an organic binder solution, solvents, plasticizers, homogenizer and surfactant and milled in solvent-resistant plastic bottles containing quarter-inch cylindrical alumina grinding media. The roller mill speed was adjusted to a speed sufficient to induce mixing, around 60 to 65 rpm, but very little cataracting action of the media to minimize contamination of the slurry. The binder used for the submicron size sample is a high molecular weight acrylic resin dissolved in MEK (Acryloid B-7 MEK) provided by Rohm and Haas Co. The mixture used is shown in Table 3.2 and produced uniform, crack-free tapes for the sintering experiments.

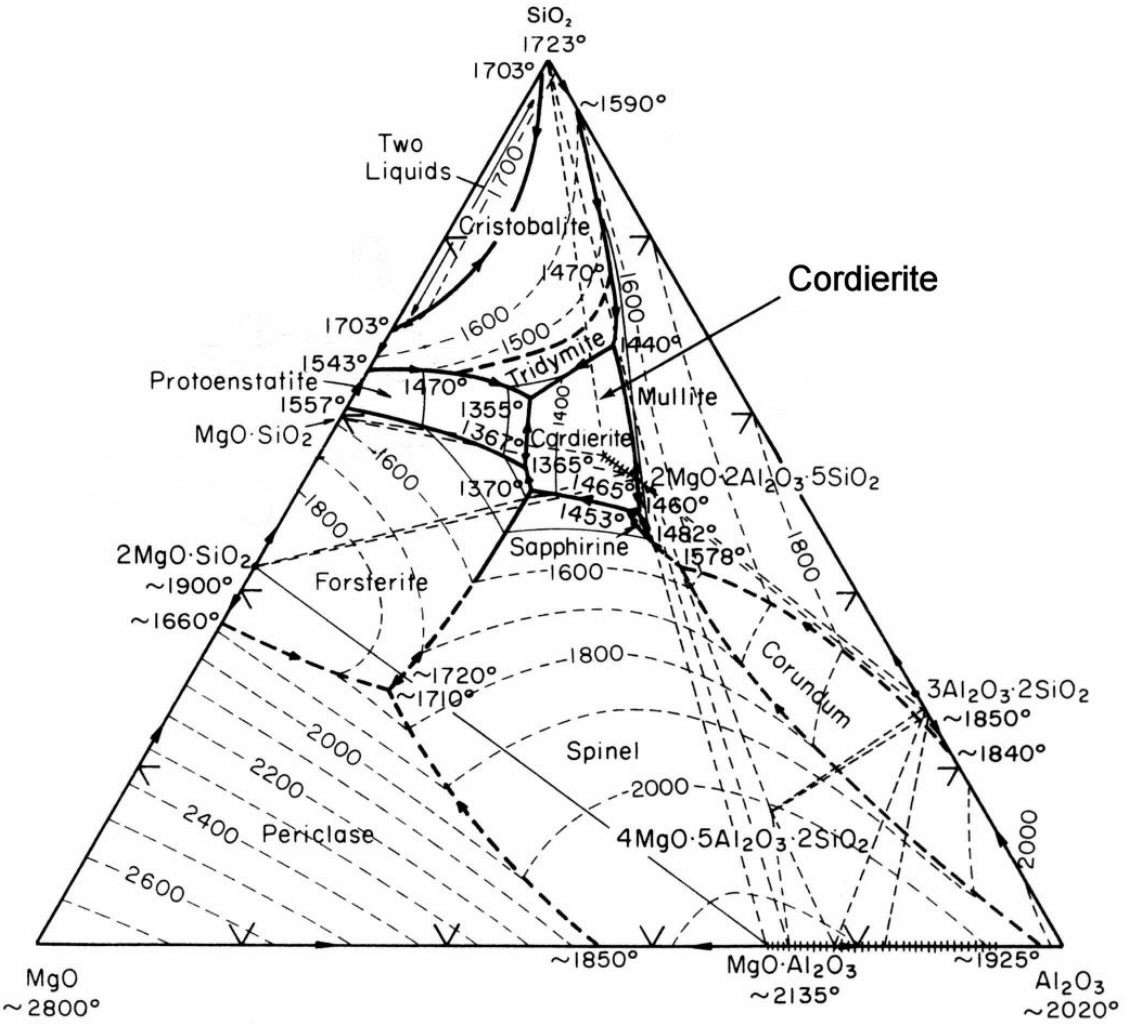

Figure 3.4. Ternary phase diagram of the MgO-Al_2O_3-SiO_2 system with the cordierite field around the $2MgO.2Al_2O_3.5SiO_2$ composition[55].

Table 3.2. Composition of slurry for tape casting of ZnO.

Ingredient	Function	Parts by weight
ZnO	Ceramic	100
MEK/Ethanol (50 wt % mixture)	Solvent	22.5
Fish oil	Deflocculant	2.2
Santicizer 160 (Butyl benzyl phthalate)	Plasticizer	4.5
Polyethylene glycol	Plasticizer	4.5
Cyclohexanone	Homogenizer	0.8
Acyrloid B-7 MEK (30% solution)	Binder	15.0

Milling of the slurry was done in two-stage milling to minimize the degradation of the binder. In the first stage, ethanol and MEK and fish oil were added to the powder and milled for 24 hours to disperse the powder and lower the viscosity of the mixture. In the second stage, the binder solution and the remaining reagents were added and the slurry was milled for another 24 hours. After milling was completed, the slurry was transferred into another container to separate it from the milling media and deaired in a vacuum dessicator for around 30 minutes or until air bubbles no longer form in the slurry. The preparation of the glass-ceramic slurry is identical except that Butvar B-79 polyvinyl butyral (PVB) from Solutia (formerly of Monsanto) was used as the binder. The slurry composition is given in Table 3.3.

Table 3.3. Slurry formulation for glass ceramic

Component	Function	Weight (g)
SCE-505 powder	Glass	100
Butvar B-79 (polyvinyl butyral)	Binder	11.04
Santicizer 160 (butyl benzyl phthalate)	Plasticizer	6.52
Defloc Z-3 Fish oil	Dispersant	2.0
Toluene	Solvent	60.28
Ethanol	Solvent	15.02

Preparation of Freestanding Samples

A portion of each deaired slurry was manually cast into tape form on a coated mylar sheet resting on a flat glass surface using an adjustable casting knife (doctor blade). The tapes were allowed to dry in air for another 24 hours and, then, were carefully peeled off from the mylar sheet to form the freestanding tapes. The tapes were subsequently dried in an oven at 100 to 115^{o}C for 2 to 3 hours. The dried tapes had a thickness of about 500 μm (20 mils). The green density was determined by cutting rectangular pieces of the dried tape and burning off the binder to obtain only the ceramic or glass powder. The green density was calculated by dividing the weight of the tape after binder burnout with the volume of the green tape. The relative green density was calculated by normalizing the green density to the density of the fully dense material.

The freestanding samples were made by cutting the dried tape into rectangular strips roughly 2.5 mm by 4 mm (Figure 3.5). The strips were, then, slowly heated at 2^{o}C per minute to 500^{o}C and held there for 2 to 3 hours to burn out the binder and other organic additives.

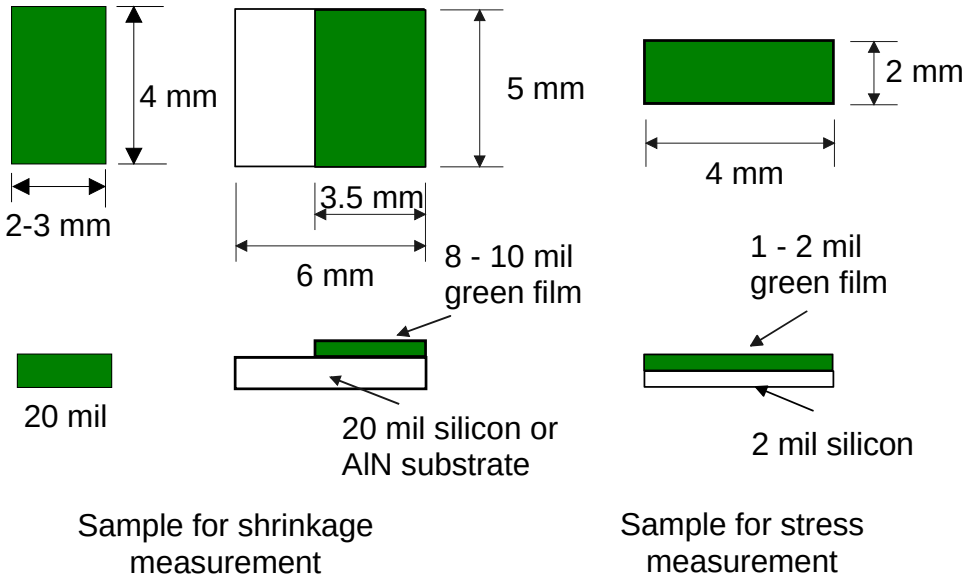

Figure 3.5. Schematic of sample geometries used for the sintering experiments in the hot stage of the optical setup (From left to right: free sintering, constrained sintering, and curvature measurement).

Preparation of Constrained Samples

To produce the constrained film samples, part of the slurries were cast on 20-mil silicon wafer substrates using the same technique employed in the preparation of the freestanding tapes. The constrained tapes were air-dried for at least 24 hours and subsequently dried at 100 to 115^{o}C for 2 to 3 hours. The constrained tapes had an average thickness of about 250 μm (10 mils) after drying. The green densities of the constrained tapes or films were assumed to be identical to their freestanding counterparts since it was cast from the same slurry composition. This was verified by repeating the method for obtaining the green density of the free tapes on some of the constrained films. The constrained films were thinner than the freestanding tapes because unlike the latter, the substrate constraint will prevent warping or distortion during sintering.

The samples for constrained sintering experiments were made by cutting the 20-mil silicon substrate into 5 mm by 5 mm squares, necessary for the samples to fit into the hot stage cavity of the sintering setup. Half of the tape was then stripped off from the square substrates and any loose portion of the remaining tape was trimmed off so as not to affect the rest of the tape during sintering. Unlike the freestanding samples, no prior binder burnout was done on the constrained samples because of loss of adhesion of the coating on the substrate upon cooling. Instead, it was incorporated in the sintering profile.

For stress measurement experiments, tapes were cast on highly polished 1-mil or 2-mil silicon wafer. A very thin substrate was necessary because the stresses developed in the film cannot produce a measurable camber or curvature in the thicker substrates. The samples used for the in-plane stress measurements were made by cutting the coated silicon wafer into 2 mm by 4 mm strips.

3.3 Sintering Experiments

Isothermal sintering experiments were carried out by heating samples rapidly after binder burnout to the sintering temperature and the data collected at intervals that are set in the control program. An entire densification profile can be obtained from a

single sample using the optical system, thus eliminating the need for multiple samples and the accompanying uncertainties in the composite densification curve from the measurement of different samples. Additional runs were made to verify the reproducibility within experimental error of each curve.

Free Sintering

Sintering of freestanding samples was carried out in the hot stage using pre-determined firing profiles. Since the binder was already removed from a previous binder burnout step, samples were rapidly heated to the sintering temperature at a ramp rate of 50°C/min. Samples were maintained at the sintering temperature for 3 hours before they were cooled down. The densification curve can be obtained from the linear shrinkage data using the following equation.

$$\bar{\rho}_o V_o = \bar{\rho}(t) V(t) \tag{3.1}$$

where $\bar{\rho}_o$ is the initial or green relative density of the powder sample, which is normalized to the density of the fully dense material; V_o is the initial sample volume; and $\bar{\rho}(t)$ and $V(t)$ are the relative density and volume at time, t, respectively. Since the sample shrinks isotropically along each direction as shown in Figure 3.6, the volume can be replaced by the cube of the width, w, of the sample such that

$$\bar{\rho}_o w_o^3 = \bar{\rho}(t)[w(t)]^3 \tag{3.2}$$

and

$$\bar{\rho}(t) = \bar{\rho}_o \left[\frac{w_o}{w(t)} \right]^3 \tag{3.3}$$

The sample width is obtained from an optical scan by locating the sections of the scan with the steepest slopes, which indicate the position of the edges of the sample. The sample width is taken at the half-maxima of the curve. This is shown schematically in Figure 3.7 where two successive scans are plotted to illustrate the change in sample width as it shrinks. The entire densification curve is compiled by obtaining the sample width in each scan and normalizing to the initial width, w_o.

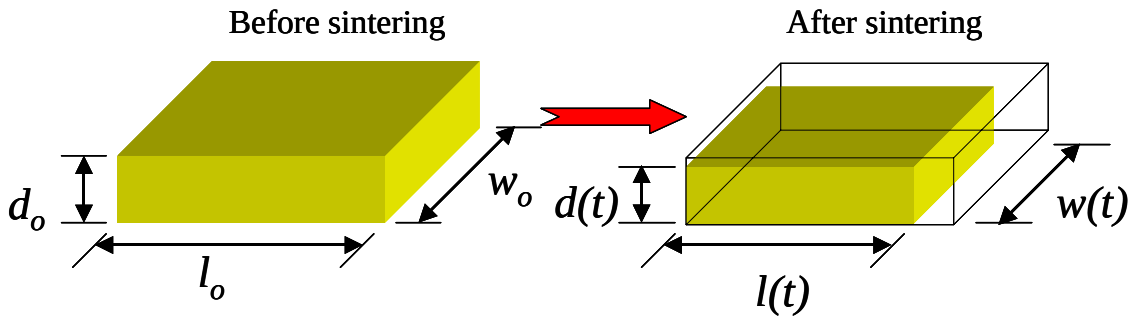

Figure 3.6. Dimensional changes in a freestanding tape undergoing isotropic shrinkage. Only one dimension needs to be monitored to obtain the volumetric change.

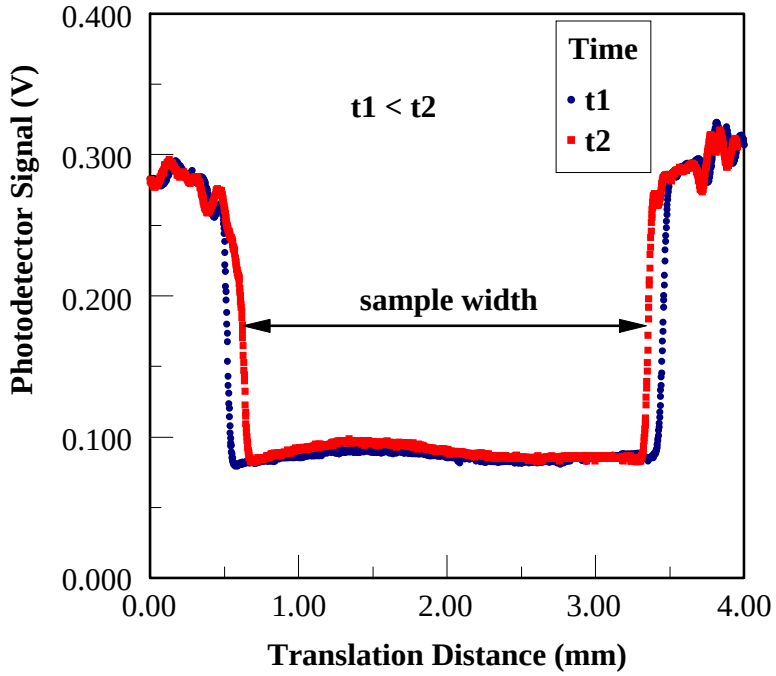

Figure 3.7. Intensity profiles that are obtained from laser scans of a freestanding sample undergoing shrinkage during sintering.

Sintering of Constrained Films

Constrained film samples were sintered using profiles similar to those for the freestanding samples except that a long binder burnout stage was appended. The samples were heated slowly at a rate of around 2°C/min followed by a 3-hour hold at 500°C. The

sintering profile is shown in Figure 3.8. Because the film can only shrink in the perpendicular direction (Figure 3.9), the density curves were calculated using the following equation.

$$\bar{\rho}(t)d(t) = \bar{\rho}_o d_o \tag{3.4}$$

Raw shrinkage curves obtained were in detector voltage versus time format and were converted to equivalent distance or thickness by considering that the vertical detector length that spans –10 V to +10V is equal to 13 mm. The results were then used to calculate both the relative shrinkage or thickness and the relative density.

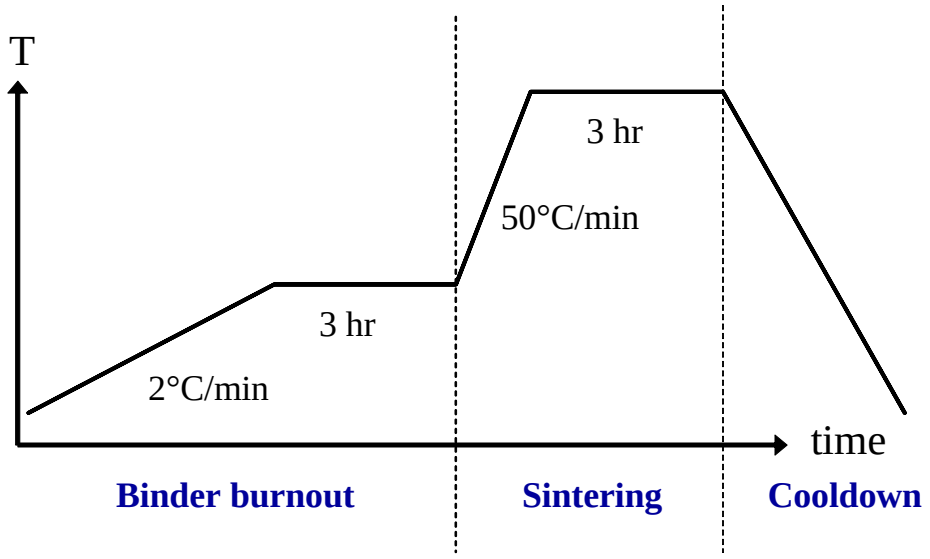

Figure 3.8. Schematic of the temperature profile for the sintering of a constrained film sample showing the various stages.

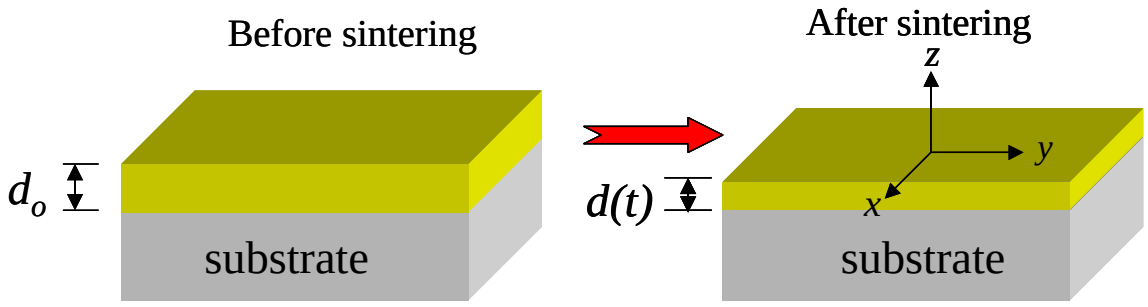

Figure 3.9. Schematic of the shrinkage of a film constrained on a substrate undergoing sintering.

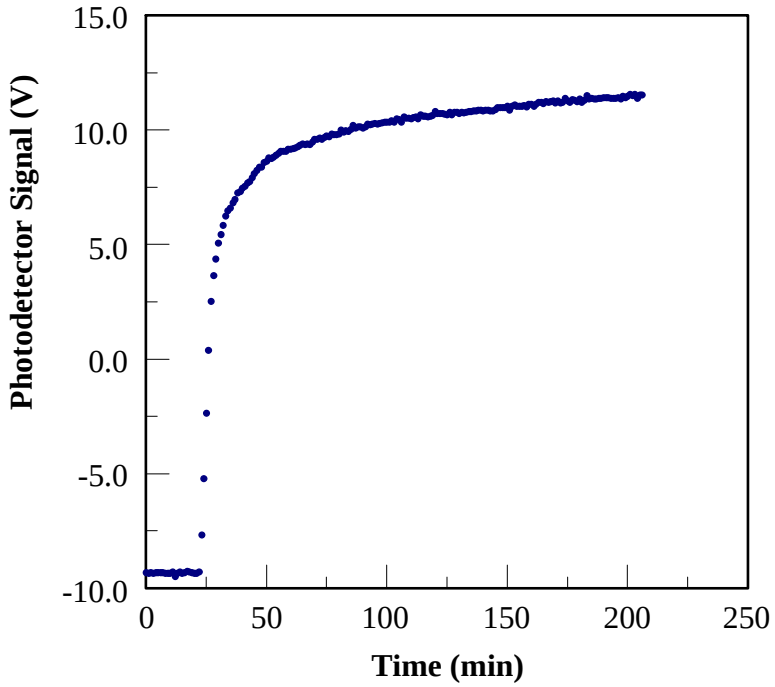

Figure 3.10. Sample curve from constrained sintering runs corresponding to film thickness shrinkage. The increasing nature of the curve is due to the optical path arrangement in the setup that produces an inverted trend.

3.4 Curvature Measurements

Curvature measurements were made using the constrained samples with thin silicon substrates. The sintering profile followed the general firing profile represented schematically in Figure 3.8 for constrained films. During sintering, the length of the sample was scanned by the laser beam by translating the hot stage by 2 mm. For each scan, a data set of detector voltage versus the translation distance was generated. The detector voltage was converted into the corresponding vertical position on the detector by a simple proportionality similar to that used in the film shrinkage measurements on the constrained samples. The processed results are similar to those plotted in Figure 3.11. For the particular setup shown in Figure 3.3, a convex camber will give a decreasing reading with translation distance (negative slope) while a concave shape will produce a positive slope.

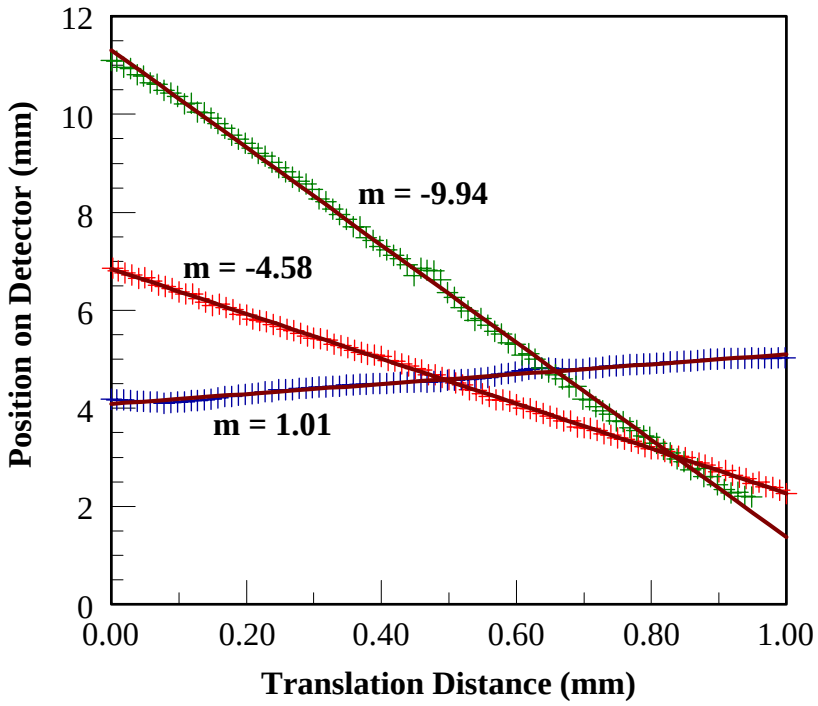

Figure 3.11. Sample plots of detector position versus translation distance from scans obtained during curvature measurements on constrained films (m = slope).

3.5 Characterization of Sintered Samples

The ZnO and glass-ceramic materials were examined using various analytical tools. Measurement of film thickness used to calculate the initial and final densities were performed using an optical microscope. A scanning electron microscope was used to obtain images of the green and sintered samples. Chemical analysis of the interface region in the constrained samples was done using an electron probe microanalyzer (EPMA). X-ray diffraction was performed on the sintered glass-ceramic samples to determine the progress of crystallization during sintering. Scanning acoustic microscopy (SAM) was also employed to obtain an area distribution of porosities in the glass-ceramic samples. Other instruments used include a picoammeter for determining the glass and glass-ceramic coating electrical resistivities, and impedance analyzer for obtaining the dielectric constants of the glass and glass-ceramic materials.

Chapter 4
Constrained Sintering of Zinc Oxide

In this chapter, the densification profiles of ZnO constrained on silicon substrate are presented along with corresponding densification curves for the freestanding tapes. The effect of substrate constraint on the densification is explored by comparing the densification rates and activation energies of the two types of samples. The in-plane stresses generated during sintering were also determined from curvature measurements on coated substrates to help explain differences in the densification behavior between free and constrained films of ZnO.

4.1 Results

The densification profiles for freestanding ZnO tapes are shown in Figure 4.1 and Figure 4.2. The former shows the entire profile, including the initial ramp up to the sintering temperatures, while, in the latter figure, the plots are truncated to the isothermal segments. The freestanding tapes had an initial relative density of 0.46 ± 0.2. The curves diverge from each other as soon as the sintering tapes reach their respective sintering temperature, indicating strong temperature dependence typical of solid-state diffusion controlled processes as described in the Chapter 2. The curves indicate a trend where samples fired at lower temperatures will not reach the density obtained at higher temperature.

Figure 4.3 and Figure 4.4 show the densification profiles of ZnO films constrained on silicon substrate. The constrained films also had an initial relative density of 0.46 ± 0.2. As was the case with the freestanding tapes, the curves began to diverge from each other as soon as the constrained film started to shrink, which again indicates strong dependence on temperature. As noted in the section 3.3, the densification comes

from the shrinkage through the thickness of the film such that the curves mirror the shape of the shrinkage curves in an inverse manner. A comparison with the densification curves for freestanding tapes show that the relative density of the constrained film always lags that of the freestanding samples at any of the sintering temperatures used. It also shows that the density of the constrained film is not likely to catch up with the freestanding film, e.g., the end point density will be lower as the curve settles into a very slow rate. This is similar to the observations made by Garino and Bowen[2]. A clear graphical comparison between the two conditions is illustrated in the combined isothermal densification curves at 950°C and 1000°C (Figure 4.5). The curve for a freestanding tape at 950°C is higher than that of a constrained film sintered at 1000°C. Possible reasons could include the evolution of the grain structure and differential sintering. If the grains experience significant growth over that of the initial particle size, then further pore removal is hindered.

The difference in the densification profiles is reflected in the sintered microstructures. The images obtained by a scanning electron microscope of a freestanding ZnO sample sintered at 1050°C for 3 hours are shown in Figure 4.6. The sample was polished and etched lightly with dilute acetic acid. The pictures clearly show the presence of pores resulting from incomplete densification. The grains have also grown beyond the submicron starting particle size by about an order of magnitude such that additional densification becomes more difficult. The corresponding images of the constrained ZnO film are shown in Figure 4.7. The microstructure is considerably more open giving a lower sintered density. The structure is also more “skeletal” in appearance with the sintered particles connected through narrow necks. This illustrates the difficulty to transport enough material to the neck region and the inability of the particles to rearrange and form the equiaxed grains found in the freestanding samples.

Both free and constrained samples attained relatively low final densities that are not fully explained by the low initial density of the powder compact. The powder undergoing annealing during binder burnout is an inadvertent effect which was observed by others when sintering zinc oxide[57]. The driving force arising from the sharp edges of the particles and high surface area-to-volume ratio is dissipated when the particles become more rounded and coarser. Images obtained from the same freestanding ZnO

that were sintered without going through a long isothermal burnout shows a noticeably denser microstructure as seen in Figure 4.8, although still not near full density. Upon closer inspection, the apparently dense areas actually include shallow voids or depressions that make them difficult to distinguish from the polished areas. However, the improvement in the sintered density is evident.

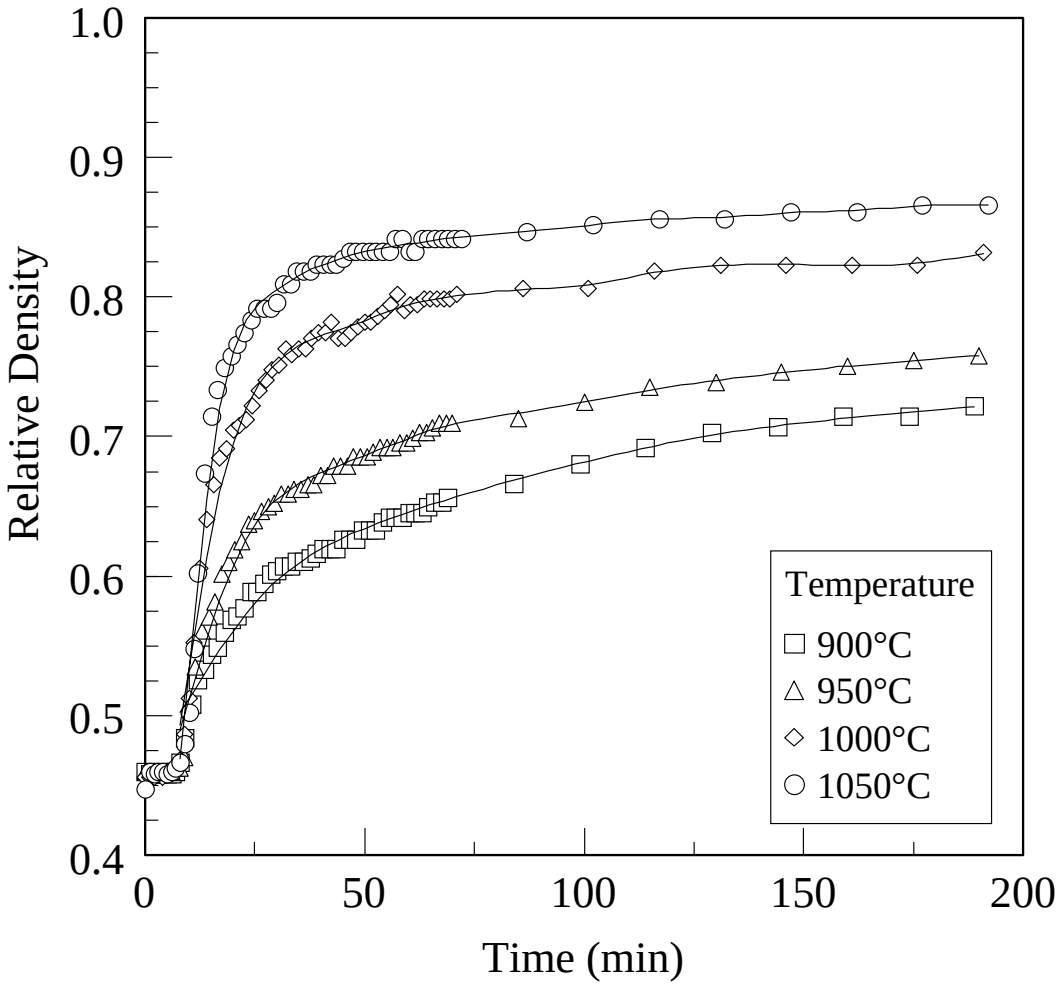

Figure 4.1. Densification profiles of freestanding zinc oxide tape at temperatures of 900°C to 1050°C with the non-isothermal segments of the curves included. Only half of the data points up to the first 60 minutes into the isothermal region are shown.

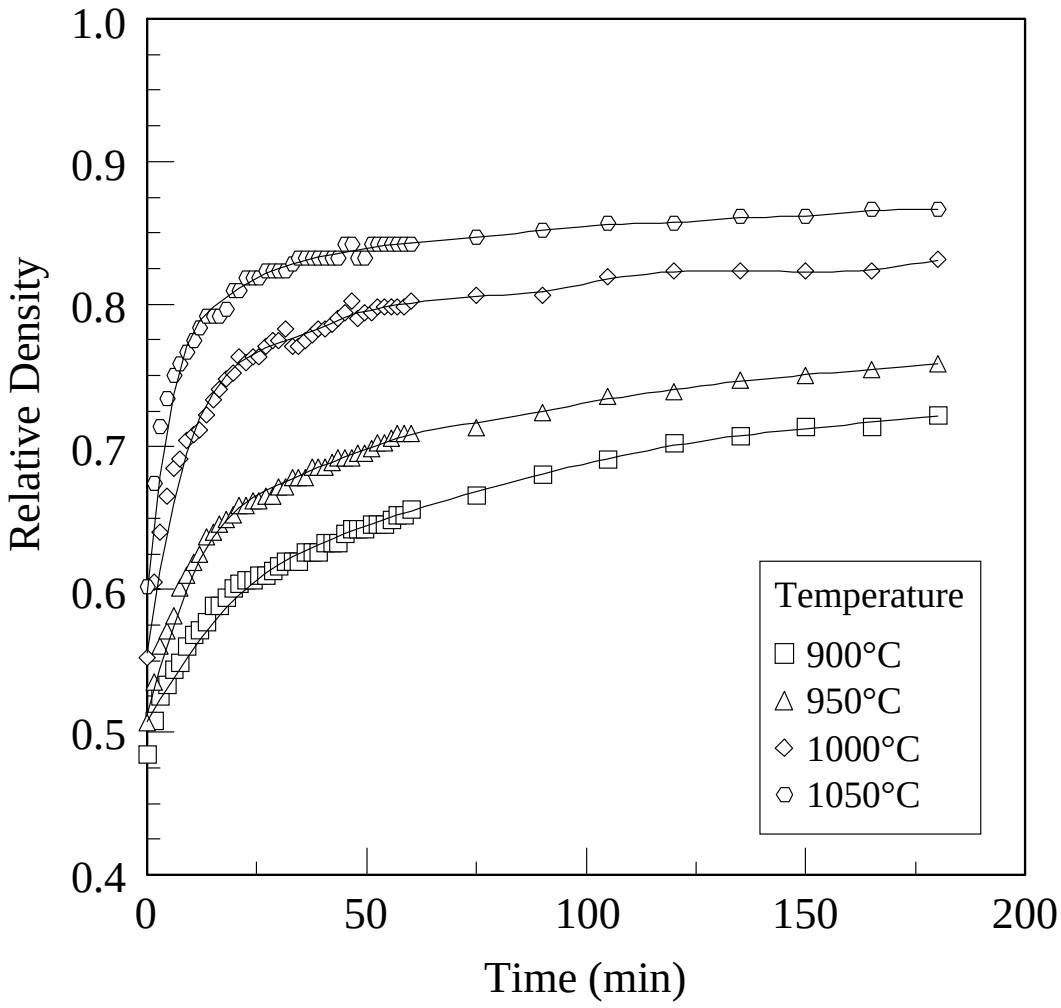

Figure 4.2. Isothermal densification profiles of freestanding zinc oxide from 900°C to 1050°C. Only half of the data points are plotted for clarity.

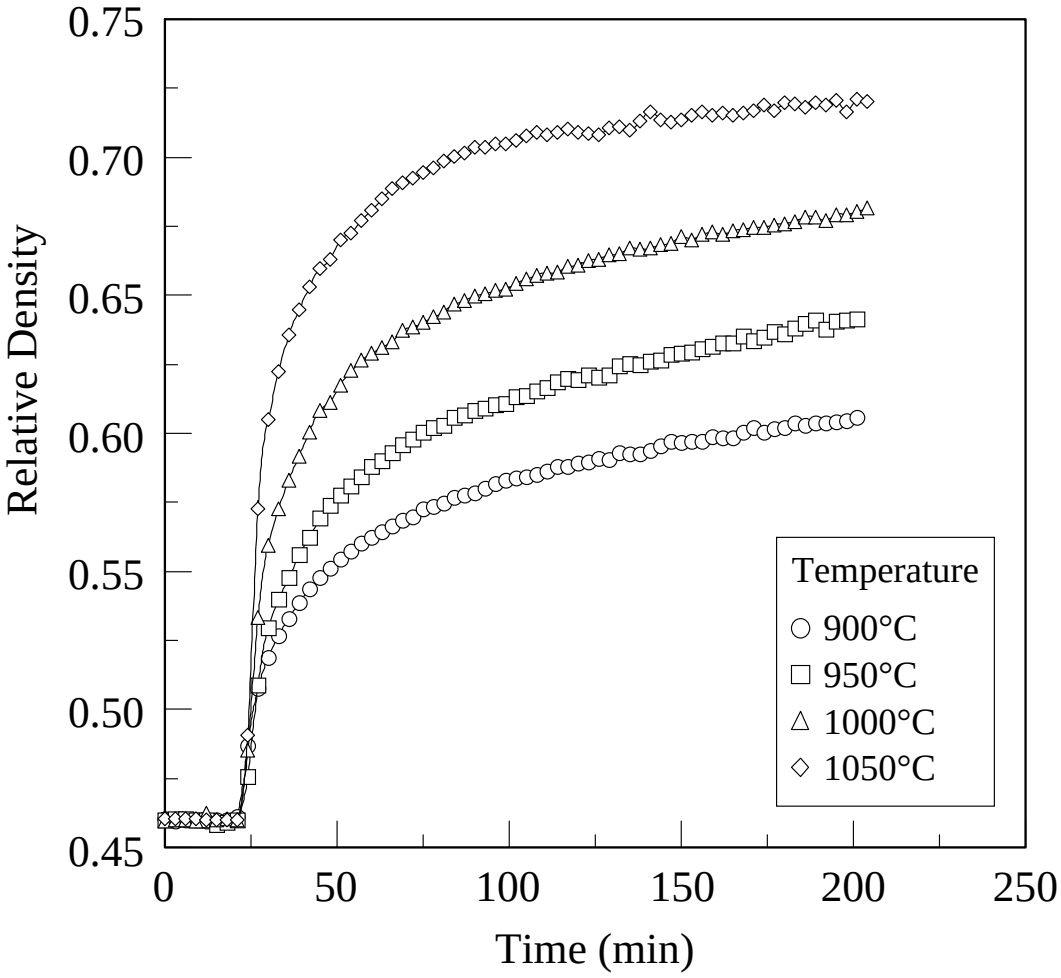

Figure 4.3. Densification curves of ZnO films constrained on silicon substrate at temperatures of 900°C to 1050°C, including the initial non-isothermal segments. Only a third of the data points are shown for clarity.

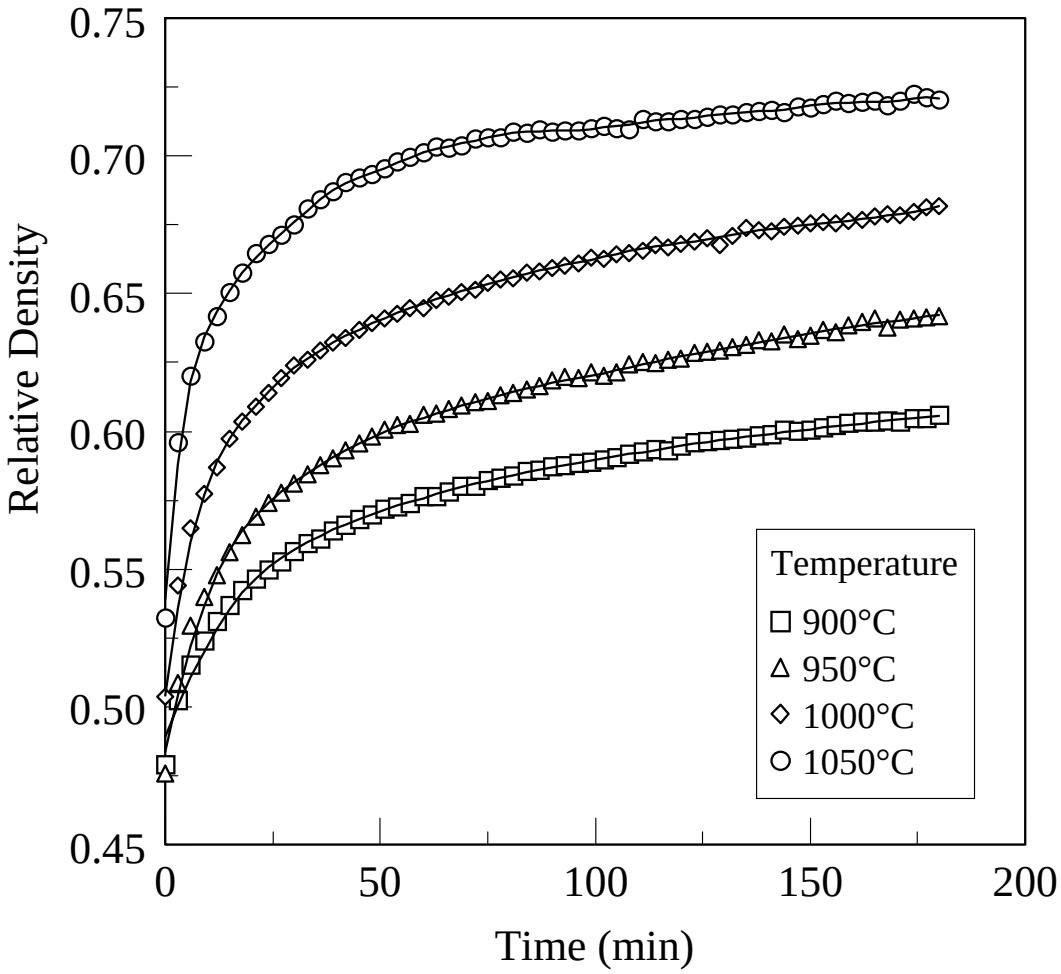

Figure 4.4. Isothermal densification curves for ZnO films constrained on 20-mil silicon substrate at temperatures of 900°C to 1050°C. Only a third of the data points are shown for clarity.

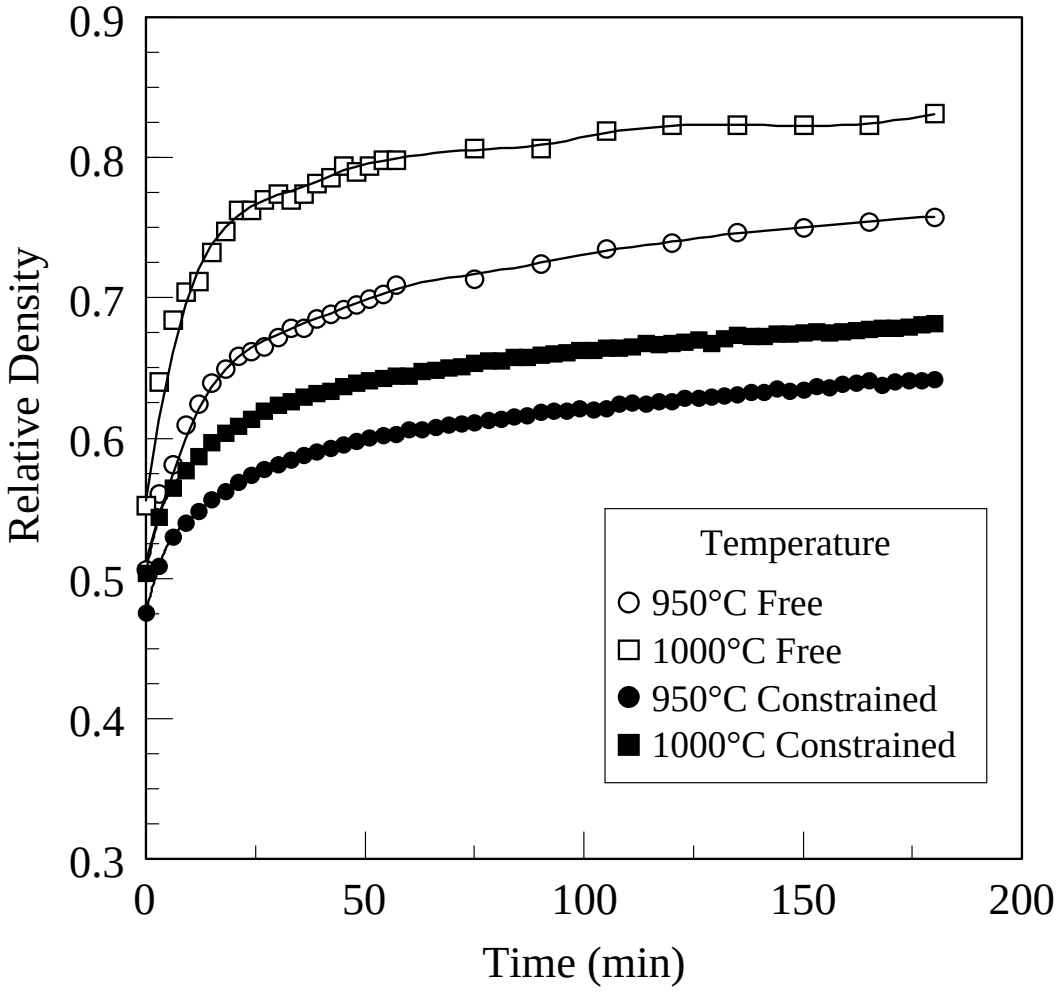

Figure 4.5. Combined isothermal densification curves for freestanding and constrained ZnO at 950°C and 1000°C.

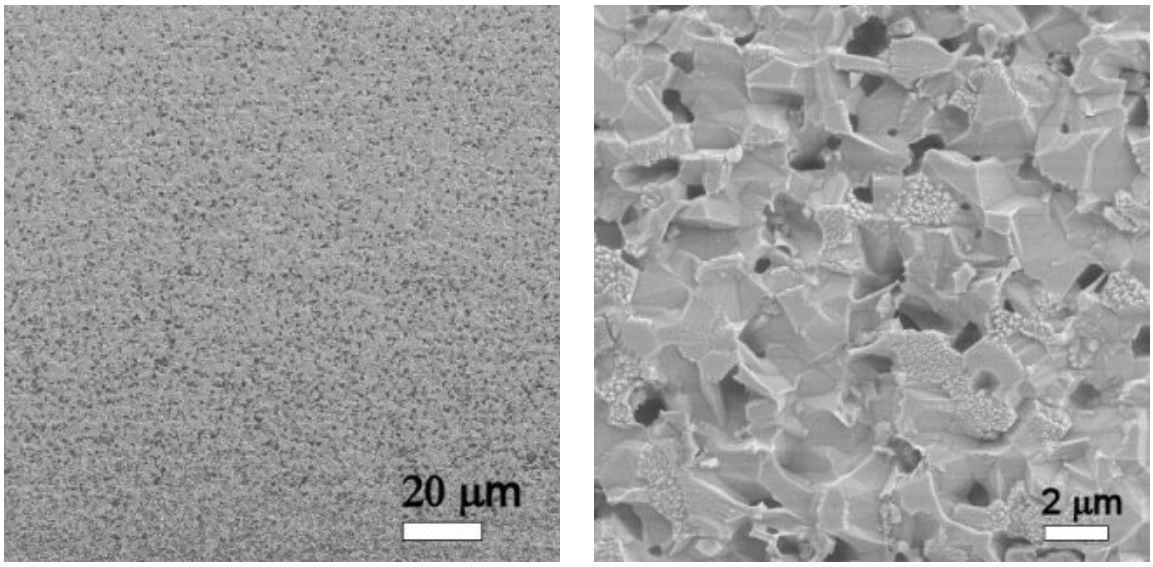

(a) (b)

Figure 4.6. SEM image of the microstructure of freestanding ZnO sintered at 1050°C for 3 hours at (a) 1000X magnification and (b) 10,000X magnification.

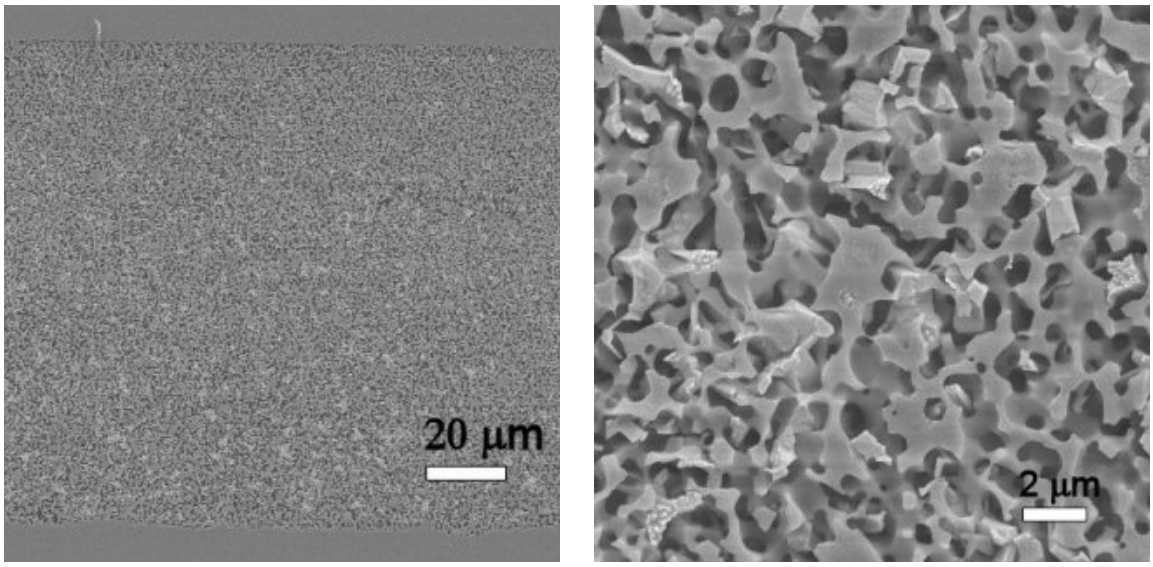

(a) (b)

Figure 4.7. SEM image of the microstructure of ZnO constrained on silicon sintered at 1050°C for 3 hours at (a) 1000X magnification and (b) 10,000X magnification.

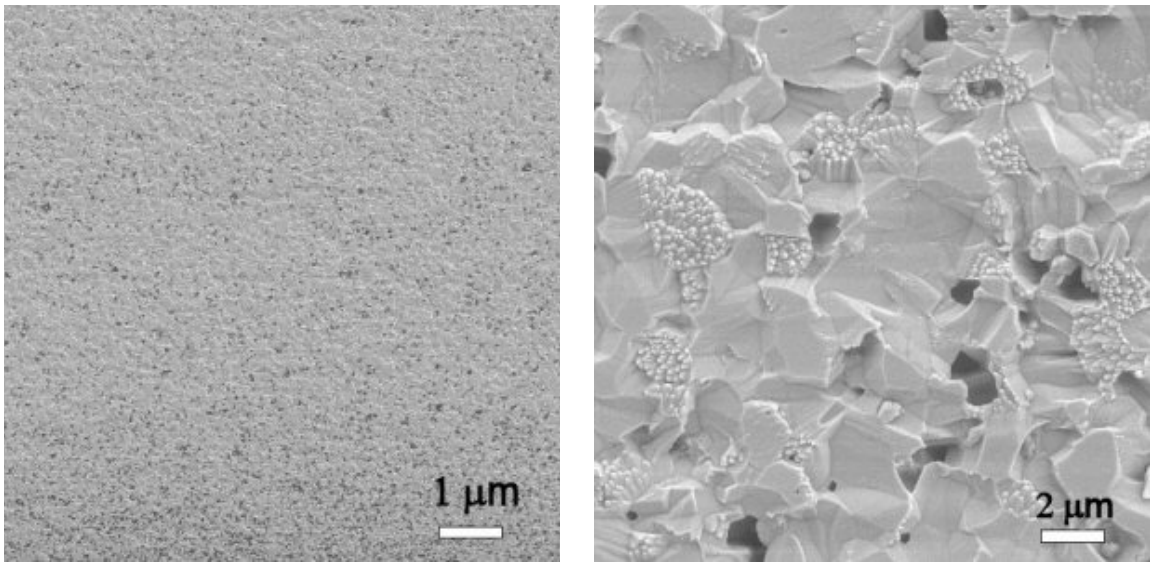

(a) (b)

Figure 4.8. SEM image of the microstructure of freestanding ZnO sintered at 1050°C for 3 hours without undergoing an isothermal binder burnout before sintering: (a) 1000X magnification and (b) 10,000X magnification.

The curvatures of the thin silicon substrates coated with a layer of ZnO powder were obtained for temperature above 900°C and are shown in Figure 4.9. The coating induced an initial curvature on the substrate during drying as seen in the early segment of the plots. Upon rapid heating to the isothermal regime, the bilayer underwent a curvature reversal, which is an indication of a momentary temperature gradient across the thickness of the sample. The bottom, which was adjacent to the setter, became hotter such that it expanded relative to the top layer. Once the temperature had equilibrated, the curvature returned and increased beyond the original curvature as the film experienced fast shrinkage. Once film shrinkage had slowed considerably, the curvature started a gradual decay.

To ensure that the curvature is not being generated by a reaction between the ZnO and the silicon substrate at the sintering temperature, the interface region where the sintered coating came off was analyzed by electron probe microanalysis (EPMA). A composite of the x-ray image for each element that was present at the interface is shown in Figure 4.10. A thin layer of less than 1 μm shows the presence of zinc and oxygen (gray region) adjacent to the silicon. A large part of ZnO detected on the surface was

most likely the residual material left behind after the coating was debonded. The ZnO film was only weakly adherent to the substrate and quickly came off, although the adhesion was sufficient to prevent lateral shrinkage. Any discoloration of the silicon substrate was very slight and the optical polish of the surface was hardly diminished. Therefore, the observed curvature was not likely to have come from reaction at the interface nor was it significantly affected by any such occurrence.

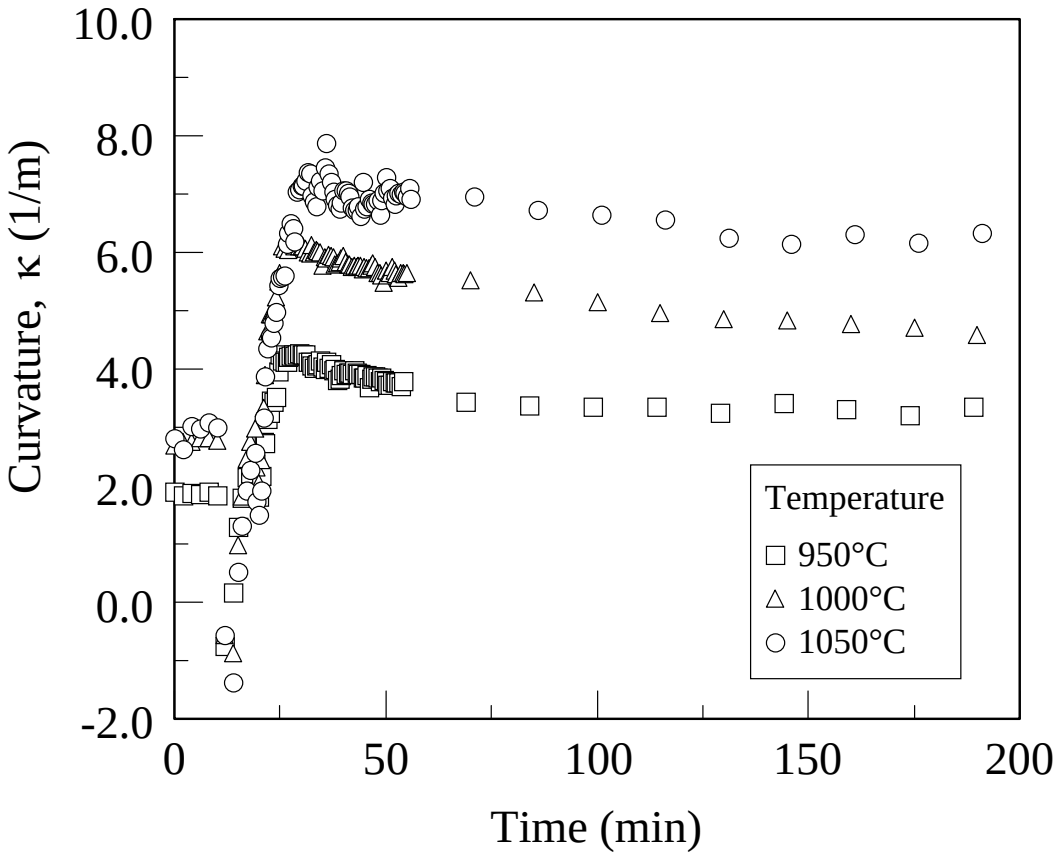

Figure 4.9. Curvature calculated from the slope of the detector position versus scan length line for various sintering temperatures.

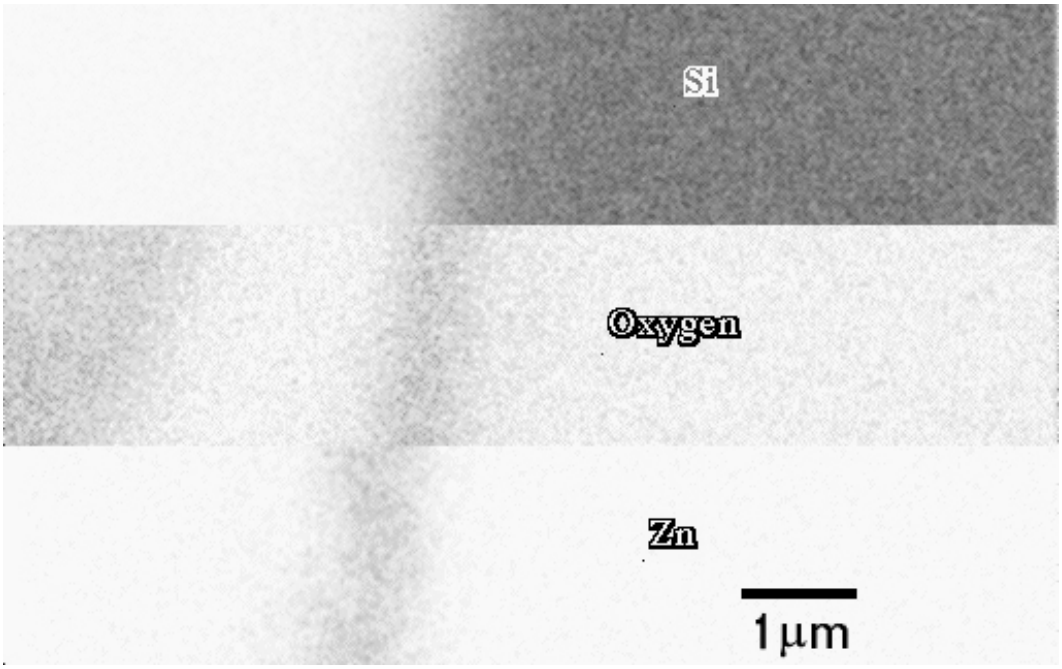

Figure 4.10. Composite image of the elemental distribution at the sintered ZnO/silicon substrate interface region obtained by electron probe microanalysis (EPMA). Dark regions indicate the presence of the element being detected.

4.2 Discussion

Both freestanding and constrained films exhibited similar behavior when subjected to different heating temperatures with the curves diverging at the point where the isothermal condition is attained. However, the progress of the densification process is severely hindered in the constrained film. Constrained sintering experiments on gold films[58] showed a similar tendency of reduced densification rate right from the outset of densification. On the other hand, Bang and Lu observed that constrained glass films[3] had almost the same densification rate as the freestanding films until a density of around 90% when the curves finally diverged. The effect of constraint has been investigated to try to explain the reduced densification rates. The constraint may be in other forms than a flat substrate such as rigid inclusions[50,59-62] and reinforcing fiber in a composite[63]. The reduced densification could come from mechanical constraint on the particles that affects the mobility of the grain boundaries and the prevailing diffusion

mechanisms[6], interference on the microstructural development[59], and stresses that build up during shrinkage that opposes the sintering potential[38,61].

In a crystalline material, the competition between the densifying and coarsening (non-densifying) is important because of the presence of grain boundaries. The following scenario was formulated by Bordia and Scherer[6] to explain how constraint will affect the densification process. Consider the situation depicted in Figure 4.11. In an unconstrained film, the particles are able to shrink in all directions such that the resulting structure will have equiaxed grains. In a constrained film, the necks or contact points between particles will be subjected to different stresses depending on their orientation in the film. The coating can be imagined to be a detached film that is being stretched along the planar directions. The neck (or boundary) B will be under a tensile stress while neck A will be under a compressive stress. Because the neck at B has not grown as fast as it would if there were no stresses, the boundary at A will become mobile even at lower density than it would be without stresses. If the boundary leaves behind the neck region, further densification would be difficult or may cease altogether trapping the porosity within the grain. Meanwhile neck B is immobilized by the substrate constraint. In principle, if the porous film attains sufficient density to allow significant grain growth, anisotropic grain growth should be observed. The grain size normal to the substrate should be larger than the grain size parallel to the substrate plane.

Even without grain boundary movement, neck A will still lose its curvature at low density, and, hence, the driving force necessary for matter transport. Any further densification will require the movement of atoms from the center of neck A to the pore region in B as shown by the curved arrow in the bottom right schematic of Figure 4.11, which is a longer path than the neck center-to-surface distance shown by the straight arrow. Since the densification rate of crystalline materials is more sensitive to the diffusion distance than amorphous materials as discussed in Chapter 2, retardation of sintering should be more pronounced. Any change in the transport mechanism should also be manifested by a corresponding change in the associated activation energy of densification.

Further reduction in the driving force for densification can occur by coarsening mechanisms. Since center-to-center approach along the plane of the substrate is hindered

by the constraint, the neck at B will be flattened by the transport of matter from the surface, which results in neck growth but not densification. Further densification can only occur if matter is transported from the grain boundary in A to the pore in B.

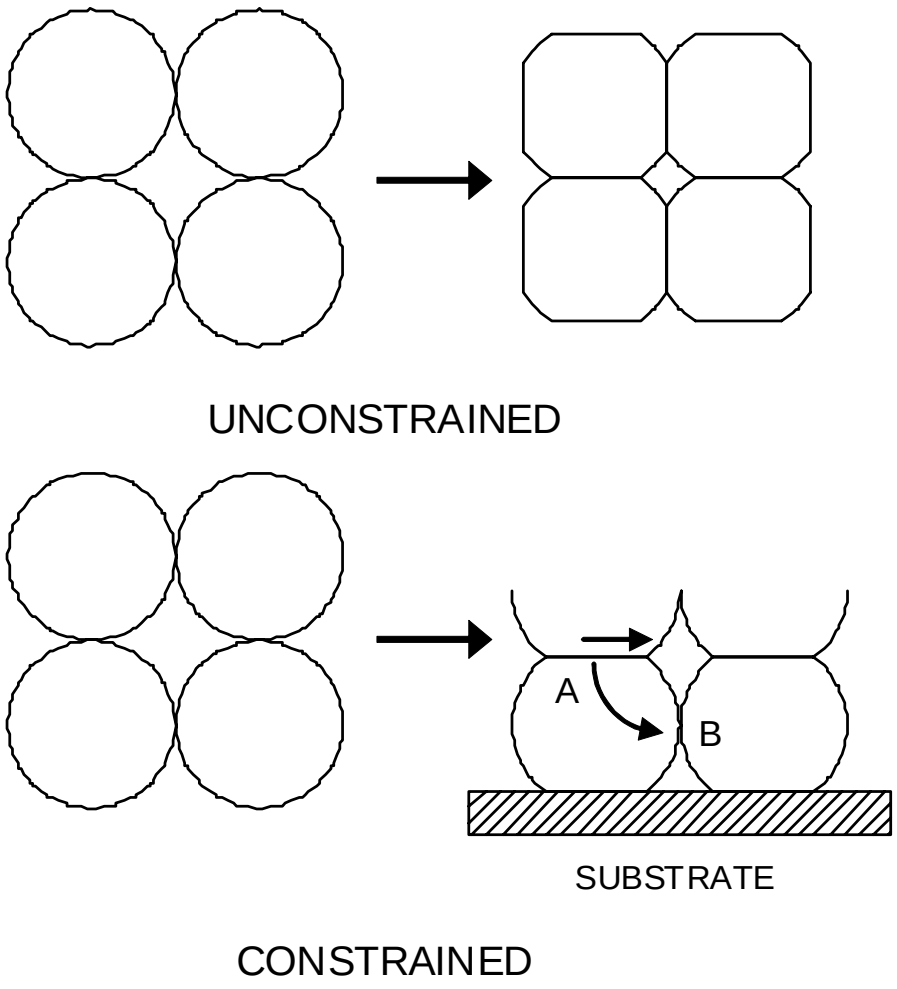

Figure 4.11. Schematic of an idealized arrangement of particles undergoing sintering uder free and constrained conditions.

The scenario(s) discussed above need not be limited to substrate constraint. The constraint may be in the form of inclusions, which may be considered as a miniature substrate. Sudre, et al. [59,60,64] proposed a model to explain the significant reduction in the sintering of polycrystalline materials with rigid inclusions based on observations of

the evolution of the microstructure of alumina matrix composites with ZrO_2 inclusions. Stress fields due to differential densification leads to premature densification in certain regions between inclusions. The premature densification and the associated grain growth will lead to the development of dense regions that resists densification such that severely reduced densification will occur in outlying regions, which are under tensile stresses.

Since the constrained films did not achieve enough density to allow clear observation of anisotropic grain growth, explanation of the retarded densification will have to come from the other associated phenomena. The densification rate of the constrained film should be substantially lower throughout except, perhaps, near the highest density attained when both rates slow down considerably. Given the argument about the change in the path of matter transport, the associated activation energy should also be different in the constrained film, at least at the lower densities where the particle packing will prevent further mechanical rearrangement of the particles. To hinder lateral approach of the particle or grain centers, the constraint should generate sufficient stress of the order of magnitude of the sintering pressure, especially during the early stage to produce the observed deviation between the densification profiles. These three items are examined individually in the following sections.

Densification Rates

The isothermal densification rates at various temperatures for freestanding ZnO are shown in Figure 4.12. The curves were obtained by taking the derivative of the densification curves in Figure 4.2. During the early stages when the density is still low, the rate is at its highest. This is followed by a steady decline until it drops to a very low value not too long into the isothermal regime. There is a large spread in the initial densification rates with the top sintering temperature of 1050°C having a rate 5 times greater than that at 900°C. The corresponding densification rates for constrained films are shown in Figure 4.13. The trend mirrors that of the freestanding case but the rates are substantially lower. This is clearly seen in Figure 4.14, where the densification rates of the unconstrained films approximately doubled up on the constrained film rates.

When plotted against relative density, the effect of temperature and constraint are even bigger. Taking 60% relative density as the reference density, the rate at 1050°C

jumped to around 20 times that of 900°C in the case of a freestanding film (Figure 4.15). For the constrained case, a similar effect is observed (Figure 4.16) although it is slightly less at the lower densities. A comparison of the densification rates of freestanding and constrained films (Figure 4.17) shows those of the constrained film lagged behind those of the free films up to the higher densities. At 60% relative density and at 950°C, the freestanding film densified around 15 times faster and, at 1000°C, by about 10 times faster than the constrained film. Given such difference in densification rates, it is very likely that the two types of films are densifying under different mechanisms. The activation energies should be different for the two films if such is the case.

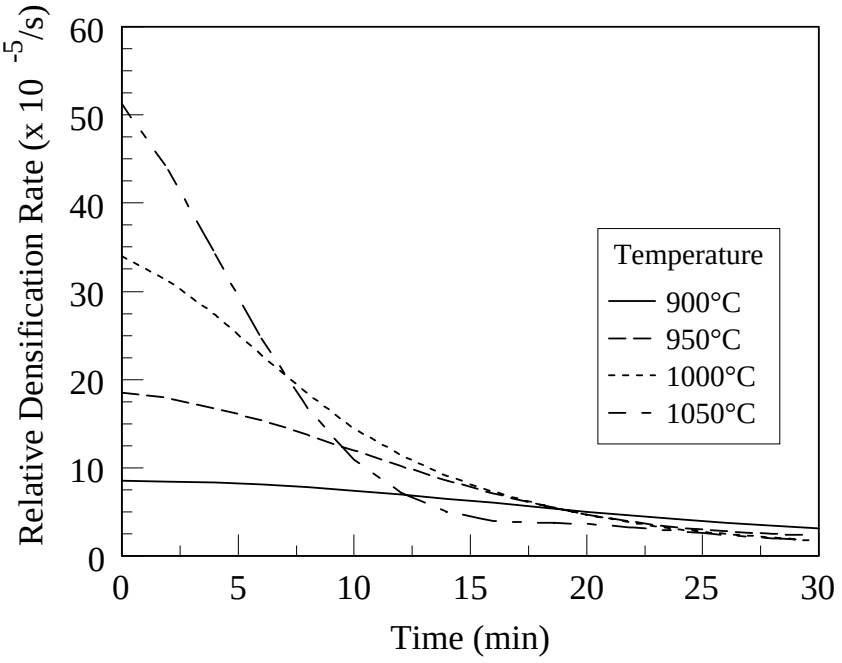

Figure 4.12 Densification rate of freestanding ZnO films sintered from 900°C to 1050°C.

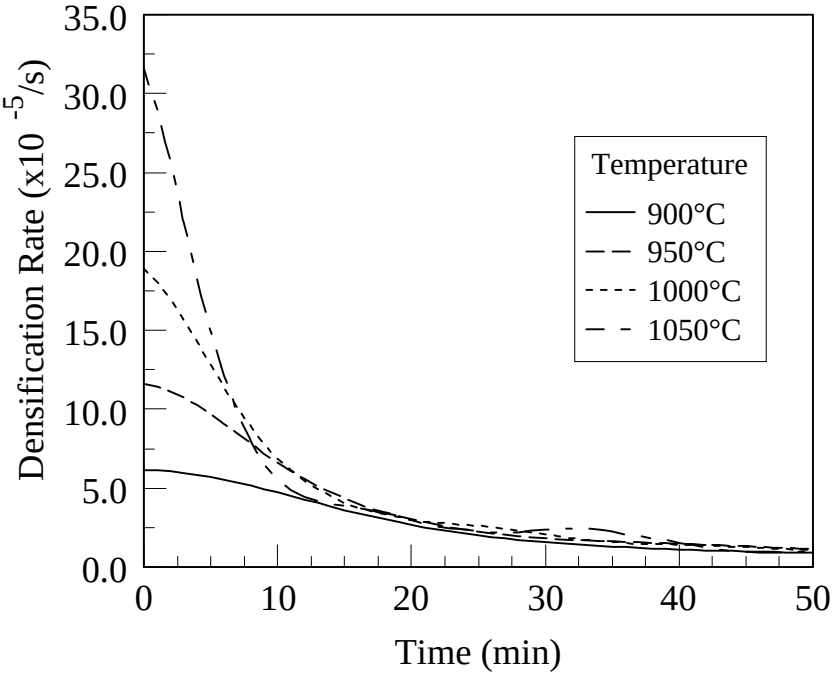

Figure 4.13. Densification rates of ZnO powder films constrained on silicon substrate sintered from 900°C to 1050°C.

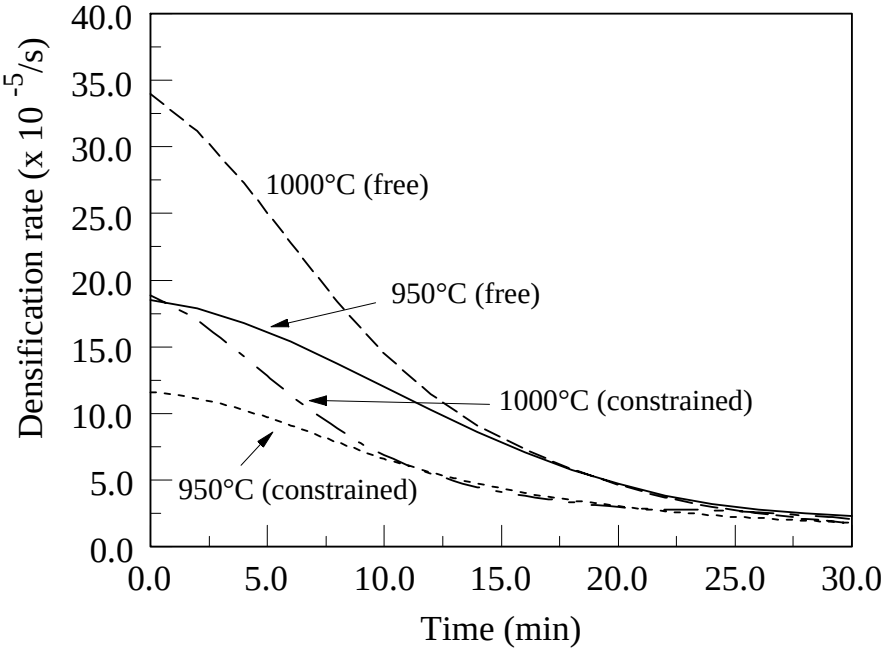

Figure 4.14. Comparison of the densification rates of freestanding and constrained ZnO films at various temperatures.

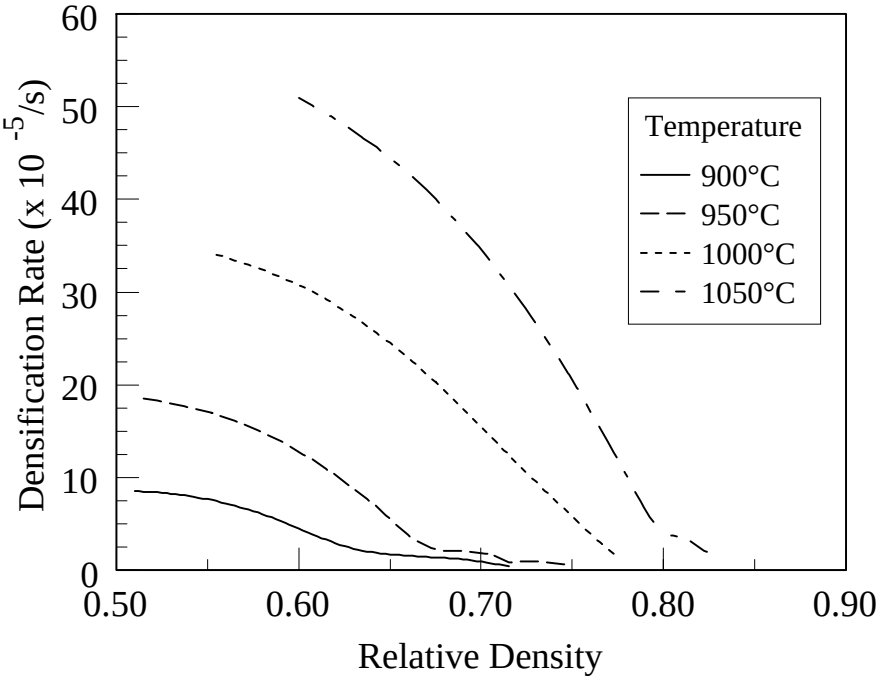

Figure 4.15. Densification rates of freestanding ZnO film as a function of sintered relative density for sintering temperatures of 900°C to 1050°C.

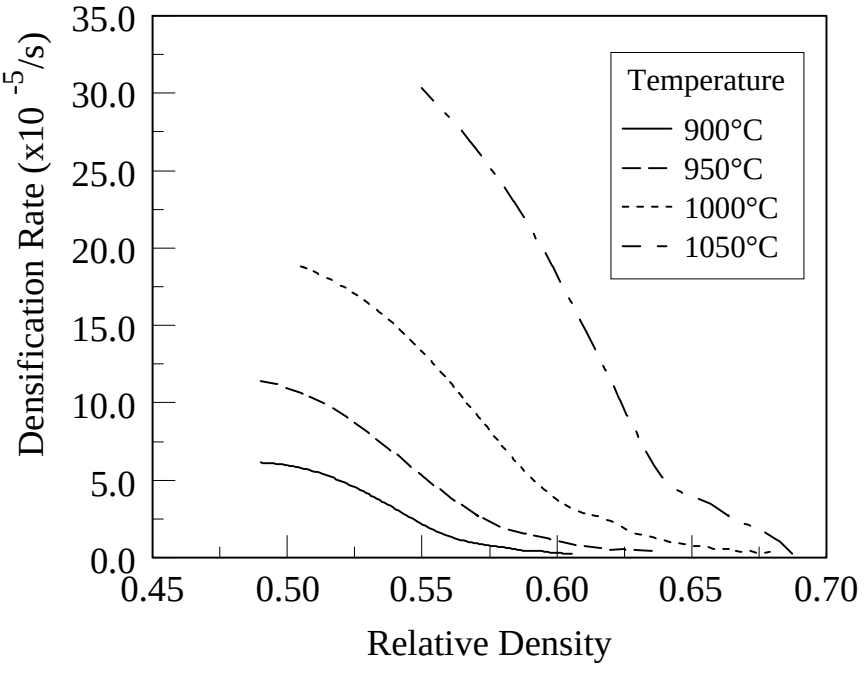

Figure 4.16. Densification rates of constrained ZnO film versus sintered relative density for temperatures ranging from 900°C to 1050°C.

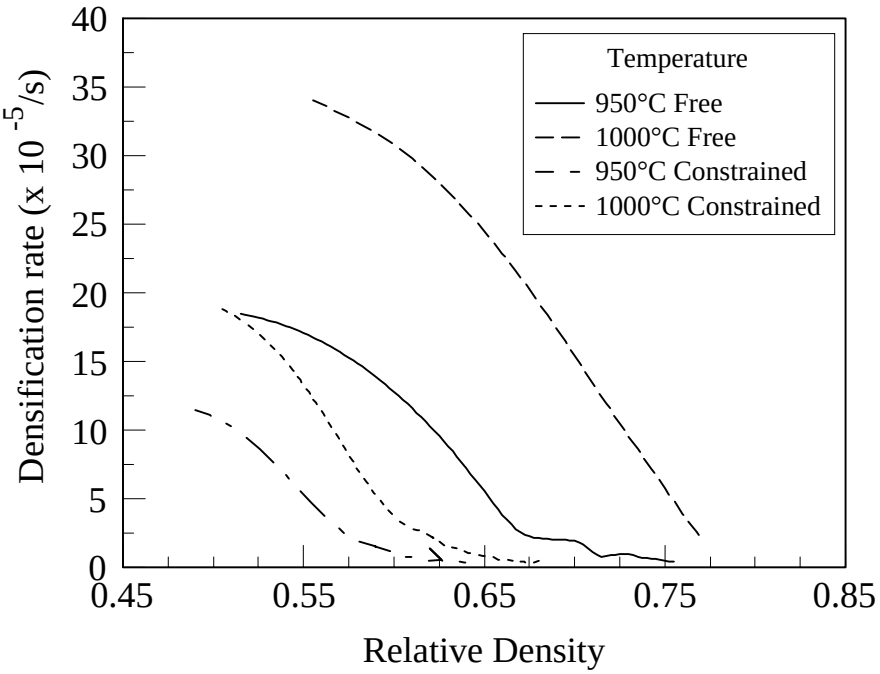

Figure 4.17. Comparison of the densification rates of freestanding and constrained ZnO films versus density for sintering temperatures from 900°C to 1050°C.

Activation Energy

Since ZnO is a crystalline material, the appropriate mechanisms for densification would be the solid-state diffusion processes as described in Chapter 2. For either grain boundary or lattice diffusion, the densification rate would be related to the diffusion and temperature by the following proportionality with the other parameters kept constant.

$$\frac{1}{\rho}\frac{d\rho}{dt} = \dot{\bar{\rho}} \propto \frac{D}{T} \qquad (4.1)$$

The term D is the diffusion coefficient and in turn is related to the temperature and the activation energy, Q, by the equation

$$D = D_o \exp\left(-\frac{Q}{RT}\right) \qquad (4.2)$$

where R is the gas constant. The densification rate is therefore related to Q through

$$\dot{\bar{\rho}} \propto \frac{1}{T}\exp\left(-\frac{Q}{RT}\right) \qquad (4.3)$$

such that

$$\log\left(\dot{\bar{\rho}} \times T\right) \propto -\frac{Q}{2.303RT} \tag{4.4}$$

An Arrhenius-type plot of Eq. (4.4) should produce a straight line with the slope equal to $-Q/2.303R$, from which the activation energy of the process can be obtained. Taking the data for the freestanding film in Figure 4.15, a plot such as that shown in Figure 4.18 is obtained. For the densities shown in the figure, the apparent activation energy is 242 ± 21 kJ/mole. This value is in close agreement with several other measurements reported in the literature. Martin and Rosen[65] determine Q to be 240 kJ/mole ± 10% for different pore fractions and under different heating rates. Perazolli, et al.[66] studied the coarsening kinetics of ZnO under constant heating rate and determined the activation energy for coarsening of 210 kJ/mole, which was in good agreement with densification activation energy, suggesting that the same mechanisms control both processes. Perazolli, et al.[67] also studied the initial stages of the sintering of ZnO and concluded that grain boundary diffusion was in control for shrinkages ranging from 3 to 6% , with an apparent activation energy of 220 kJ/mole. For a structure where the pores remain interconnected, it is reasonable that the densification is controlled by grain boundary diffusion.

Applying the same procedure to constrained films, the logarithmic plot was obtained using the data in Figure 4.16. The calculations for densities from 60 to 64% are shown in Figure 4.19. The apparent activation energy for this range of densities is 391 ± 34 kJ/mole. This is at least 50% greater than the activation energy obtained from free sintering. Positron studies made by Fernandez, et al[57] yielded an activation energy for sintering of 360 ± 10 kJ/mole, in good agreement with Gupta and Coble[68]. The higher activation energy obtained from the constrained film at the same density range could indicate a change in the dominant mechanism as predicted by Bordia and Scherer[6]. At lower densities, the activation energy dropped to around 300 kJ/mole at 57% density as shown in Figure 4.20. At lower densities, it is possible that other mechanisms, including non-diffusional processes such as particle rearrangement, could be taking place concurrently. Structural rearrangement was found by Perazolli, et al[67] to dominate at very low shrinkages of up to 1.5% with an apparent activation energy of 290 kJ/mole.

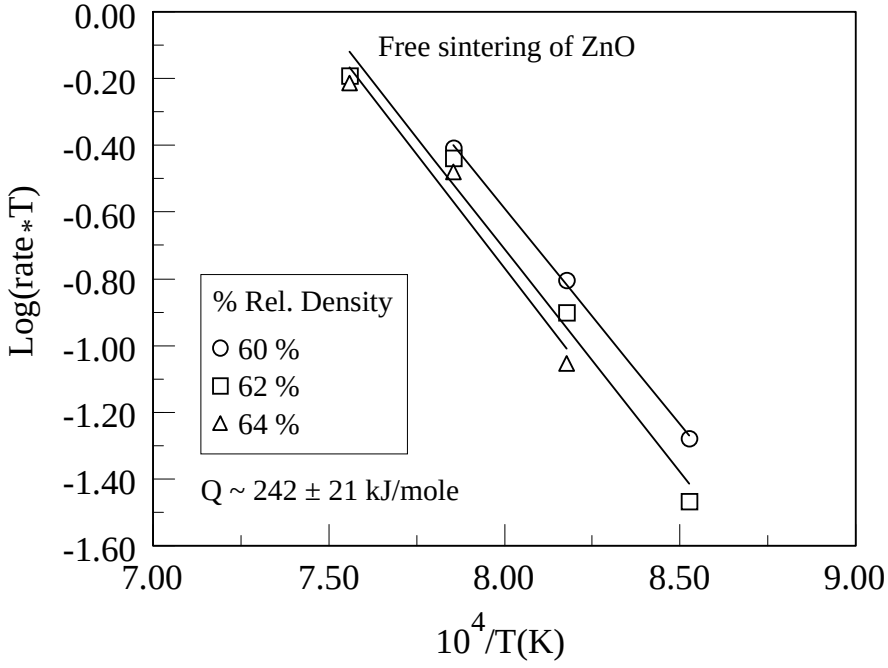

Figure 4.18. Plots of rate function versus 1/T at constant densities for the freestanding ZnO films.

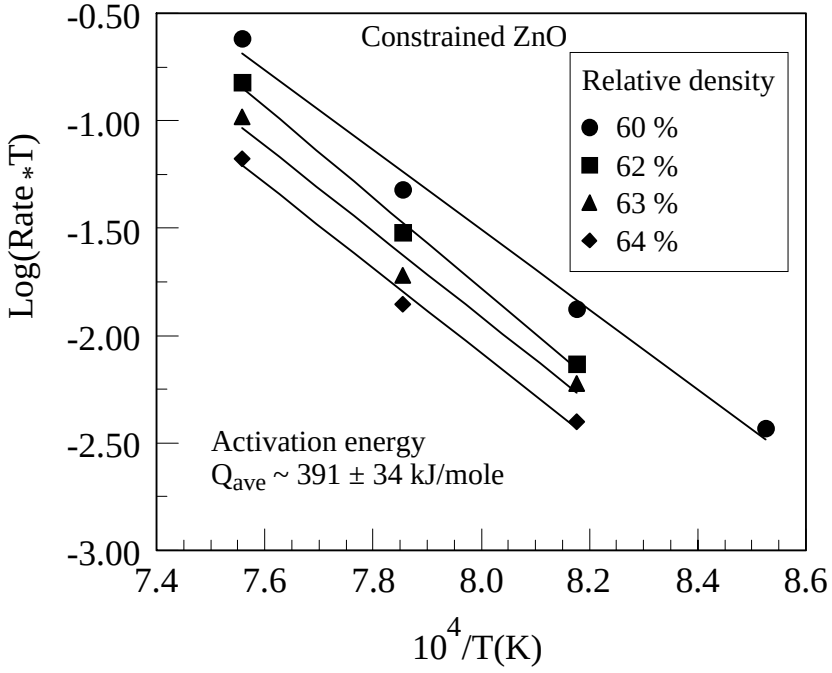

Figure 4.19. Plot of rate function versus 1/T at various sintered densities for constrained ZnO films.

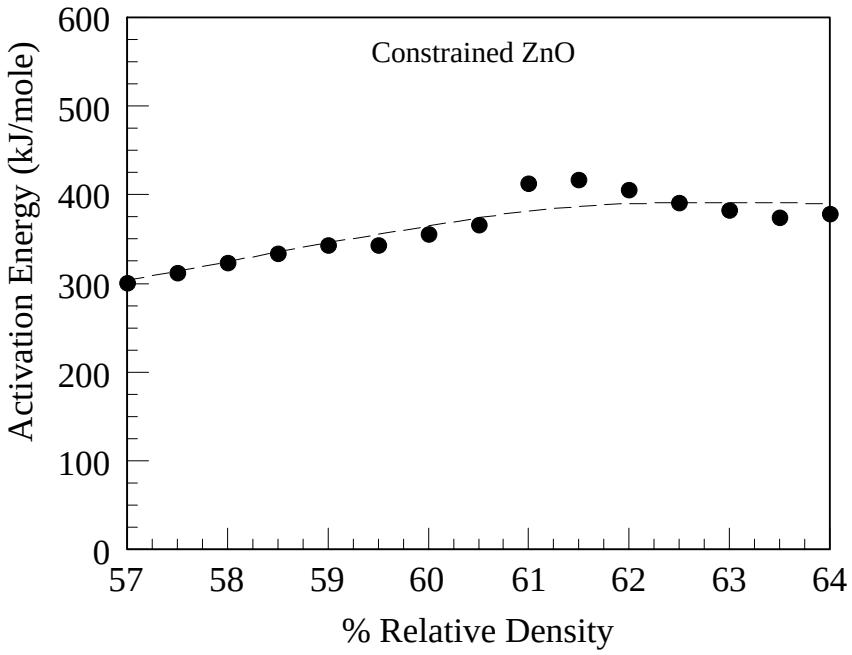

Figure 4.20. Variation of the activation energy for densification with sintered relative density for a constrained ZnO film.

Determination of In-plane Stresses in the Constrained Film

The in-plane stresses were determined by combining the results of the film shrinkage and curvature measurements. Calculation of the corresponding stress values was done using a modified form of the Stoney formula [54] as discussed later.

Film Shrinkage and Density

The film shrinkage curves with sintering time at different temperatures (950, 1000 and 1050°C) are shown in Figure 4.21. Although there is a relatively large shrinkage, the final relative density does not come close to the full density even for the film fired at 1050°C (Figure 4.22). Because of the relatively large film shrinkages involved, the change in film thickness from the initial values must be taken into account when calculating the stresses.

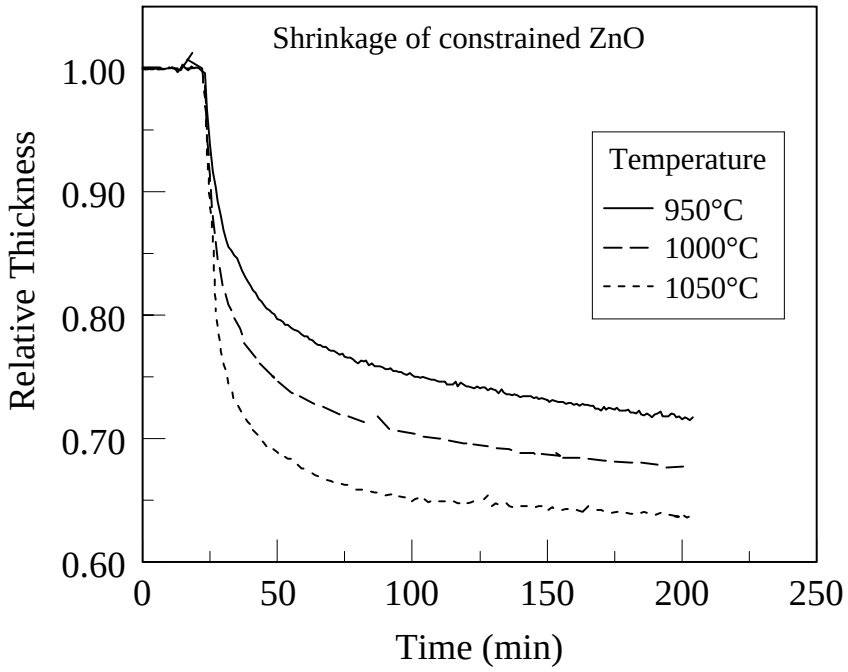

Figure 4.21. Relative thickness of constrained ZnO film undergoing sintering at various temperatures.

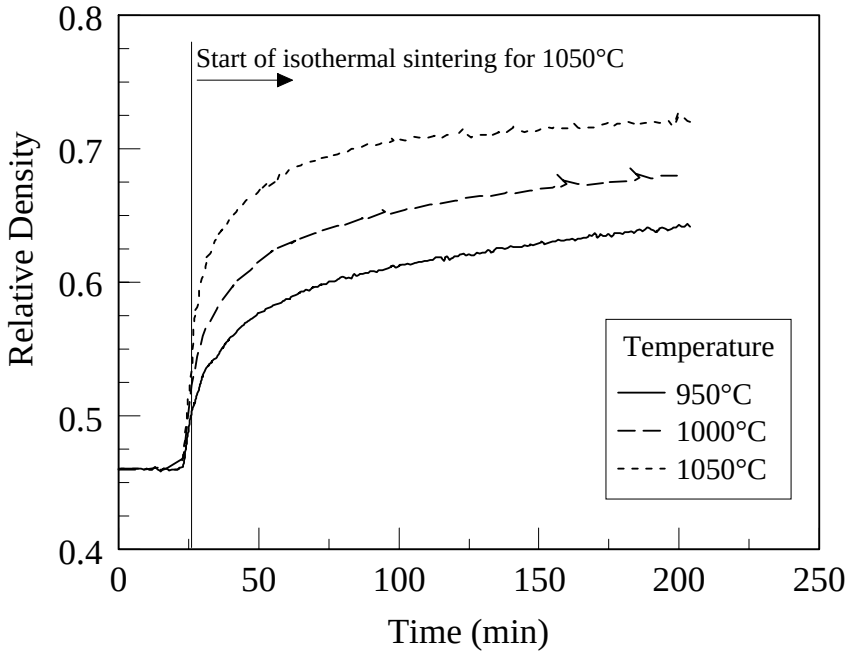

Figure 4.22. Relative density curves for ZnO films on silicon substrate calculated from the film thickness shrinkage curves.

Curvature during Sintering

The geometric representation of the setup in Figure 3.3 is shown in Figure 4.23. The sample curvature was extracted from the signal detector position versus substrate scan position data using the proportionality relationship derived from Figure 4.23 which is written as follows.

$$\frac{D}{X} = \frac{L - \left(R/2 - \sqrt{(R/2)^2 - X^2} \right)}{\sqrt{(R/2)^2 - X^2}} \tag{4.5}$$

where X is the relative substrate position of the laser beam, D is the relative detector position of the signal, L is the distance between the substrate and the detector plane, and R is the radius of curvature. The scan length (X on substrate) was very small (2 mm) when compared to the distance between the substrate and the detector (0.85 m) and the radius of curvature, such that for X << R/2, the equation reduces to

$$D \approx \left(\frac{2L}{R} \right) X \tag{4.6}$$

The quantity (2L/R) is the slope (m) of experimental D vs. X line. The curvature, κ, can be calculated from the slope using the following equation:

$$\kappa = \frac{1}{R} \approx \left(\frac{m}{2L} \right) \tag{4.7}$$

A concave shape, such as the one shown in Figure 4.23, will give a positive slope and will correspond to a compressive stress on the film. A convex shape will have a negative slope and corresponds to a tensile stress on the constrained film.

Plots of the curvature versus sintering time for different temperatures were shown previously in Figure 4.9. The curvature of the samples underwent a momentary reversal (convex to concave) once the temperature started its rapid climb towards the sintering temperature. This reversal has nothing to do with the densification since, at this point, the films have not begun to densify. Uneven heating caused a temporary temperature gradient across the sample thickness resulting in a transient thermal expansion mismatch-induced stress. The curvature continued climbing in a near linear pattern and reached a

maximum once the shrinkage rate decreased appreciably. This is followed by a gradual decline in the curvature during the rest of the sintering run, resembling a slow exponential decay.

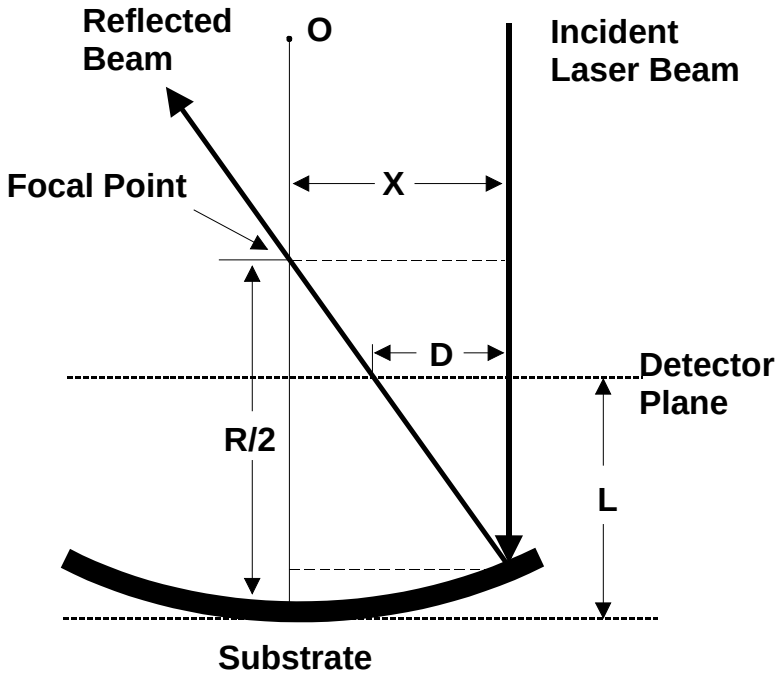

Figure 4.23. Schematic of the geometry used to obtain the relationship between the slope of detector position versus scan length and the sample curvature.

Calculation of In-plane Stress

The in-plane stresses were estimated from the shrinkage and matching curvature data using a modified form of the Stoney equation,

$$\sigma \cong \left[\frac{\kappa E_s d_s^2}{6(1-\nu_s)d_f(t)}\right]\left[\frac{d_s}{d_s + d_f(t)}\right] \tag{4.8}$$

where κ is the curvature, E_s is the Young's modulus of the substrate, ν_s is the Poisson's ratio of the substrate, and d_s and $d_f(t)$ are the substrate and film thickness, respectively. In Eq. (4.8), the first term in parenthesis is the well-known equation for thin film stress. The second term, which was dropped in the original derivation[54], was added back because the film thickness was comparable to the substrate thickness. It should be noted that the film thickness (d_f) is now a function of time instead of a constant value and

indicates that the thickness is changing as the sintering progresses. Equation (4.8) may also be expressed in terms of the relative density of the sintering film using the relationship between the film thickness and relative density, and is as follows

$$\sigma \cong \left[\frac{\kappa E_s d_s^2}{6(1-\nu_s)d_0}\right]\left[\frac{1}{\bar{\rho}_o/\bar{\rho}(t)}\left(\frac{d_s}{d_s + d_o(\bar{\rho}_o/\bar{\rho}(t))}\right)\right] \tag{4.9}$$

where $\bar{\rho}_o$ and $\bar{\rho}(t)$ are the initial and time-dependent relative densities of the film, respectively. The Young's modulus was compensated for the temperature change during sintering based on the temperature profile using data for the <110> direction by Ono, et al.[69]. The value of the Poisson's ratio hardly changed with temperature and was taken to be 0.226[70].

The in-plane stress curves are shown in Figure 4.24. The curves are replotted in Figure 4.25 with the initial stresses offset to zero to show the magnitude of the stress increase for each temperature. Positive values correspond to a tensile stress on the sintering film while negative values are compressive. An initial stress exists in each of the samples, which was the result of drying shrinkage of the slurry coating on the silicon substrate. The in-plane stress curves essentially followed the trend of the sample curvatures. The stress underwent a momentary reversal into the compressive regime (on the sintering film) as the temperature increased rapidly towards the sintering temperature starting at the 10-minute mark on the graph. Since no film shrinkage took place during this stage, the reversal was the result of a non-uniform temperature across the bilayer as the bottom layer temperature increased more rapidly because it was in physical contact with the setter. This reversal was followed by a rapid increase in the stress back into the tensile regime. The stress-temperature profile is not as linear as the corresponding curvature profile.

As the sample temperatures moved into the isothermal sintering regime, with a corresponding increase in density, the stress curves developed a kink where the stress actually dropped slightly or remained unchanged over a short period of time. This discontinuity occurred early enough in the sintering run where the relative density of the powder film was still below 60%. With a loosely packed structure and with interparticle necking in the early stages, the particles retain some mobility with room for particle

rearrangement such that yielding of the film is possible. Lu, et al. [5] calculated the stress in a gold film undergoing sintering using Skorokhod's model for the shear viscosity (G_p) and assumed that the maximum calculated stress will be the yield stress of the gold at the sintering temperature of around 10 MPa. However, this value is much higher than what has been experimentally observed in the same material[4]. The possibility of yielding at lower stresses due to the loose packing was not considered. The duration of the yielding stage varied with the sintering temperature. At 950°C, this occurred between 25 and 33 minutes, right after the start of the isothermal regime, while at 1000°C, it was between 25 and 35 minutes. The discontinuity is less obvious at 1050°C, with a drop in stress between 31 and 33 minutes. The speed of the densification at the higher temperature kept the duration very short and difficult to notice.

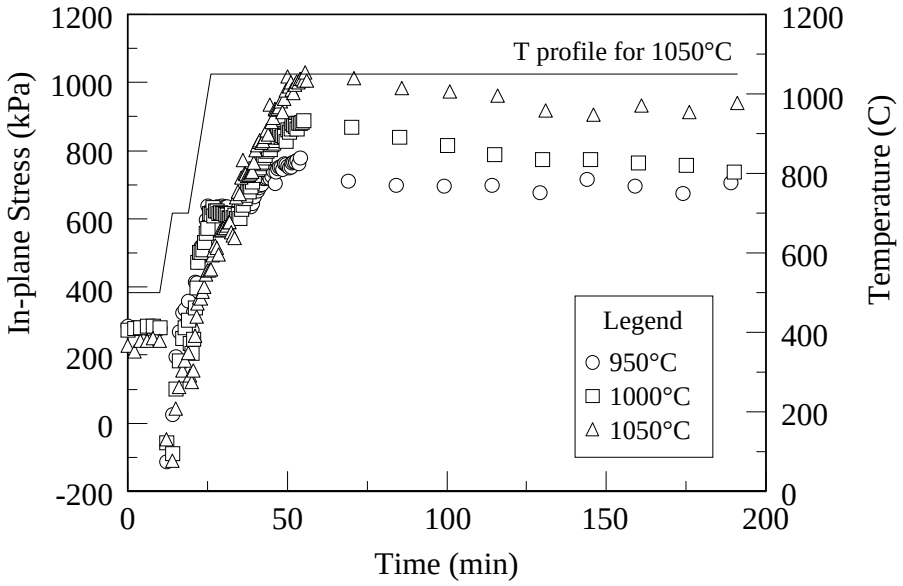

Figure 4.24. In-plane stresses in the constrained ZnO films on silicon substrate at various temperatures.

Turning to the expanded plot in Figure 4.26, a barely noticeable dip can be seen between 19 and 20 minutes for all curves and correspond to the resumption in the temperature ramp-up. At this stage, the density barely increased over the initial density, such that this too can be attributed to a temporary temperature gradient across the sample thickness. After the yielding event, the stress continues to increase gradually tapering off and reaching a maximum when the shrinkage rate has dropped of significantly.

Afterwards, the stress gradually drops, reminiscent of a viscoelastic body undergoing relaxation. However, unlike constrained glass films [53], there is a substantial stress remaining even after a lengthy period, highlighting the difference between glass and crystalline materials. While viscous flow quickly dissipates the stress in glass, the stress in a crystalline body will have to be relieved by slower diffusion processes.

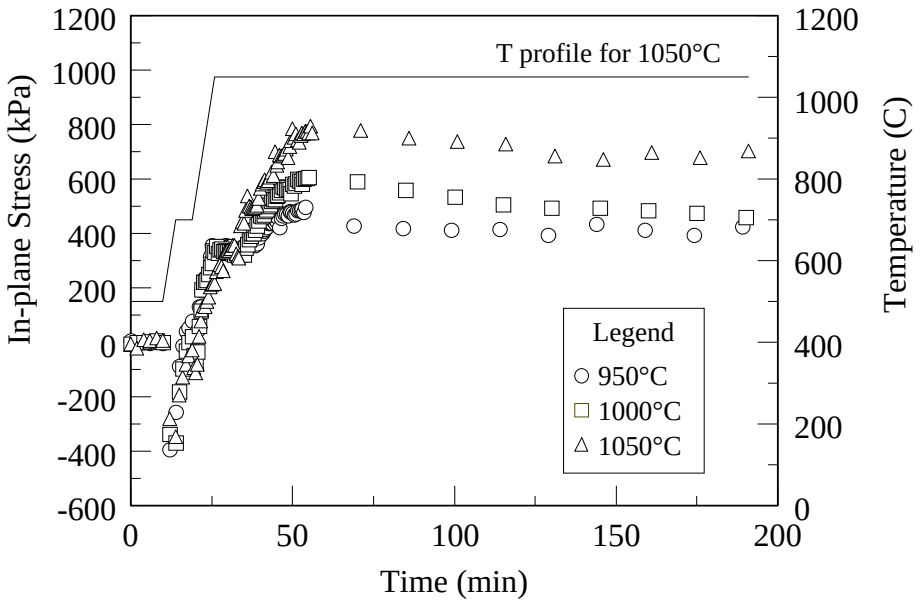

Figure 4.25. In-plane stresses in the constrained ZnO films on silicon substrate at various temperatures with the initial stress offset to zero.

The stress curves in Figure 4.25 are replotted against relative density in Figure 4.27. Instead of the short yielding stage observed in the stress versus time plots, the stress for each temperature did not appreciably change over a wider range of densities. The stress did not increase again until it reached a threshold density that also increased with sintering temperature. This could be due to the increased ability of the particles to consolidate further before widespread necking takes place.

There is also a question of the level of stresses experimentally observed when compared to predicted stresses. Measurements on gold films, also a crystalline material, showed stresses reaching hundreds of kilopascals but not exceeding 1 MPa before dropping[4]. Scherer and Garino[49] predicted maximum stresses for some materials

undergoing viscous sintering. For an alkoxide-derived silicate gel, a stress of up to 35 MPa was predicted and, for a colloidal gel, up to 4.4 MPa.

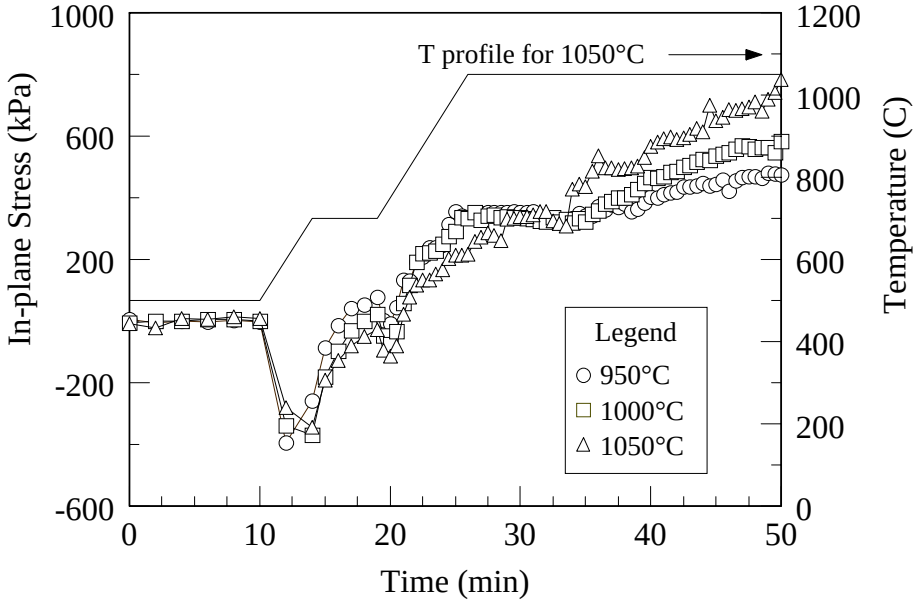

Figure 4.26. In-plane stress versus time (offset to zero) expanded to show the details of the early stage of the sintering.

Looking at Figure 4.28, there is practically a linear increase in the stress for all temperatures after the yielding stage and before there is considerable slowdown in the densification rate (see Figure 4.22). At 950°C, the stress increases at a rate of 46 kPa per percent increase in relative density. At 1000°C, it increases at 80 kPa per percent, and at 1050°C, by 86 to 87 kPa per percent increase in relative density. The substantially lower rate at 950°C could be because the relative density is still below 60 percent, such that the particles have room to adjust and the joint between particles may not be as extensive compared to the higher temperatures. Even assuming that the rate of stress increase is sustained to around 90 percent density, the maximum stress will only be around 3 MPa, which is still lower than the predicted figures above. This may even be an optimistic figure, considering that the stress actually starts to decline when the densification rate drops significantly.

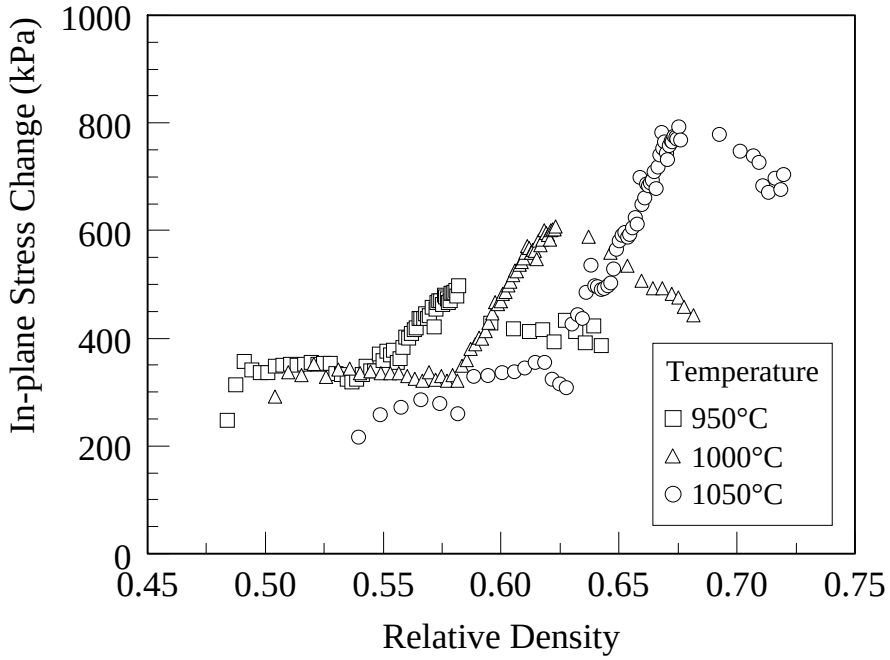

Figure 4.27. Isothermal portion of the in-plane stress versus relative density.

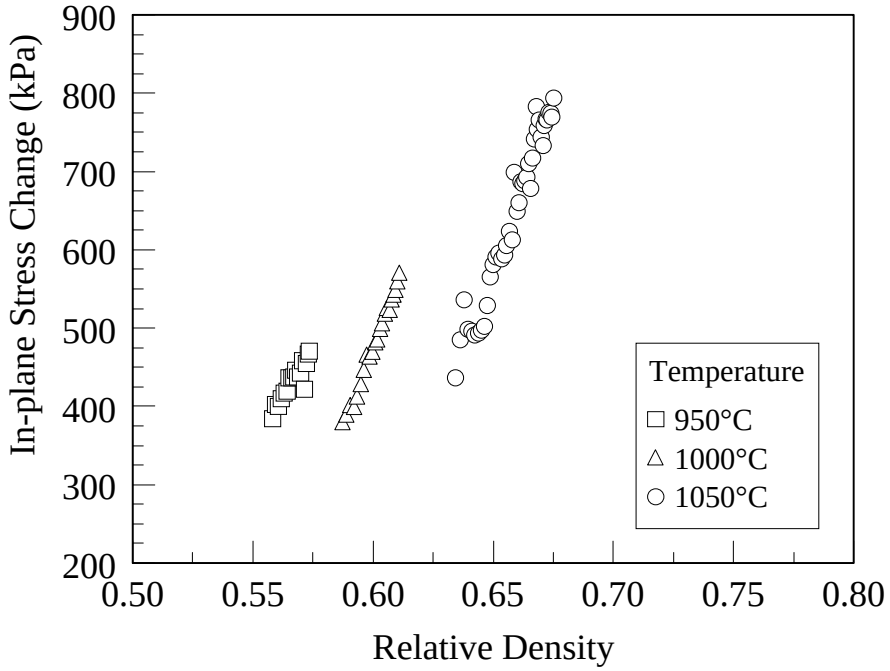

Figure 4.28. In-plane stresses plotted against relative density after the yielding stage and before gradual relaxation of the stress.

4.3 Summary

Densification experiments on freestanding and constrained films of ZnO powder showed that substrate constraint substantially reduced the densification rates and the density that can be attained. Although both types of samples contained a lot of porosity, the sintered microstructures were different. The freestanding films contained grains that had a more regular equiaxed structure with grains connected to each other over a wide area of the grain boundaries. The constrained film had a microstructure consisting of grains connected by narrow necks because the substrate prevented the particles from moving closer to develop the thicker contacts found in the freestanding films. The result is a wide-open skeletal structure. The activation energies for densification were also different. The freestanding film had an activation energy of 242 ± 21 kJ/mole while that of the constrained film was 391 ± 34 kJ/mole. The sizable difference in activation energies indicates that, in the freestanding film, other mechanisms may be operating such as grain boundary diffusion and some mechanical rearrangement while the dominant mechanism is by lattice diffusion in the constrained film. In-plane stresses were observed to develop during sintering of constrained films through the formation of a camber or curvature on the substrate. Yielding of the constrained film appears to have taken place at densities below 60% when the interparticle necks have not widened enough and where some particle rearrangement is still possible. After the yielding event, the stress increased linearly with density and then gradually declined after the densification rate has tapered off.

Chapter 5
Constrained Sintering of Crystallizable Glass

The free and constrained densification curves were obtained using glass powder with an average particle size of 10 μm. Silicon was used as the rigid non-sintering substrate. Other substrates were also used, including aluminum nitride (AlN) with a CTE close to the crystallized glass, to try to explain the observed deviation from shrinkage of the constrained films. A powder with smaller average particle size (3.97 μm) was subsequently used to obtain densification curves below 900°C for calculating the activation energy of densification.

5.1 Results

The shrinkage profiles at 900, 950 and 1000°C of cordierite-base crystallizable glass (glass-ceramic) constrained on silicon substrate are plotted in Figure 5.1. The corresponding densification curves are shown in Figure 5.2. The two sets of curves are mirror images of each other since the relative density is inversely proportional to the film thickness. The constrained film had an initial relative density of 0.58 ± 0.02. The graphs show that the glass film undergoes shrinkage before expanding. At 900°C, the film shrinks to nearly 60% of its initial thickness, corresponding to greater than 90% density, before undergoing an expansion that appears unfinished at the end of the isothermal sintering period. At 950°C, the shrinkage is faster, getting barely into the isothermal sintering regime before reversing and undergoing a more rapid expansion. The film shrinks to less than 70% of the initial thickness (around 85% relative density), and then expands back to more than 80% of the original thickness, or an apparent relative density of 72%. At 1000°C, the shrinkage is even faster than the previous temperature shrinking

to under 70% of the original thickness before expanding quickly to nearly 80% of the original thickness.

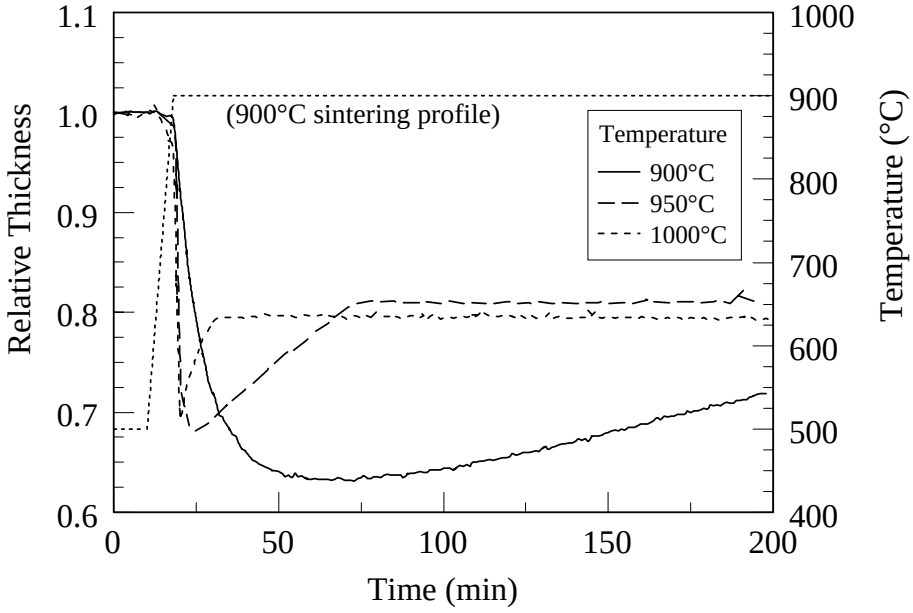

Figure 5.1. Shrinkage profile of cordierite-base crystallizable glass constrained on silicon substrate during sintering at various temperatures.

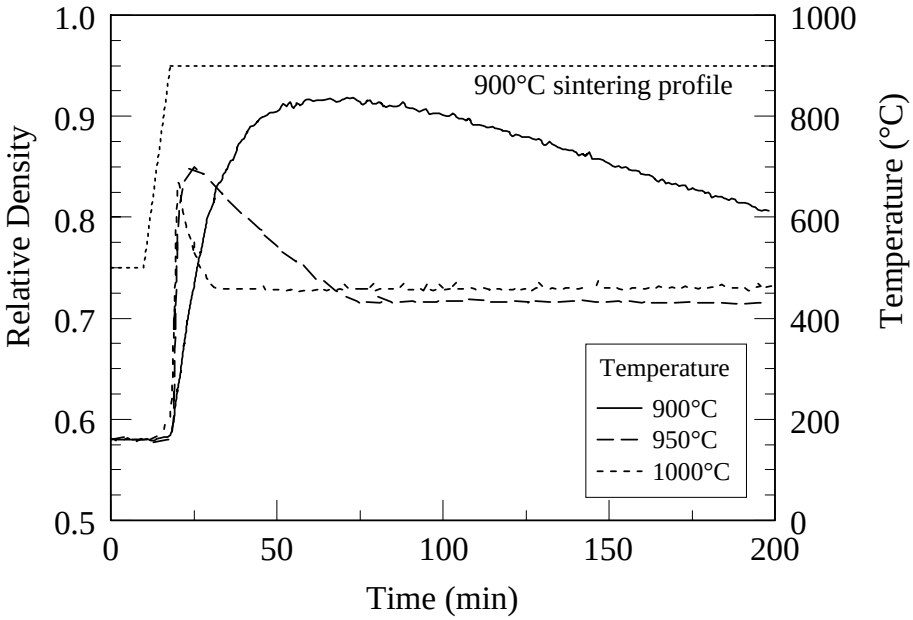

Figure 5.2. Densification curves for the crystallizable glass constrained on silicon during sintering at different temperatures.

The densification curves of the freestanding films are shown in Figure 5.3. Unlike the constrained films, the freestanding samples underwent rapid densification but without the expansion that followed the shrinkage in the constrained films. The density at 1000°C appeared to have overshot the maximum possible density but this is the result of the sample losing the sharpness of its rectangular corners as it minimizes its surface area and partly to some other shape distortion. The result is a more rounded edge and a thicker center, making the width even narrower and, at the same time, more difficult to detect. However, there is little doubt that the film has attained a density near 100%.

A combined plot of the densification curves of both types of samples at 900 and 950°C in Figure 5.4 show that the corresponding curves practically overlap each other before deviating due to the expansion of the constrained films. This is an indication that, at least in the early stage when the densification rate is at its highest, the densification is not outwardly affected by the substrate constraint. This observation was also made by Bang[71] during the sintering of pure borosilicate glass films above the softening point. The two curves deviated but not before attaining densities above 90% when the curve for the constrained film tapered off. Other than this deviation, the only other difference is in the microstructure where the constrained film contained larger residual pores compared to those in the freestanding film. The observation that the densification curves of the constrained film followed that of the freestanding film before film expansion also provides an indication of the absence of a crystalline phase that should affect the densification process. This will be discussed further later.

Aluminum nitride was substituted as the constraining substrate for the glass film to find out if the expansion is related to the substrate composition. The shrinkage and densification profiles are shown in Figure 5.5 and Figure 5.6, respectively. The films also underwent rapid shrinkage but the subsequent expansion was less severe for both temperatures than the ones observed in films constrained on silicon. The expansion also appeared to have stopped or slowed down to a barely noticeable rate two hours into the isothermal sintering at 900°C paralleling that of 950°C, which flattened out earlier. Other than that, the curves are similar to those obtained from films on silicon substrate such that the densification appeared to be independent of the substrate type.

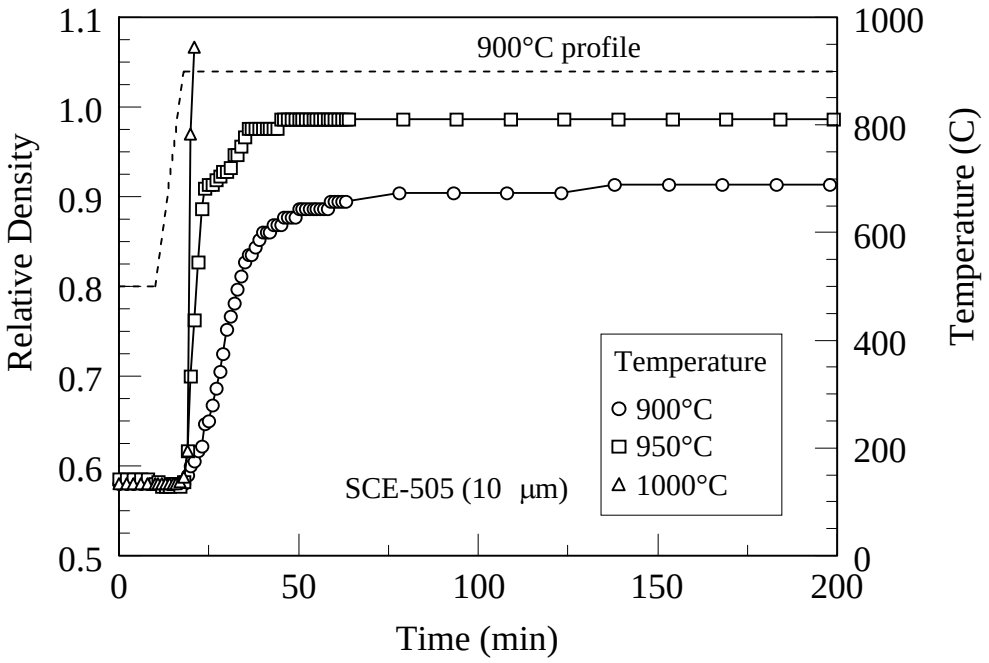

Figure 5.3. Densification curves of freestanding crystallizable glass films at various sintering temperatures.

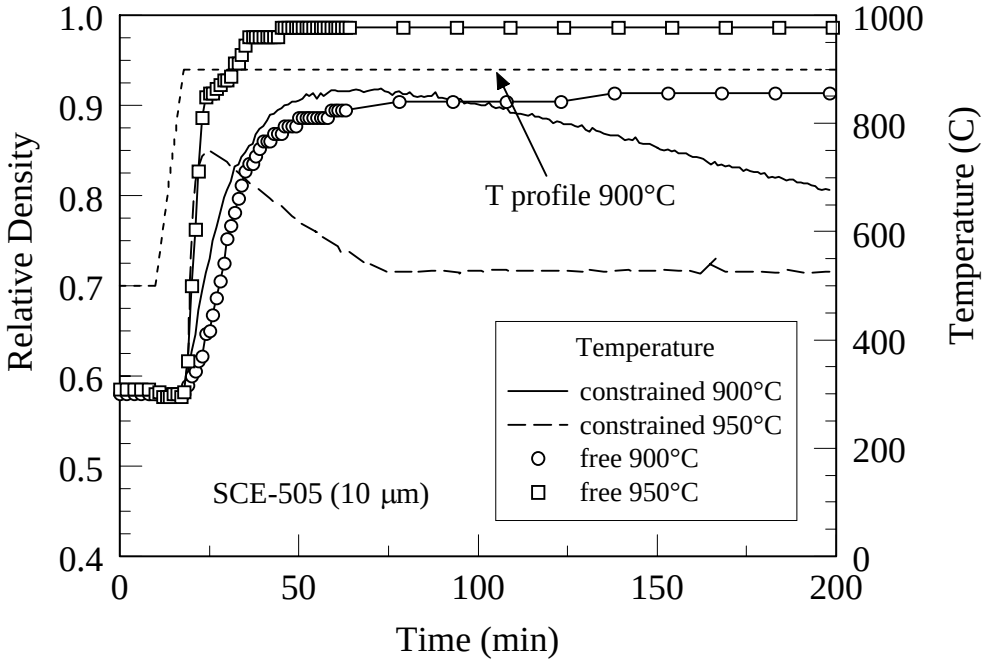

Figure 5.4. Combined plots of the densification profiles of freestanding and constrained crystallizable glass films sintered at 900°C and 950°C.

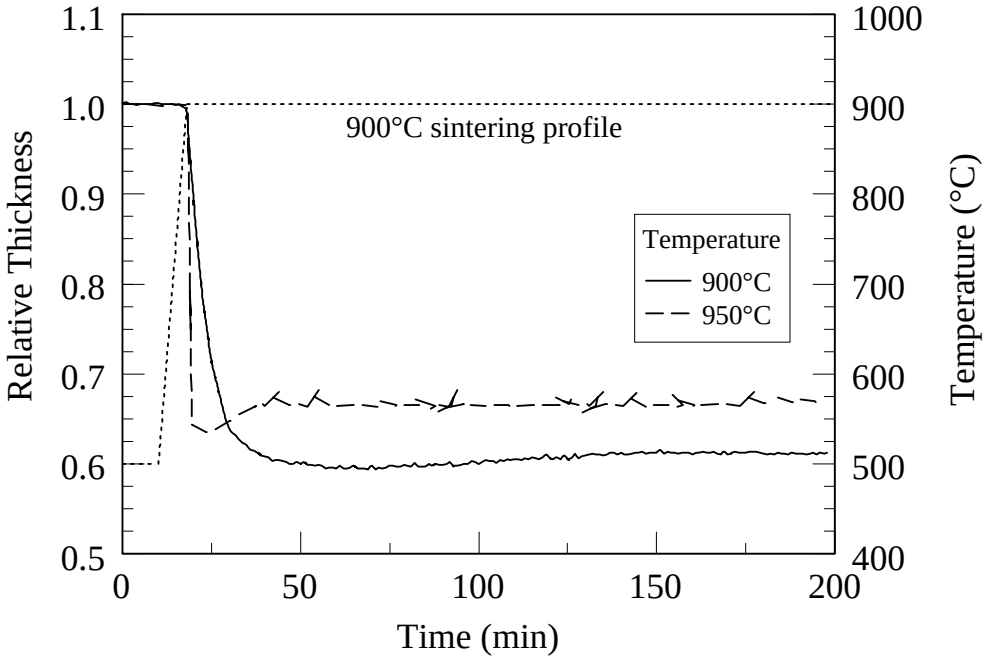

Figure 5.5. Shrinkage profiles of crystallizable glass films constrained on aluminum nitride.

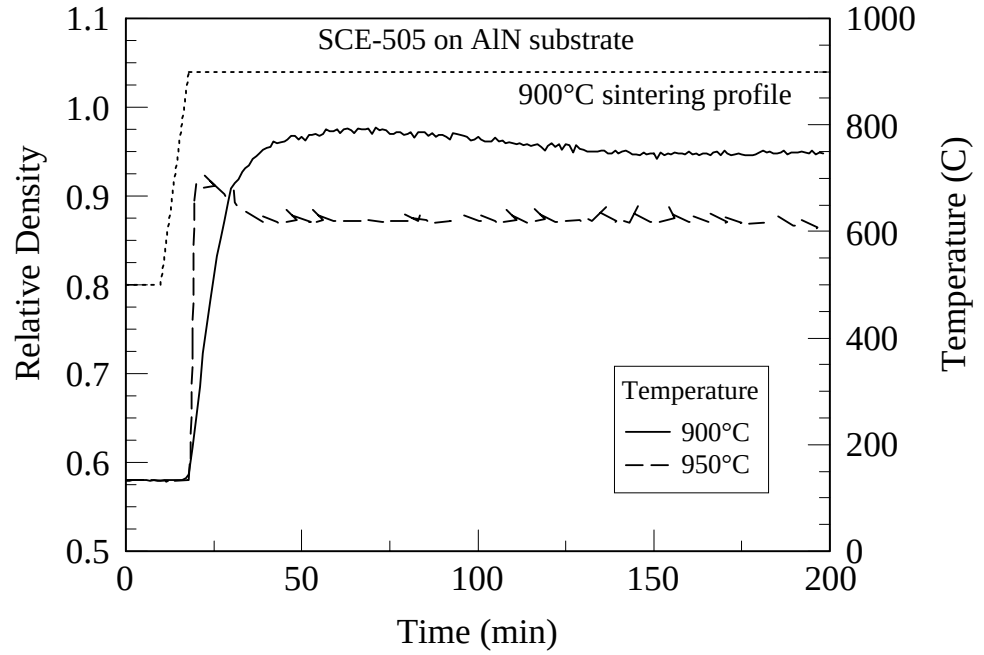

Figure 5.6. Densification profiles of crystallizable glass films constrained on aluminum nitride substrate.

The constrained films were fractured after sintering to determine how the films would look like and find out where the expansion is coming from. The SEM image in Figure 5.7 is the fracture surface of a film on silicon that was fired at 950°C for 3 hours. It reveals the presence of large pores in the glass-ceramic layer adjacent to the substrate. These pores are larger than the initial average powder size of 10 μm and are so numerous that they intersect each other. In the rest of the film, the pores are much smaller and sparsely distributed such that, without the large pores, the film has nearly attained full density. Since the presence of large pores was not observed in the unfired coatings, it is reasonable to conclude at this point that they were responsible for the film expansion. A film on aluminum nitride that was fired under the same condition (Figure 5.8) revealed the presence of some large pores but not as numerous as the pores in the film fired on silicon. Thus, this could explain why the observed expansion is smaller. In addition to the formation of the large pores, of further interest is why the pores did not shrink even after a prolonged sintering time. This will be tackled in the subsequent discussions.

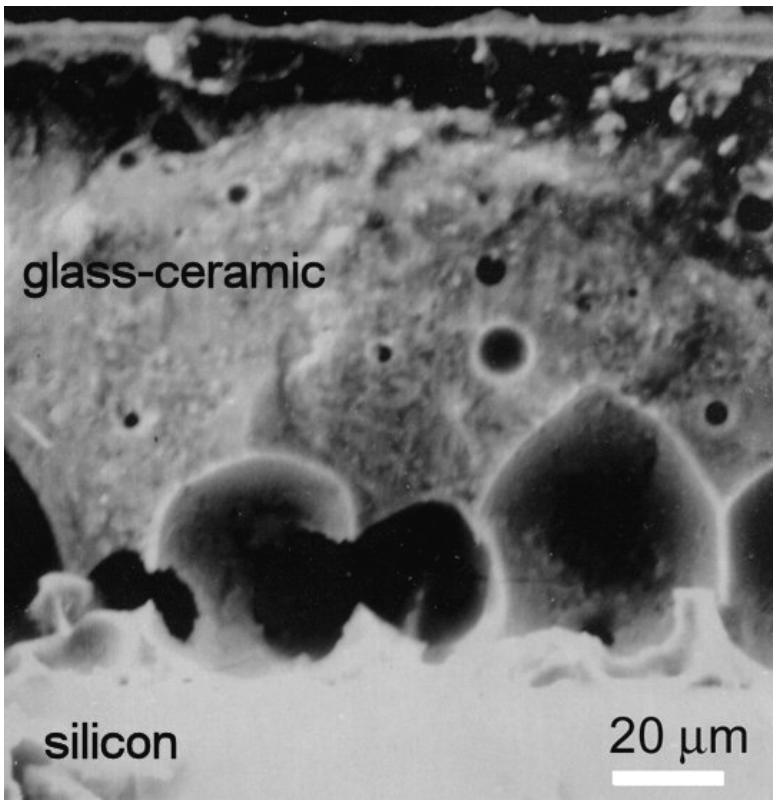

Figure 5.7. SEM micrograph of the fracture surface of the cordierite glass-ceramic constrained on silicon after sintering for 3 hours at 950°C.

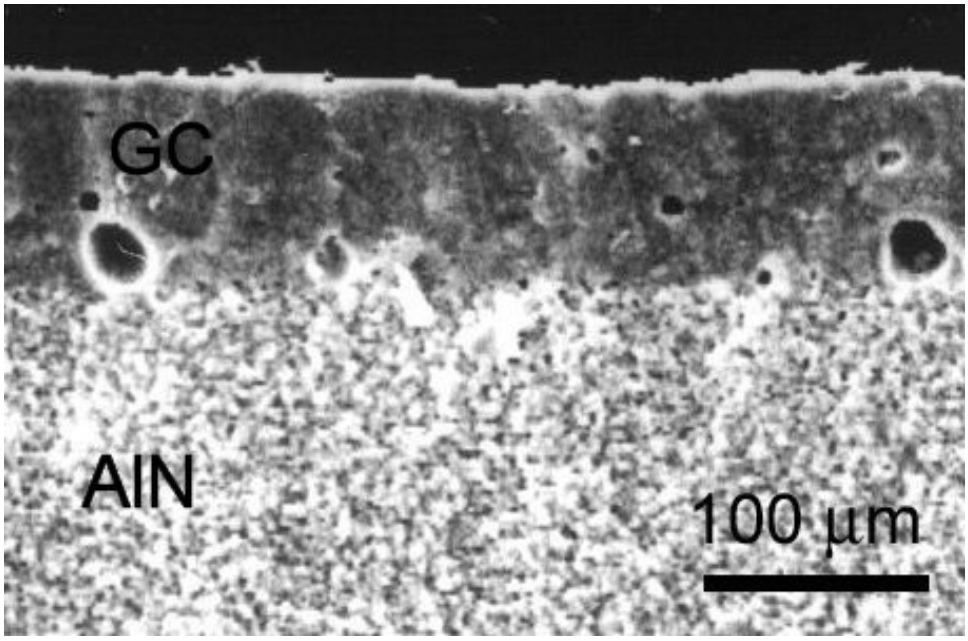

Figure 5.8. SEM micrograph of the fracture surface of the cordierite glass-ceramic (GC) constrained on AlN after sintering for 3 hours at 950°C.

5.2 Discussion

There are several issues that arose from the results in the previous section. Foremost would be the film expansion after the glass went through shrinkage and densification and why it happened. As mentioned previously, of further interest is why, even after prolonged sintering, the pores did not eventually disappear or shrink. Another issue is whether crystallization of the glass affected the densification of the film and played a role in the persistence of the pores. There is also the question of the levels of stresses that may have occurred in the film during sintering and how they relate to the microstructure evolution. Since the densification curves of the constrained films were comparable to those of the freestanding films, it is almost a foregone conclusion that the densification mechanism would not change, that is by viscous flow. Nevertheless, the activation energy for densification was obtained to find out if there were other effects that could alter the calculated value.

Densification Rates and Activation Energy of Densification

Because the shrinkage rates at the higher sintering temperatures were too fast such that the films already attained very high density before reaching the isothermal condition, glass powder with a smaller average particle size of 3.97 μm was used in order that sintering with substantial shrinkage can be obtained below 900°C but at a slower rate. The glass films had an initial relative density of 0.49 ± 0.2. The densification profiles for temperatures of 875, 900 and 950°C are plotted in Figure 5.9. The films sintered at 900 and 950°C underwent expansion but not the film sintered at 875°C. The calculated densification rates are shown in Figure 5.10 and Figure 5.11 with the rate at 950°C being much higher than at the other two temperatures. However, if the densification process is thermally activated, the densification rate at 950°C when plotted versus relative density seems to be underestimated. This is important because the activation energy of densification is calculated from the densification rates as was done in the sintering of zinc oxide.

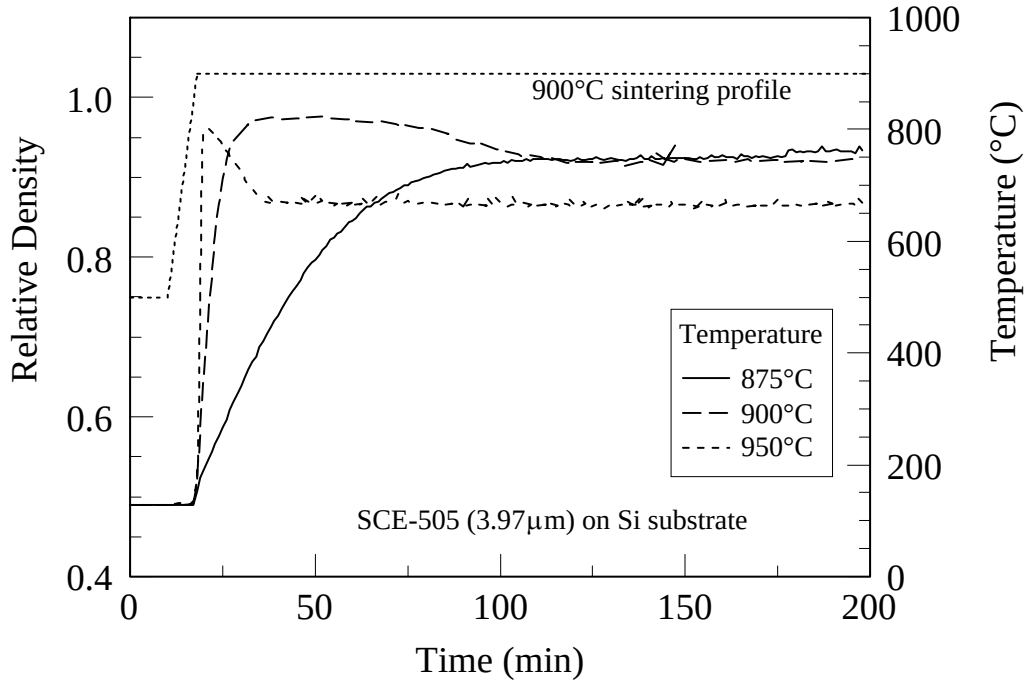

Figure 5.9. Densification profiles of constrained films from the 3.97mm glass powder.

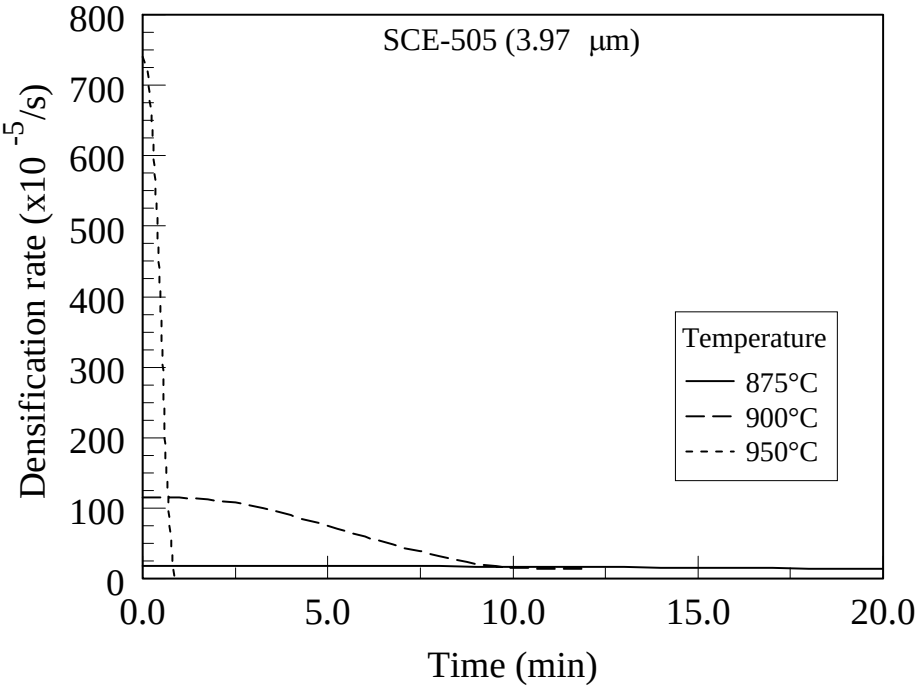

Figure 5.10. Densification rates of crystallizable glass films constrained on silicon.

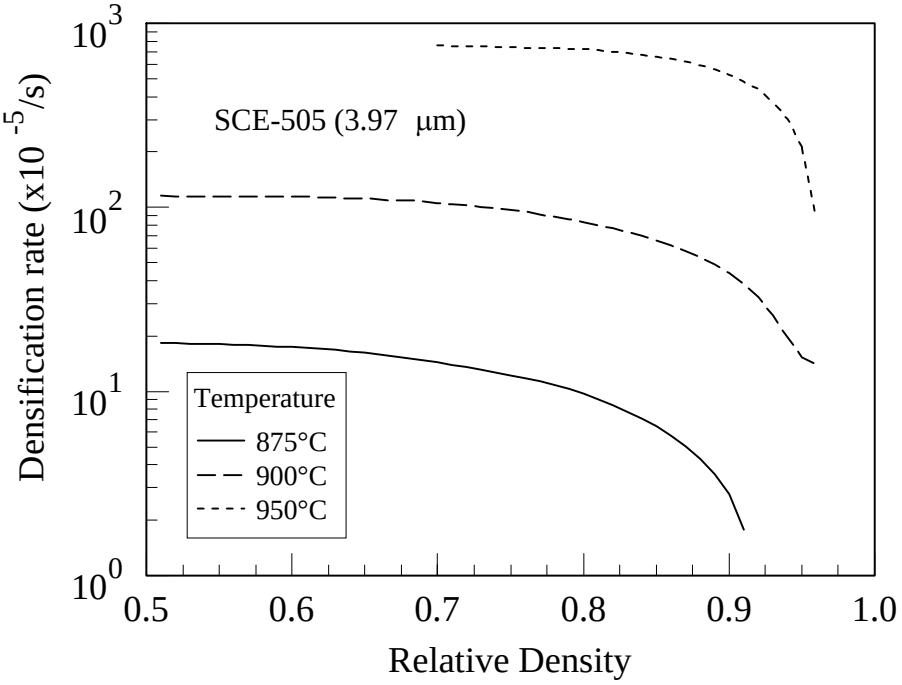

Figure 5.11. Densification rates of crystallizable glass films constrained on silicon as a function of relative density.

The activation energy was obtained using a similar procedure from the previous chapter. The difference is that the glass-ceramic, while still in amorphous form, densifies by viscous flow such that a different relationship between the densification rate and activation energy is needed. A generalized equation of the densification rate ($\dot{\bar{\rho}}$) developed by Scherer[34] is used to calculate the activation energy and is of the form

$$\dot{\bar{\rho}} = DF \times KF \tag{5.1}$$

where *DF* is the driving force that is dependent on the surface tension, initial pore size of the porous body and a geometrical factor, *KF* is the kinetic factor containing the viscosity term, η, in an inverse relation. The viscosity is expressed in terms of the activation energy *Q*, and temperature *T* (in Kelvin) in the following equation

$$\eta = \eta_o \exp\left(\frac{Q}{RT}\right) \tag{5.2}$$

where *R* is the gas constant and η_o is the pre-exponential factor. Therefore, it follows that the densification rate is proportional to the exponential of the activation energy. Using an Arrhenius plot of densification rate versus 1/T at a fixed density, the activation energy of densification can be obtained from the slope. If the glass remains in the amorphous state at that particular density, it should be the same or similar to the activation energy obtained from Eq. (5.2)

The densification rates at several densities are plotted on a logarithmic scale against 1/T in Figure 5.12. The data for 950°C seem to be depressed relative to the other temperatures on the plot such the activation energy for densification from the linear fit would fall between 600 and 800 kJ/mole. The activation energy of the glass-ceramic can be calculated from the annealing point of 757°C and softening point of 870°C. The viscosities at these temperature points are defined by convention to be 10^{13} poise (10^{12} Pa-s) and $10^{7.6}$ poise ($10^{6.6}$ Pa-s)[72]. Using Eq. (5.2), an activation energy of 1077 kJ/mole is obtained. This is higher than what was obtained from the linear fit, which was depressed by the data for 950°C. An inspection of the plot of activation energy with relative density in Figure 5.13 would also make one to conclude that the densification mechanism is changing with density. However, if the data for 950°C were excluded, the plotted results (Figure 5.14) for the other two temperatures form nearly parallel lines with

activation energies near that obtained from the calculations using the annealing point and softening point. The increasing value of Q with relative density may simply be an artifact of the method of obtaining the densification rates from the densification curve, pore formation and growth concurrent with densification that suppresses the densification rate, and the low densification rates at the higher densities, all of which could introduce additional uncertainties. The possibility that it could be the effect of crystallization is also remote, since the timeframe covered is only a short segment of the total sintering time as the glass attained high densities very quickly.

Based on a Q of 1077 kJ/mole, the densification rate at 950°C can be calculated to obtain a new curve that would make the plots in Figure 5.12 conform to a linear fit. The calculated curve is plotted along with the experimental curves in Figure 5.15. Given the interval between the curves for 875° and 900°C, the gap between the curves for 900°C and 950°C should also be wider, which is roughly where the calculated curve should be. The activation energy does not explain the expansion of the film due to the formation of large pores but it does eliminate the densification mechanism among the possible reasons.

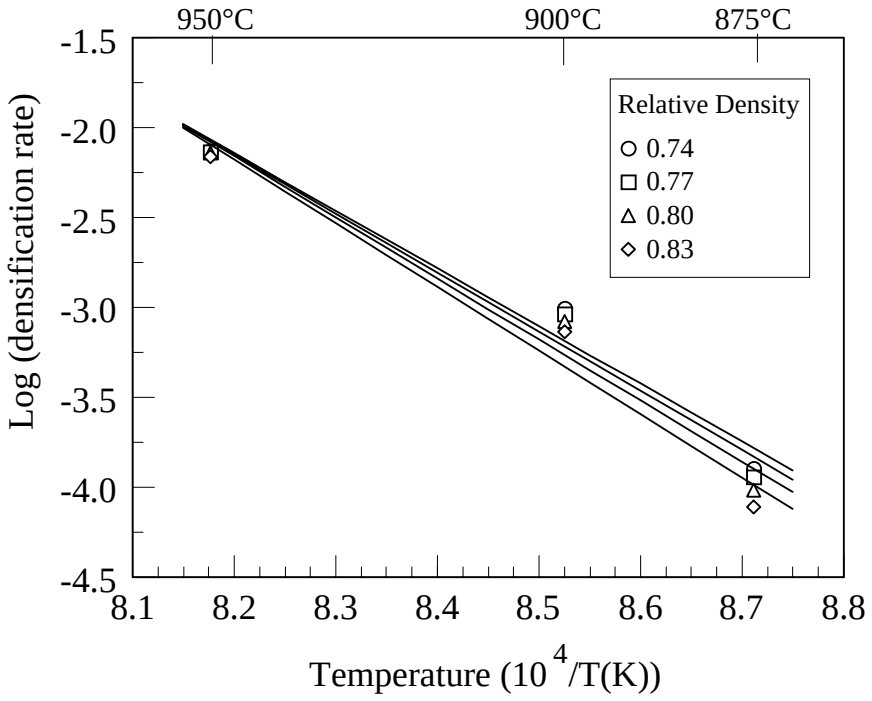

Figure 5.12. Plots of log densification rate versus 1/T at various relative densities for the constrained crystallizable glass films.

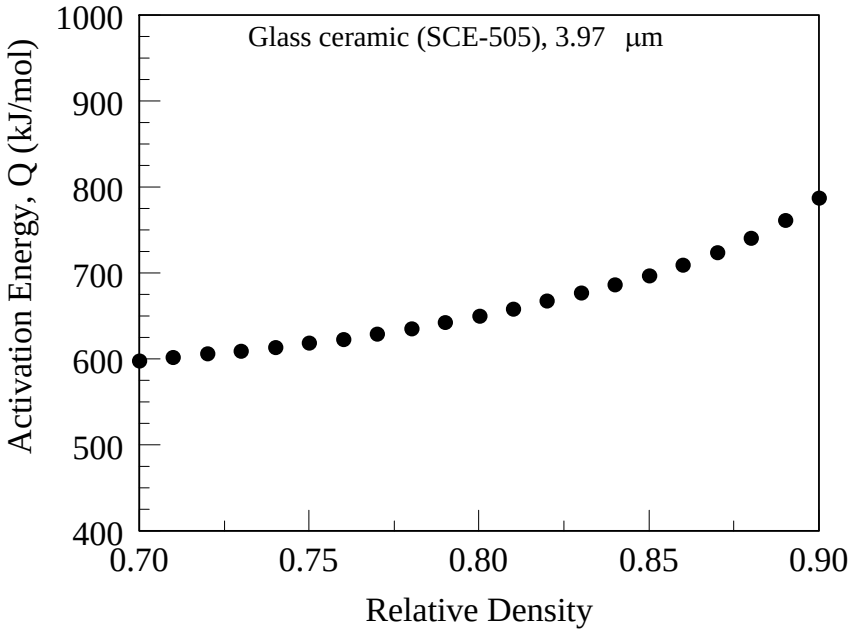

Figure 5.13. Calculated activation energy of densification versus relative density for the constrained crystallizable glass films.

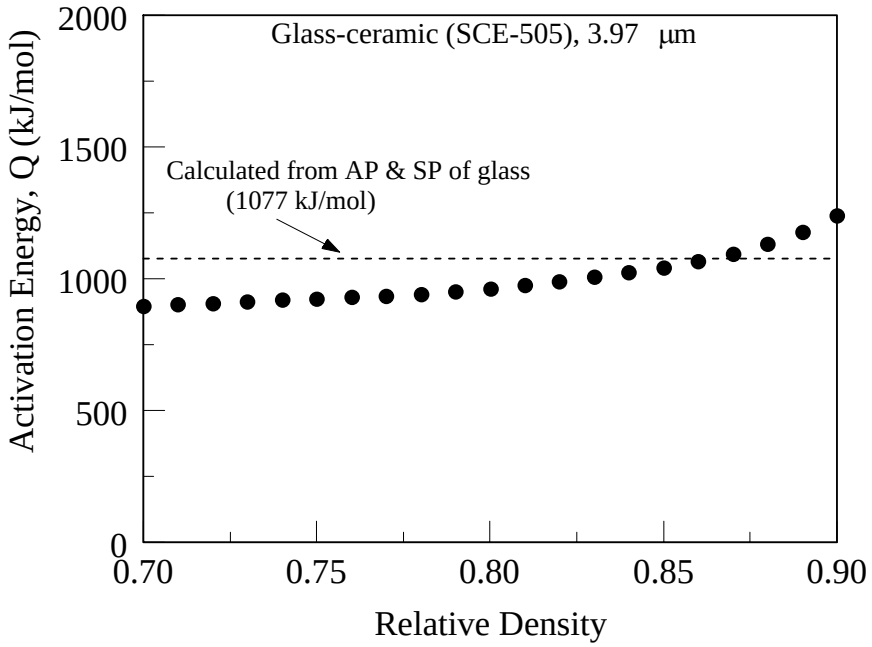

Figure 5.14. Calculated activation energy of densification for constrained crystallizable glass films by considering only data from 875°C and 900°C.

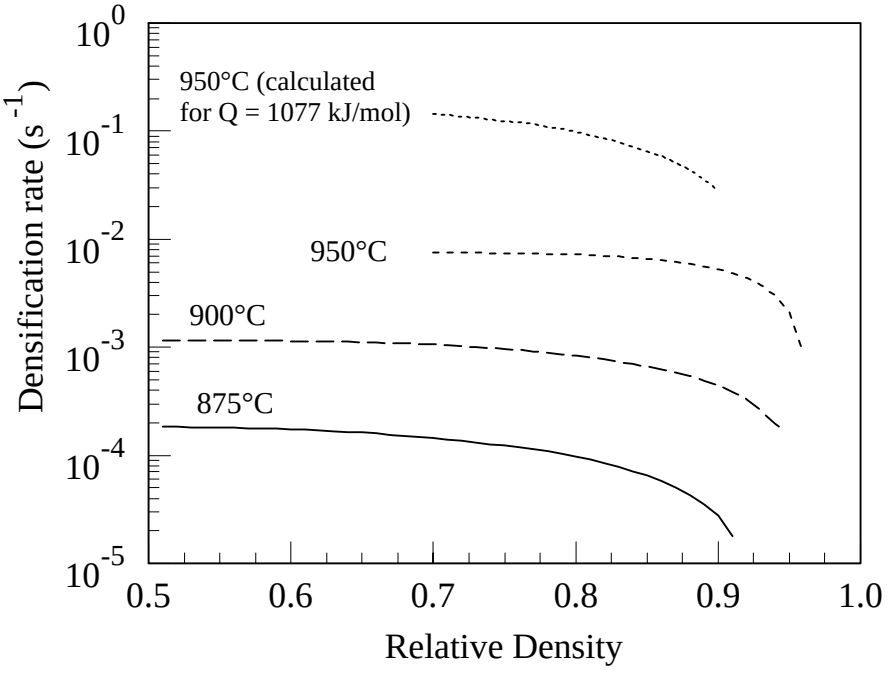

Figure 5.15. Densification rate of constrained 3.97 μm crystallizable glass film on silicon substrate. The densification rate at 950°C calculated for a Q of 1077 kJ/mole is also shown.

Film Expansion during Constrained Sintering

Understanding why the pores formed during sintering of the constrained film, particularly on silicon substrate at the higher sintering temperatures requires an observation of the sintered microstructure, the progress of the crystallization and the development of the in-plane stress, as well as the possibility of some reaction at the film-substrate interface. Each one will be examined and an explanation of the why the expansion occurred will be attempted. A solution to eliminate the problem will also be discussed.

Sintered Film Microstructure

Looking back at Figure 5.1and Figure 5.2, the curve for 900°C showed a gradual transition from shrinkage to expansion. The start of pore formation need not coincide with the start of the observed expansion since it could have been happening while

shrinkage was still in progress. The two micrographs in Figure 5.16 were from samples sintered up to 9 minutes and 42 minutes into the isothermal regime. The former is at a period in the sintering profile where the film is still undergoing relatively rapid shrinkage while the latter is at the peak of the shrinkage before it turns into an expansion. The film sintered for 9 minutes (Figure 5.16(a)) already show some porosity of varying sizes at the interface with the silicon even while the film was still shrinking. At 42 minutes (Figure 5.16(b)) when the shrinkage tops out, the pores at the interface have grown bigger. The two micrographs provide evidence that the pores have begun to form and grow even while the net trend is shrinkage. The early formation of pores can also depress the observed shrinkage of the film, and thus the densification rate. This could partly explain why the densification rate at 950°C was considerably lower than expected based on the calculated activation energy from the annealing and softening points of the glass. To some extent, this was also the case at 900°C. Thus, the activation energy obtained from the densification rates is also reduced.

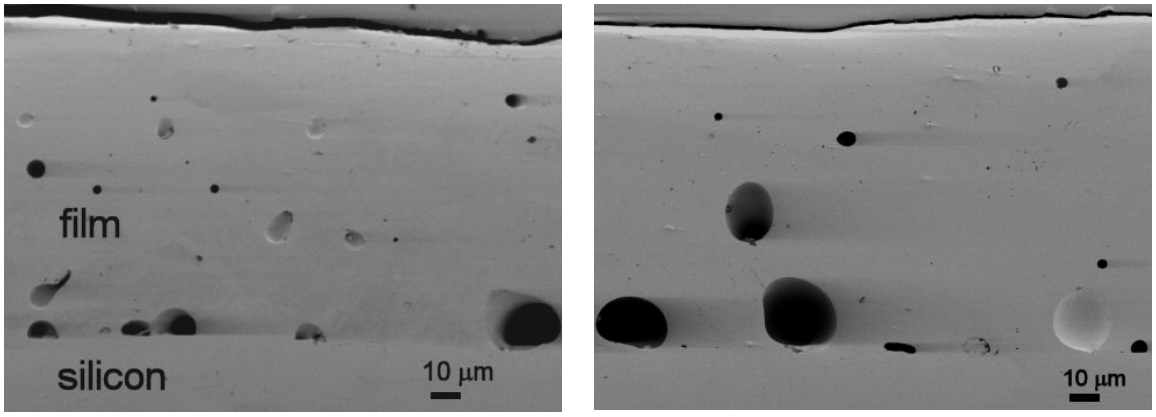

(a) (b)

Figure 5.16. SEM micrographs of the cross-sections of crystallizable glass films constrained on silicon after isothermal sintering at 900°C for (a) 9 min and (b) 42 min.

The series of micrographs in Figure 5.17 show the progress of pore formation and growth in the constrained film sintered at 950°C during the expansion period and up to the end of the sintering cycle. At 8 minutes, which is right after the peak average density was attained, pores are already visible with sizes up to around 20 μm and that indicates

that they formed earlier while the film is undergoing a net shrinkage. The pores experience further growth during the expansion regime as seen for times of 17 and 32 minutes into the isothermal regime. The final sintered microstructure at 3 hours of sintering is shown in Figure 5.17(d) where the pores have formed and grown to the point where they intersect each other. As the sintering progresses, the wetting of the substrate appears to deteriorate. Parallel to these events was an observed change in the optical characteristics of the film. The film starts out as a transparent coating on the substrate, gradually becoming translucent and eventually becoming a white opaque film for coatings fired at 950 and 1000°C. At 900°C or lower, the film appeared translucent. The question now is whether the change is due to the crystallization of the glass or the formation and growth of the pores. The progressive loss of wetting could either come from a reaction with the substrate and/or a change in the composition of the glass due to transformation into the crystalline cordierite phase. For the latter reason, transformation should be widespread at both 900 and 950°C. It should be possible to confirm the transformation by the x-ray diffraction results, which will be shown later.

SEM micrographs of a sintered film constrained on aluminum nitride (AlN) substrate (Figure 5.18) show the presence of pores at the interface but not as widespread as in films constrained on silicon substrate. Still, AlN is not very reactive such that wetting by the glass is relatively poor and adhesion weaker too. The film shown in the micrographs is one of the better samples observed. On the other hand, when the film is constrained on alumina (Al_2O_3) substrate, the pores did not form at all. This can be seen in Figure 5.19, where even at high magnification, the interface between the sintered glass-ceramic film and the substrate is very clean and almost devoid of any porosity. Any porosity that persisted after sintering is most likely due to a defect in the green coating and not generated by sintering. Since Al_2O_3 is a major component of the glass, it is reasonable to expect that the glass would wet and adhere strongly to the substrate. The difference in the interface microstructure between films on AlN and Al_2O_3 substrates provides a strong indication of the role of the surface layer of the substrate directly in contact with the coating, not necessarily the bulk of the substrate.

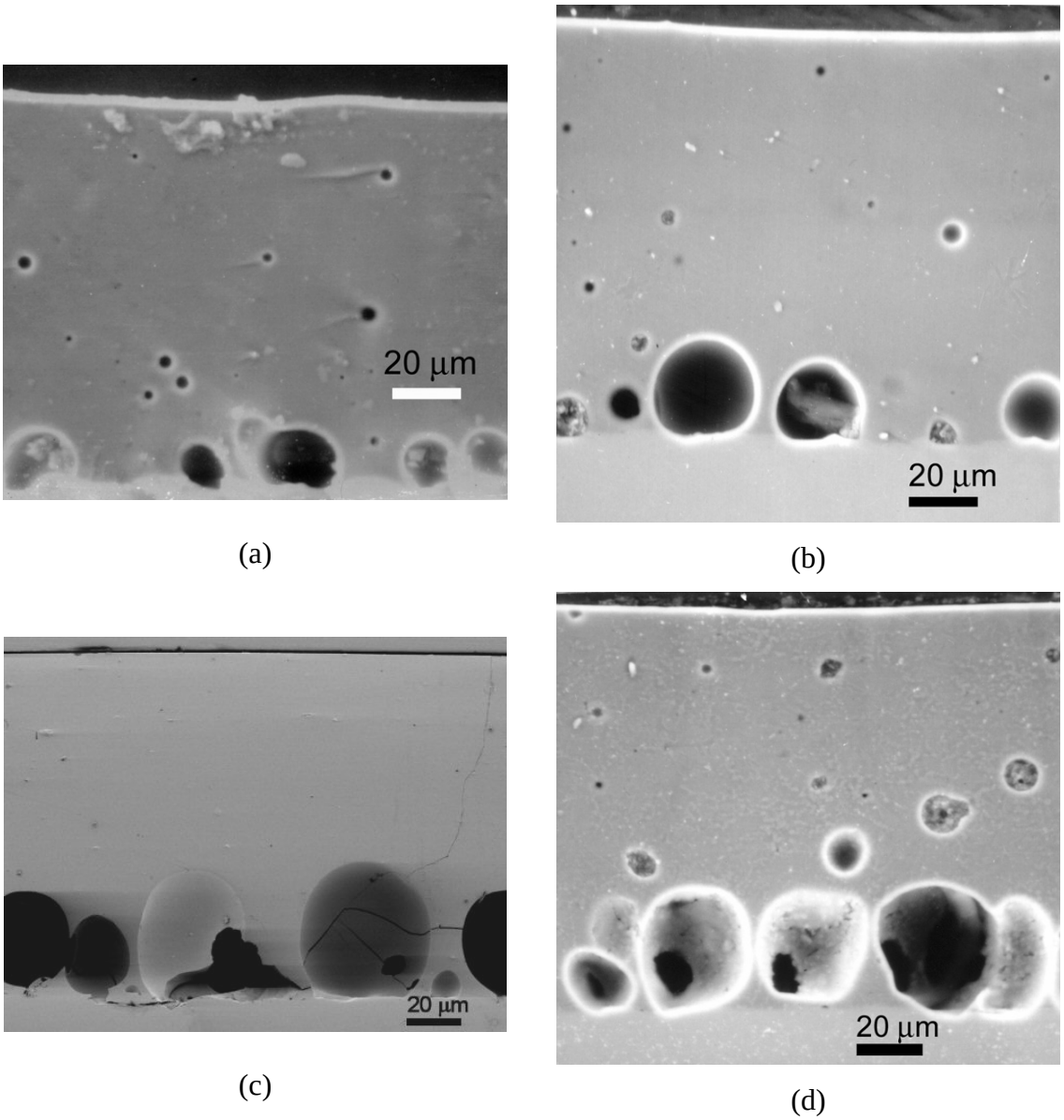

(a) (b)

(c) (d)

Figure 5.17. SEM micrographs of the cross-sections of crystallizable glass films constrained on silicon sintered at 950°C for (a) 8 min, (b) 17 min, (c) 32 min, and (d) 3 hr.

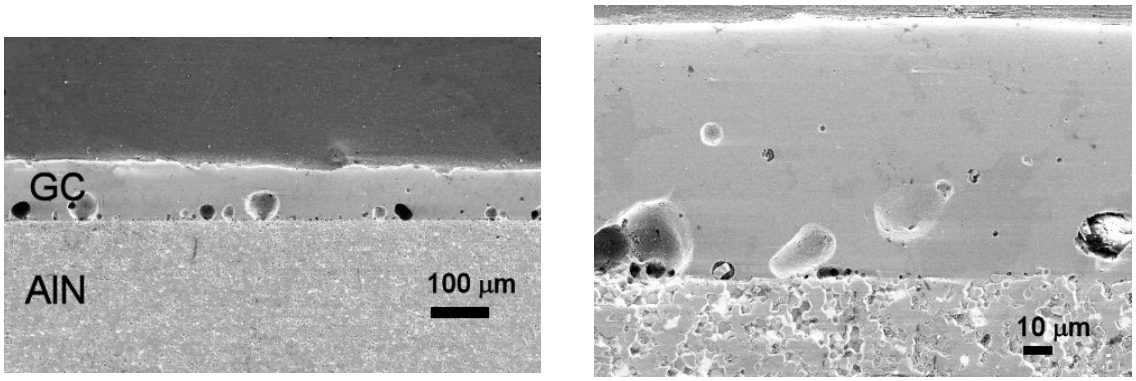

(a) (b)

Figure 5.18. SEM micrographs of crystallizable glass (GC) constrained on AlN substrate sintered at 950°C for 3 hours at magnifications of (a) 100X and (b) 500X.

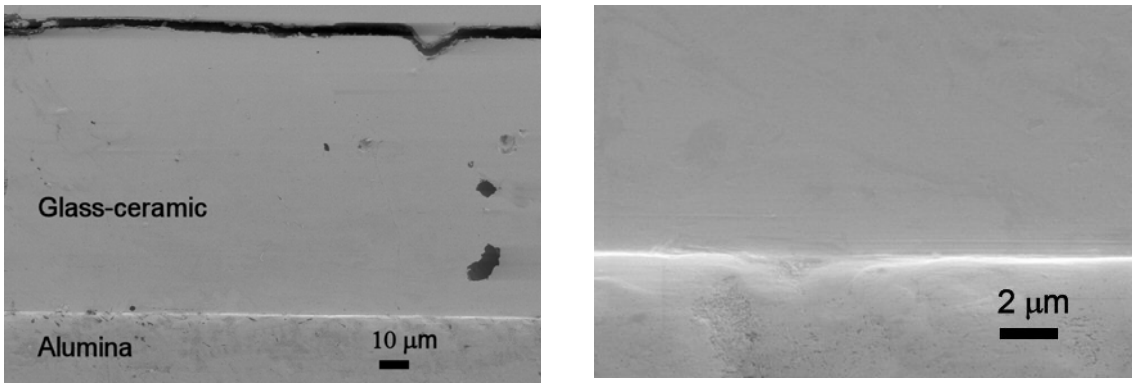

(a) (b)

Figure 5.19. SEM micrographs of crystallizable glass constrained on Al_2O_3 substrate sintered at 950°C for 3 hours at magnifications of (a) 500X and (b) 5000X.

X-ray Diffraction of Sintered Films

X-ray diffraction patterns were obtained for films sintered at different temperatures. The results for films sintered for 3 hours are plotted in Figure 5.20. Only films that were sintered above 900°C showed strong cordierite peaks suggesting that the film sintered at 900°C (and lower) did not undergo significant crystallization. Since constrained films sintered at 900°C also underwent expansion, although at a more gradual pace, the XRD measurements indicate that pore formation is not the result of transformation of the glass, such as crystallization. Films were also sintered at 950°C under different durations. X-ray diffraction patterns are plotted in Figure 5.21 for

sintering times of 8 minutes to 3 hours corresponding to the microstructures in Figure 5.17. Peaks did not start appearing until after 32 minutes into the isothermal stage, again showing that crystallization did not play a primary role in the evolution of the pores at the interface. Related to the appearance of the diffraction peaks is the evolution of the fracture surface (Figure 5.22(a)-(c)). At 8 minutes (Figure 5.22(a)), the break is relatively clean and flat typical of a glassy material. At 17 minutes (Figure 5.22(b)), the fracture surface starts acquiring some striations and texturing. Finally, at 3 hours, the fracture resembles more of a crystalline material fracture coinciding with the very strong peaks in the XRD pattern.

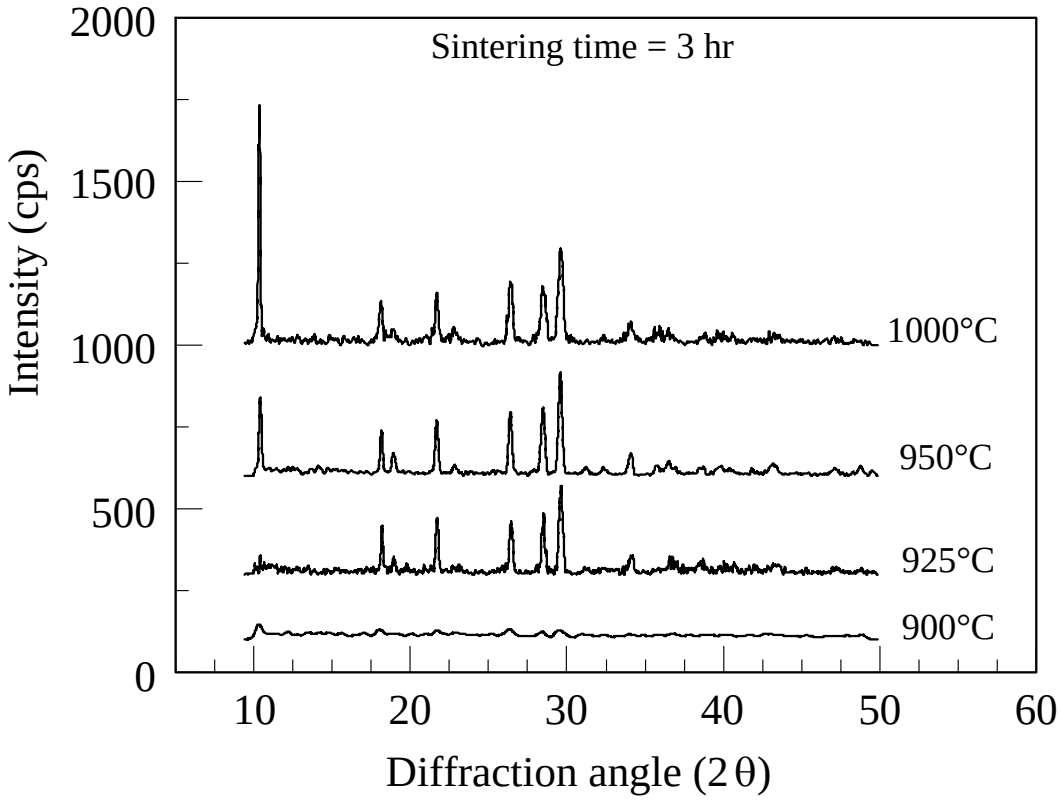

Figure 5.20. X-ray diffraction patterns from crystallizable glass films sintered for 3 hours at several temperatures.

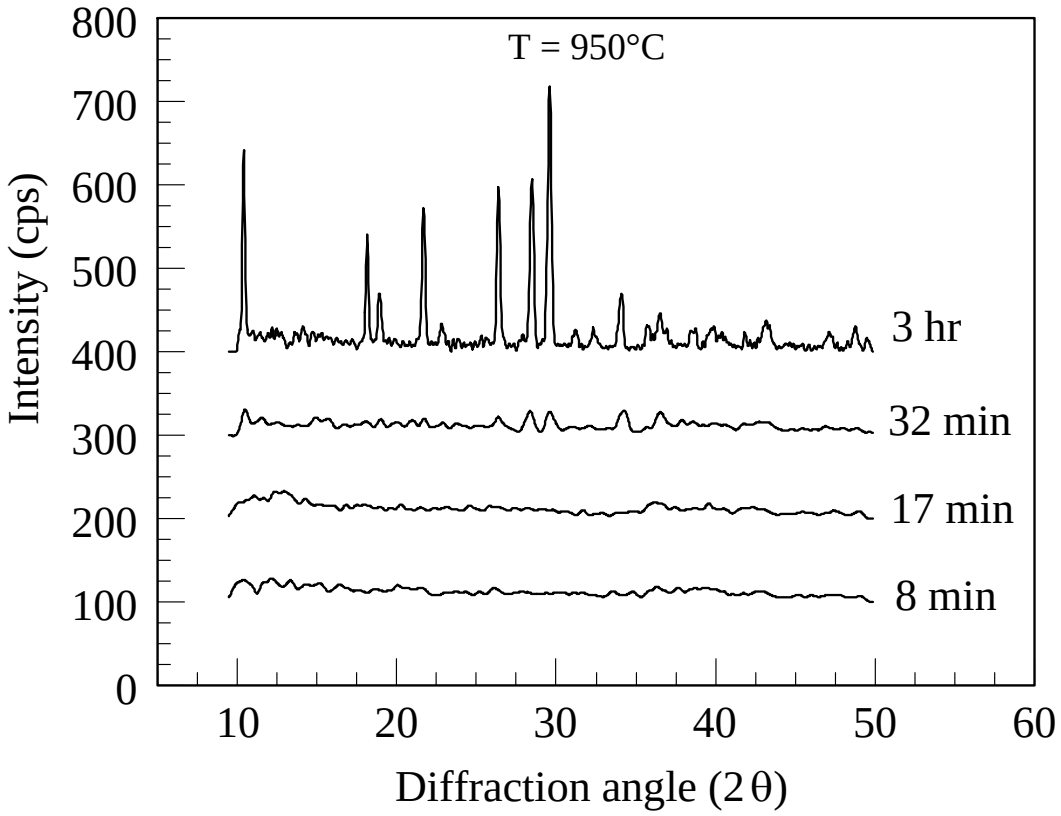

Figure 5.21. X-ray diffraction patterns from crystallizable glass films sintered at 950°C for different sintering times.

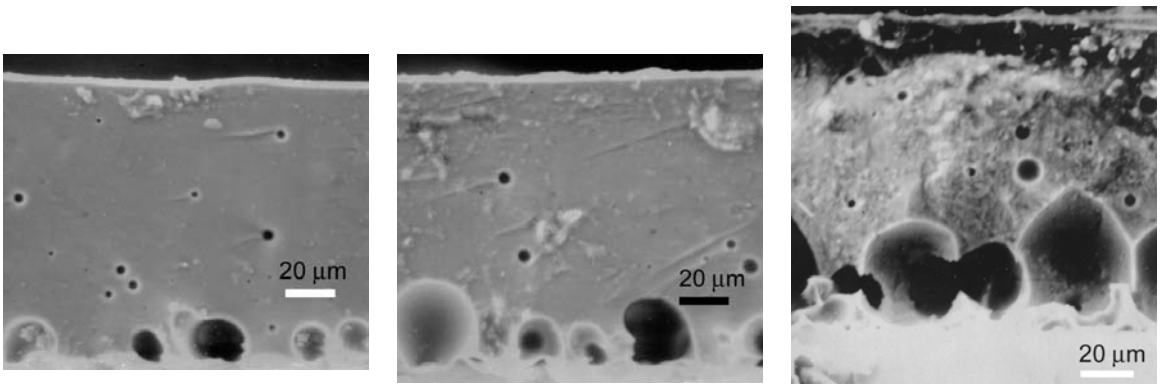

(a) (b) (c)

Figure 5.22. Fracture surfaces of the crystallizable glass films constrained on silicon substrate isothermally sintered at (a) 8 min, (b) 17 min, and (c) 3 hr.

Figure 5.23 shows the possible paths that the glass will follow during sintering and crystallization. Since the glass has attained near full density long before the appearance of the cordierite peaks, the glass essentially followed path D. Thus, if the large pores at the interface are ignored, this densification is a case of viscous sintering, which explains why the substrate constraint had no major effect on the densification. If B and C were followed, it would be a case of viscous sintering with inclusions [50] arising from crystallization. Once enough material has transformed, the crystals will form a rigid network effectively stopping any shrinkage. For a three-dimensional case, this begins at around 16% by volume[73]. Because the large pores at the interface are under constraint, they are not likely to shrink much further. Additionally, for the films that were fired at 950°C and higher, massive crystallization effectively prevented elimination of the large pores at the interface because the crystals would have formed a rigid network of "inclusions" in the remaining glass phase. Thus, even with some driving force to shrink the pores still present, the pores would persist even after long sintering times as observed in the glass-ceramic films sintered at 950°C or higher.

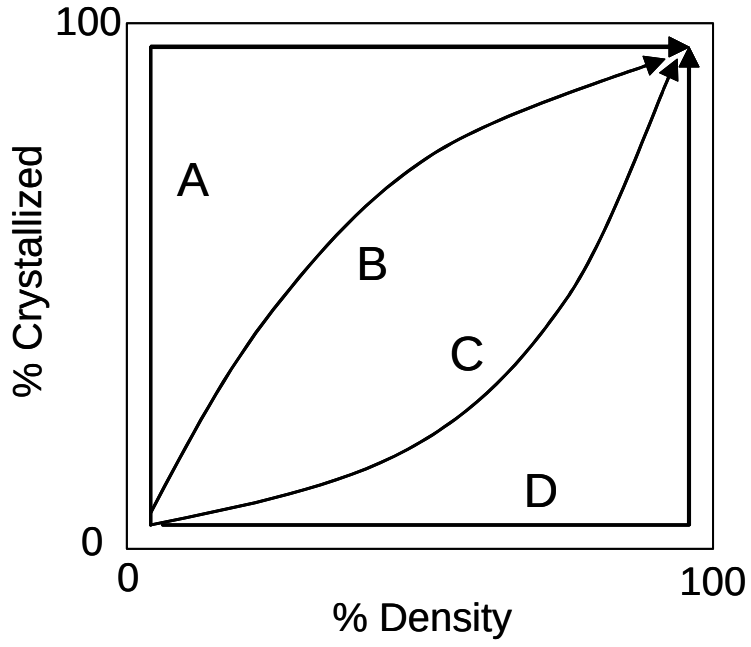

Figure 5.23. Schematic of the possible sintering and crystallization routes that the glass-ceramic may go through.

The schematics in Figure 5.24 summarize what could have transpired during the sintering of the glass-ceramic film on silicon, aluminum nitride and alumina. Among the three substrates, alumina gave the best result as far as bonding is concerned because of the near complete absence of pores at the interface. This may be attributed to the oxide that was in direct contact with the glass-ceramic film. The aluminum nitride did not fare well, most likely due to its relative inertness. Since pores did not form and grow at the glass-ceramic film/alumina interface, transformation of the glass into the cordierite phase may not be the cause of the pore formation at the interface between the glass-ceramic and silicon. Loss of wetting on silicon could have been caused by the disappearance of the oxide layer such that the glass film was "seeing" the bare silicon. Because the glass is of the $MgO\text{-}Al_2O_3\text{-}SiO_2$ composition, the native oxide on the silicon would be susceptible to reaction with the components of the glass, particularly the basic oxides. This possibility was put to the test and the results are discussed below.

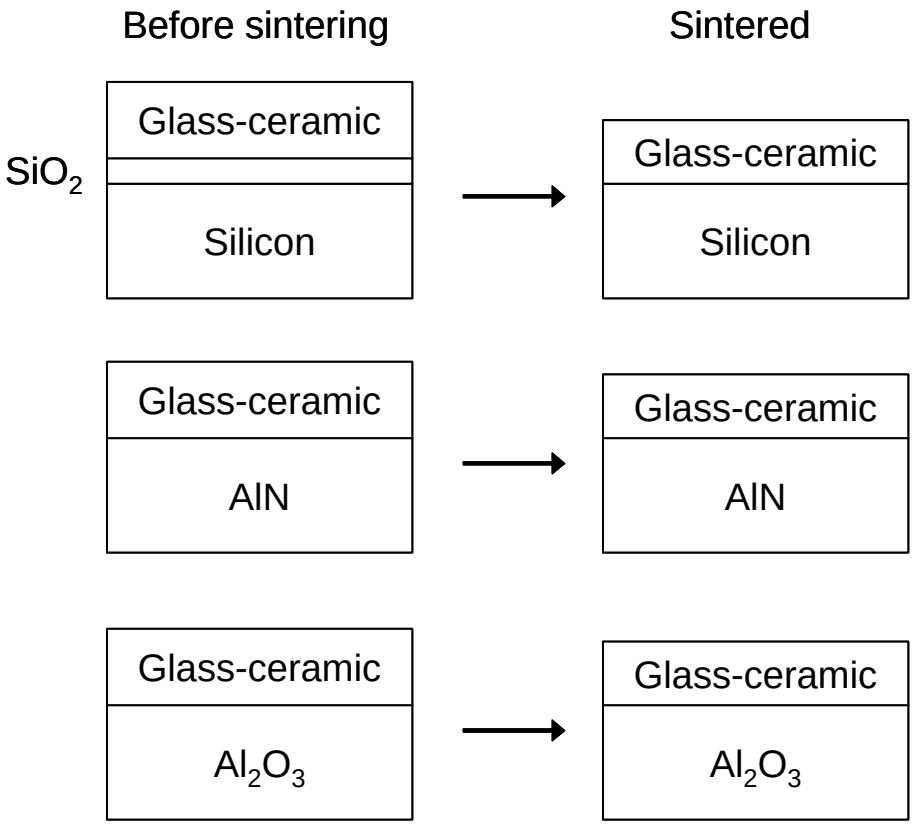

Figure 5.24. Schematic of the layer structures for the constrained glass films on different types of substrates used before and after sintering.

Cause of Pore Formation and Growth

The distinct possibility that the appearance of pores at the interface with the silicon substrate was caused by the loss of the native oxide layer can provide a solution to the problem. If the oxide layer can be thickened such that a film of the oxide remains after sintering, then in principle a clean interface devoid of pores would be attained. This scenario is illustrated below in Figure 5.25. To test this scenario, silicon wafers were heated to 900°C for up to 6 hours to increase the thickness of the oxide layer. The pre-oxidized silicon substrates were then coated with glass-ceramic slurry as was done for making the constrained films used in the previous experiments. The films were sintered at 950°C for 3 hours. The SEM micrograph of a constrained film after firing is shown in Figure 5.26. The number of pores at the interface was drastically reduced even with only a small increase in the oxide thickness on the silicon from the pre-oxidation step. The area density of the porosity was also observed using a scanning acoustic microscope (SAM). When the silicon substrate was used fresh, the SAM images in Figure 5.27 would be obtained. The interface region contains a high density of pores compared to the bulk and free surface of the film. When the silicon is pre-oxidized, SAM images such as those in Figure 5.28, which contain much less porosity at the interface region were obtained. Therefore, based on the numerous observations and indirect evidences presented, it is safe to conclude that the formation of pores at the interface with silicon is due to loss of wetting, which in turn is caused by the loss of the native oxide originally in contact with the film undergoing sintering.

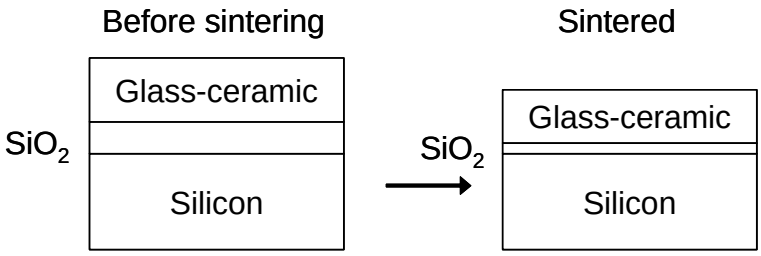

Figure 5.25. Schematic of the layer structure of a constrained crystallizable glass film on silicon substrate with residual silicon oxide on the substrate surface after sintering.

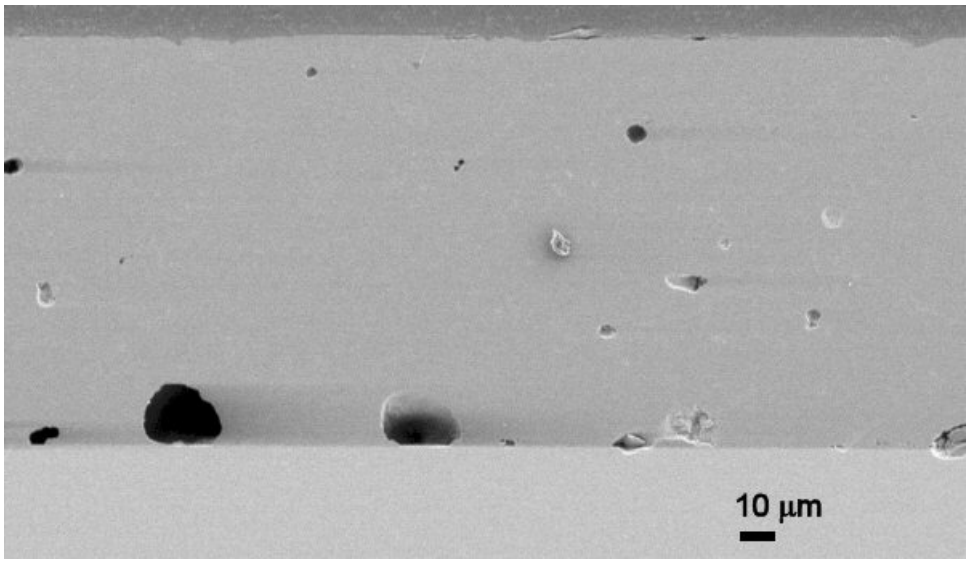

Figure 5.26. SEM micrograph of the cross-section of a glass-ceramic film constrained on a silicon substrate, pre-oxidized at 900°C for 6 hours, that was fired at 950°C for 3 hours.

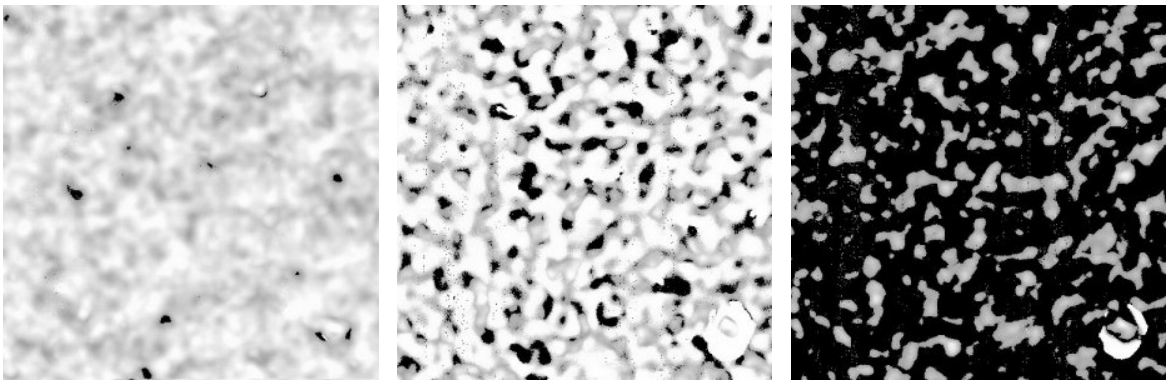

(a) (b) (c)

Figure 5.27. Scanning acoustic microscope images of the (a) top layer, (b) bottom layer (adjacent to substrate), and (c) glass-ceramic/silicon substrate interface of a glass-ceramic coating on silicon substrate sintered at 950°C for 3 hours.

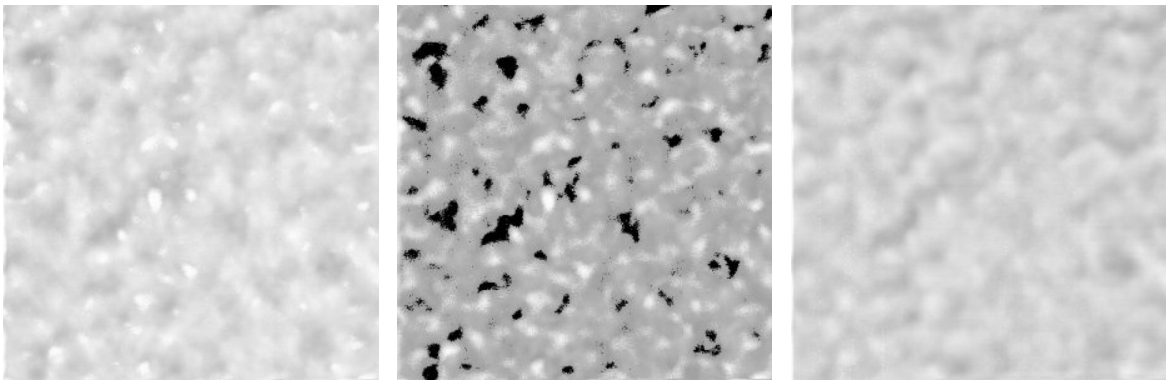

(a) (b) (c)

Figure 5.28. SAM images of a glass-ceramic coating on silicon substrate sintered at 950°C for 3 hours with the silicon substrate heated at 900°C for 3 hours in air prior to coating with the glass-ceramic slurry: (a) top layer of glass-ceramic, (b) bottom layer adjacent to substrate, and (c) substrate surface.

In-plane Stresses during Constrained Sintering

The in-plane stresses in the films constrained on silicon were determined using the same procedure followed for the zinc oxide films. The curves obtained from the 10 μm crystallizable glass powder at two sintering temperatures are shown in Figure 5.29. The coatings on the silicon substrates were initially under compression (negative stresses on the plots). When the temperature started ramping up to the sintering temperature, a dip was also observed similar to that of the ZnO curves because of a momentary temperature gradient across the sample thickness. At the 900°C sintering temperature, the stress rose to around 100 kPa (~ 300 kPa increment from initial state) before falling off to near zero. This is similar to the results obtained from the sintering of constrained non-crystallizing borosilicate glass [74] where the film stress quickly dropped back to zero after it rose to 20 kPa. Addition of non-sintering inclusions of silica particles up to 20 % by volume to the glass raised the peak maximum stress close to 40 kPa and at the same time caused the stress to relax more slowly to a tensile residual stress.

For 950°C sintering temperature, the stress quickly rose to near zero then dropped to slightly below zero, an incremental increase of around 200 kPa from the initial stress

state. The stress remaining below zero is a result of the expansion that reverses the curvature of the substrate putting the film in net compressive stress. The stress remained at the same level until after nearly 100 minutes into the isothermal sintering regime when it increased to just below 900 kPa and then remained there. Since the time when the increase took place is already well into the isothermal stage and way past the end of film expansion, it is very likely the increase in the stress was caused by the massive presence of the crystalline cordierite phase that interfered with the ability of the remaining glass phase to relax the stress when the large pores started to shrink. The cordierite crystals acted like inclusions in the film, similar to the case where rigid inclusions were intentionally added[50,74] but with a larger fraction of the inclusion. Since the transformation to the crystalline cordierite phase was continuing, the inability to relax the stress was compounded even further.

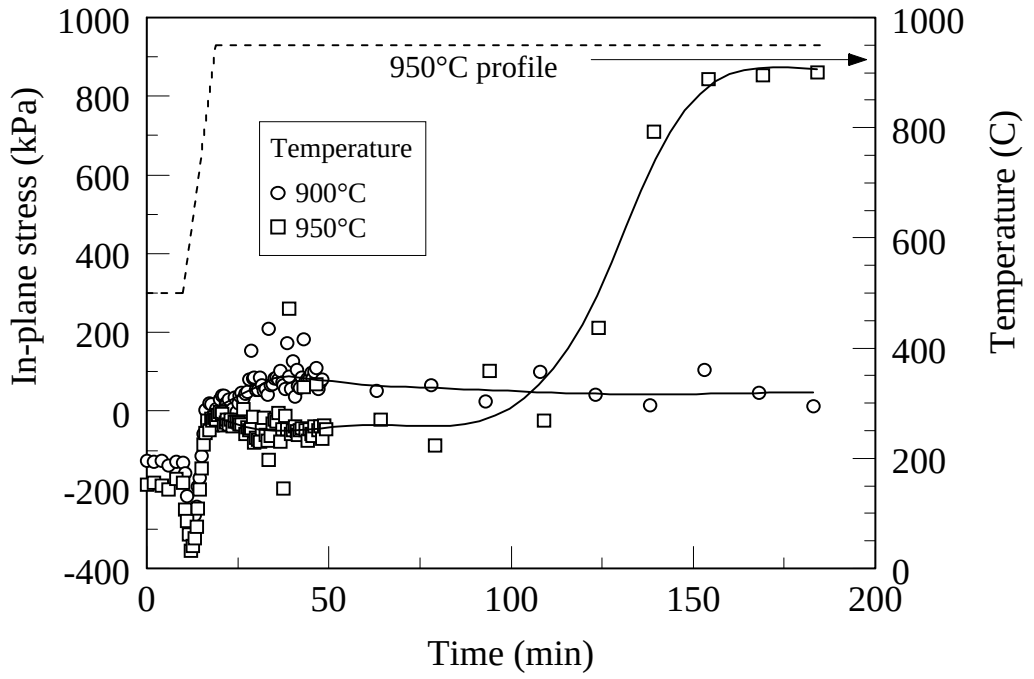

Figure 5.29. In-plane stresses during the sintering of crystallizable glass (10 μm powder) films constrained on silicon substrate.

In-plane stress curves were also obtained on the films from the 3.97 μm powder (Figure 5.30). The coatings were initially under tension (positive on graph) brought about by the large drying shrinkage. At 875 and 900°C, the stresses quickly dropped to

zero. On the other hand, at 950°C, the stress dropped below zero, the reversal being brought about by the film expansion as the pores formed and grew at the interface. As was the case with the 10 μm powder film samples, the stress also reversed back to the tensile regime and rose to an apparent value of over 3 MPa. The discrepancy between the two powders may be traced to the following. The ratio of the film thickness to the pores from the thick coatings (10 mil films) was assumed to carry over into the thinner coatings. Obviously, this was not the case since the interface condition did not change and so the pores would grow to about the same size, such that the corresponding thicknesses were underestimated in both instances. The calculated stresses would then be exaggerated but to different extents. The slurry from the 10 μm glass powder shrank less compared to that from more dilute slurry with the 3.97 μm powder. Because the film with the finer powder also had a lower green density, the net result is a thinner film in the dried state. The resulting film to pore ratio would be larger such that the actual average stress should be lower than reported.

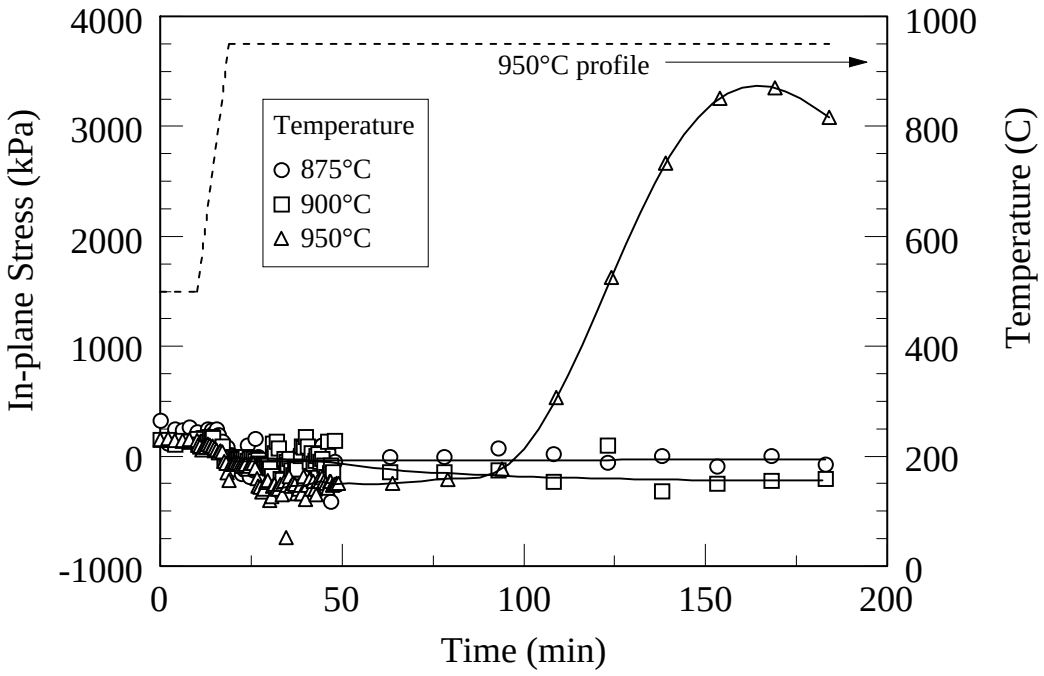

Figure 5.30. In-plane stresses at different sintering temperatures in crystallizable glass films (3.97μm powder) constrained on silicon substrate.

5.3 Summary

Densification profiles from constrained and freestanding films of the crystallizable glass were very similar up to a range of relative densities in excess of 90%, particularly at the higher sintering temperatures, such that it is reasonable to assume that substrate constraint did not have a significant effect on the densification of the glass film. Compensating for the pore formation early in the sintering runs, the activation energy for densification was comparable to the activation energy of 1077 kJ/mole calculated from the annealing and softening points of the glass, indicating the densification was primarily controlled by viscous flow mechanism. The massive formation and growth of pores during sintering at the interface with the substrate of films constrained on silicon was traced to the loss of the native oxide due to a reaction with the glass. A pre-oxidation step at 900°C of the substrate before coating with the glass slurry substantially reduced the occurrence of the pores at the interface, confirming this conclusion. In-plane stresses were obtained for the constrained films on silicon from the substrate curvature measurements. At 900°C or lower, when the glass has not undergone significant transformation to the crystalline cordierite phase, the films behaved just like non-crystallizing glass where the stress rose to a small value before quickly relaxing. At 950°C, the stress in the film rose slightly before reversing to the compressive state as the pores at the interface formed and grew. About halfway into the 3-hour isothermal sintering run, the stress reverted back to the tensile state and increased to nearly 900 kPa for the film from the 10 μm glass powder. The increase in the stress is believed to be caused by the pores undergoing some shrinkage but with the large amount of crystalline phase preventing the dissipation of the stress.

Chapter 6
Applications of Sintered Coatings on Rigid Substrates

6.1 Electrostatic Chucks

Electrostatic chucks (ESC) represent a technological advancement over mechanical chucks for semiconductor wafer handling. Several advantages have been cited as compelling reasons for adopting the technology in semiconductor processing. However, for these chucks to operate at high temperature, the dielectric coating must be a non-polymer material with sufficiently high electrical resistivity at the operating temperature. Reliable chucks based on ceramics are difficult to process because of the high firing temperatures and the inherent brittleness of ceramic materials. Consequently, the associated costs can be prohibitively high. A process based on cofired glass, glass-ceramic or ceramic coating may provide a method to fabricate highly reliable chucks at a much lower cost.

Electrostatic chucks differ from mechanical chucks in several ways. In a mechanical chuck, the wafer is held in place along its periphery such that the force is concentrated on the actual contact area of the clamping ring. This uneven force distribution can cause the wafer to bow. This in turn can result in poor heat dissipation through the chuck and can cause serious problems in the circuit fabrication itself. The available wafer area for die fabrication is also reduced. In electrostatic chucks, the electrostatic force is distributed more uniformly throughout the contact area between the chuck and the wafer. This not only improves heat dissipation but also increases the flatness of the wafer by forcing it to conform to the chuck surface. Because no chucking mechanism is in direct contact with the top surface of the wafer, using electrostatic

chucks should also minimize particle contamination resulting in higher yields and lower failure rates.

Commercial electrostatic chuck designs utilizing polymer coatings as dielectric layers are available but they are useful only at relatively low temperatures. High-temperature chucks require coatings that not only can withstand process temperatures but can also maintain sufficiently high electrical resistivity at elevated temperatures. Many ceramics and some glass systems can meet these specifications. One issue that needs to be addressed is how to process them into low-cost, high-reliability chucks that can be scaled-up to keep up with the trend of increasing wafer diameter.

Working Principle of Electrostatic Chuck

Electrostatic chucks rely on coulombic forces to attract or clamp down objects that come into contact with it. These forces arise from the separation of charges across the dielectric when a potential difference exists between the electrodes. The principle is very much similar to a capacitor[75,76] in which the charge separation creates an attractive pressure between the electrodes. For two parallel plates in a vacuum separated by a distance h and a potential difference V, the clamping or attractive pressure P is given by:

$$P=\frac{\varepsilon_o V^2}{2h^2} \tag{6.1}$$

where ε_o is the permittivity of a vacuum. In the case of an electrostatic chuck, however, the space between the two electrodes is filled with a solid dielectric material of thickness h_d and relative dielectric constant k. Assuming that there is perfect contact between the wafer and the dielectric, i.e., no air gap, Eq. (6.1) becomes

$$P=\frac{\varepsilon_o k V^2}{2h^2} \tag{6.2}$$

This is represented schematically in Figure 6.1(a) and 1(b). Figure 6.1(c) graphically illustrates the dependence of the clamping pressure on the applied voltage, V. A more realistic model[77,78], however, takes into account the presence of an air gap of thickness, h_{gap}, between the bottom surface of the wafer and the top surface of the

dielectric. In this model, part of the voltage drop occurs across the air gap such that the expression for the clamping pressure in Eq. (6.2) becomes

$$P=\frac{\varepsilon_o V^2}{2\left(\frac{h_d}{k}+h_{gap}\right)^2} \tag{6.3}$$

Equation (6.3) reveals some interesting features that are not found in Eq. (6.2). There are two limiting case that arise from the equation. In the case of a dielectric with a very high k, the voltage drop occurs essentially across the air gap such that the clamping force does not increase indefinitely (as Eq. (6.2) would suggest) but approaches a limiting value given by:

$$P=\frac{\varepsilon_o V^2}{2\left(h_{gap}\right)^2} \tag{6.4}$$

The other case occurs when the air gap approaches zero. In this case, Eq. (6.3) reduces to the commonly reported form:

$$P=\frac{\varepsilon_o k^2 V^2}{2\left(h_d\right)^2} \tag{6.5}$$

Note that Eq. (6.5) differs from Eq. (6.3) by a factor of k. Equation (6.3) will form the basis for the analysis of the clamping force data obtained in this research.

Design and Advantages

Two major reasons that are often cited for the adoption of electrostatic chucks are particle generation and contamination, and wafer temperature control[79,80]. Wafer handling systems employing mechanical clamping contain moving parts that are potential sources of particle contaminants. Thus, to minimize particle contamination, the mechanical parts have to move slowly. In contrast, electrostatic clamping systems can generate clamping pressures that enable rapid movement and since there are no moving parts in the chucking devices, particle contamination is virtually eliminated. In processes that are carried out at elevated temperatures such as those involving plasma, wafer temperature control and uniformity are important. In systems using mechanical chucks, clamping is confined to the periphery resulting in a nonuniform force distribution over the wafer surface. This causes the wafer to bow when pressurized cooling gas is injected

through the substrate. The mechanical clamps themselves can cause an additional curvature on the wafer. This can seriously affect the optolithography process due to depth of field issues. An electrostatic chuck on the other hand exerts a force that is distributed according to the electrode layout, which is much more uniform than that in a mechanical chuck. This not only improves the flatness of the wafer but also ensures a more uniform heat transfer over the entire wafer surface.

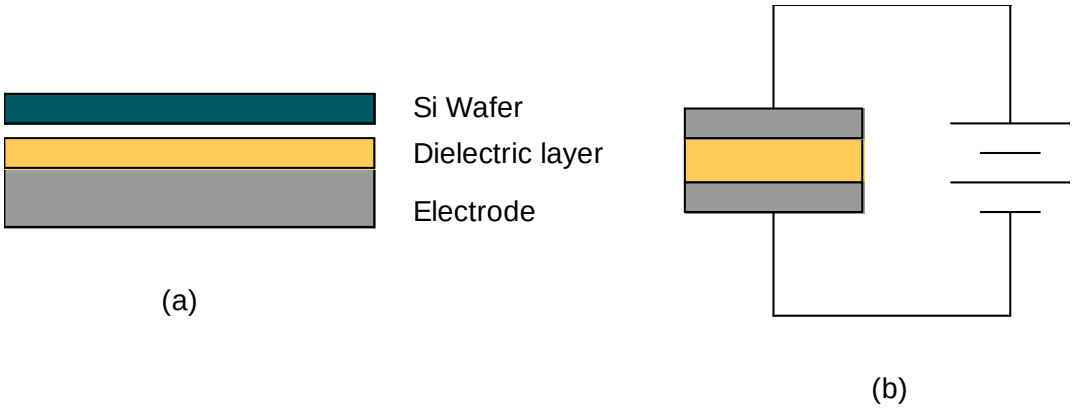

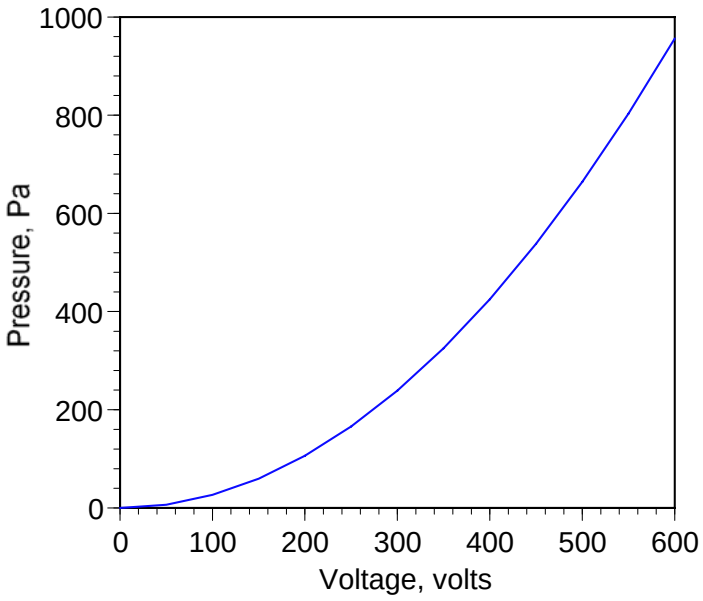

(c)

Figure 6.1. Schematic representation of (a) wafer-electrostatic chuck configuration, (b) equivalent capacitor circuit, and (c) graphical dependence of clamping pressure on applied voltage for a simple parallel plate configuration.

Electrostatic chucks come in three basic configurations[78-80]. These include the monopolar design which is essentially a parallel-plate capacitor with a solid dielectric material filling the gap. The wafer rests on top of the insulating layer (Figure 6.1(a)) and serves as the other electrode. To complete the electrical circuit, an electrical connection to the wafer is necessary. In plasma etching and deposition processes, the plasma serves as the electrical connection. Among the three, this configuration generates the largest clamping pressure for comparable voltages[78-81] and can be described by Eq. (6.3). The design is also simple and straightforward such that it is relatively easy to fabricate.

The other configurations are a bipolar ESC and interdigitated electrodes (IDE). In a bipolar design, two coplanar electrodes are separated from the wafer by an insulating layer effectively forming two capacitors in series. This design does not require an electrical connection to the wafer to complete the circuit. However, the voltage is divided between the two electrodes such that the resulting clamping force is only a quarter of the clamping force in a monopolar chuck. Therefore, the clamping force has to be boosted by some other means such as reducing the thickness of the dielectric or using a higher k material. This, coupled with the more complex electrode arrangement, makes the manufacturing process more difficult. The interdigitated design consists of an interleaved pair of electrodes separated and covered by a thin layer of insulating material. This, too, does not require an external electrical connection to the wafer to operate. The clamping force is also lower than that produced by a monopolar chuck. By referring to the force equation, the parameters that determine the performance of an ESC design can be obtained. Because the main objective is to obtain a reasonably high clamping pressure, this can be achieved by increasing the voltage, the dielectric constant and the effective contact area. On the other hand, the thickness of the dielectric must be reduced to obtain a similar effect.

Glass-ceramic-Metal Electrostatic Chucks

In order for an electrostatic chuck to deliver the desired performance, it is important to select materials with the required properties[78-80]. For the insulating or dielectric layer, its electrical properties are of primary importance. Another property that must not be overlooked is its coefficient of thermal expansion (CTE). Since the

dielectric is going to be cofired with an electrically conductive material that will serve as the electrode, it is important that the two materials will have comparable CTE. The adhesion strength of the dielectric to the substrate is also critical to ensuring reliability and robustness of the device.

Most of the common ceramic materials and glasses have outstanding insulating properties[15]. Polymers also have excellent electrical resistivities but they are suitable only for low temperature applications because of their inability to withstand high temperatures. This leaves ceramics and glasses as candidate materials for high-temperature electrostatic chucks. One major disadvantage of ceramic materials is that they require very high processing temperatures to attain reasonably dense films or layers. To keep the process simple and inexpensive, processing temperatures below 1000°C are desirable. Most glasses can be sintered below 1000^{o}C but ordinary glasses cannot maintain high electrical resistivity at elevated temperatures. However, some like the alkali-free glasses provide resistivities approaching those of their ceramic counterparts. This is graphically illustrated in Figure 6.2 that shows the electrical resistivities of 3 glass compositions as a function of temperature. Two of the glasses, SCE-505 and SCE-5 (Sem-Com Co., Toledo, OH), are alkali-free and the other glass contain alkali elements, mainly sodium. In alkali-containing glasses, the resistivity quickly drops with temperature because of the increased mobility of the ions in the glass. As an insulating layer, SCE-505 and SCE-5 were therefore considered to be more suitable and both glasses can be sintered at 900 to 950°C.

SCE-505 is a crystallizable glass with a CTE of 4.6 x 10^{-6}/C in the amorphous state and 4.1 x 10^{-6}/C in the crystalline state. SCE-5 is an aluminosilicate glass and has a CTE of 6.4 x 10^{-6}/C. The substrate must have a CTE that is reasonably close to that of the dielectric material to minimize the stresses that arise from CTE mismatch. The stress in the dielectric layer can quickly be estimated using a simple equation given below:

$$\sigma = \frac{E}{(1-\nu)}(\Delta\alpha\Delta T) \tag{6.6}$$

where E is the Young's modulus of the glass, ν is the Poisson's ratio, $\Delta\alpha$ is the CTE mismatch and ΔT is the change in temperature. For a high-modulus glass like SCE-505,

a CTE mismatch of around 8 ppm and a temperature change of 800°C, can easily produce internal stresses in excess of 1GPa. Ideally, the CTE of the substrate should be such that the ceramic layer will be under slight compression at all temperatures up to the operational temperature. Although SCE-505 glass adhered well to stainless steel, its CTE of around 11 or 12 ppm eliminated it from consideration. A metal substrate that fits the requirement is pure molybdenum with a CTE of around a 5 ppm. This combination would put the glass-ceramic coating under compression but not high enough that it would cause the coating to fail.

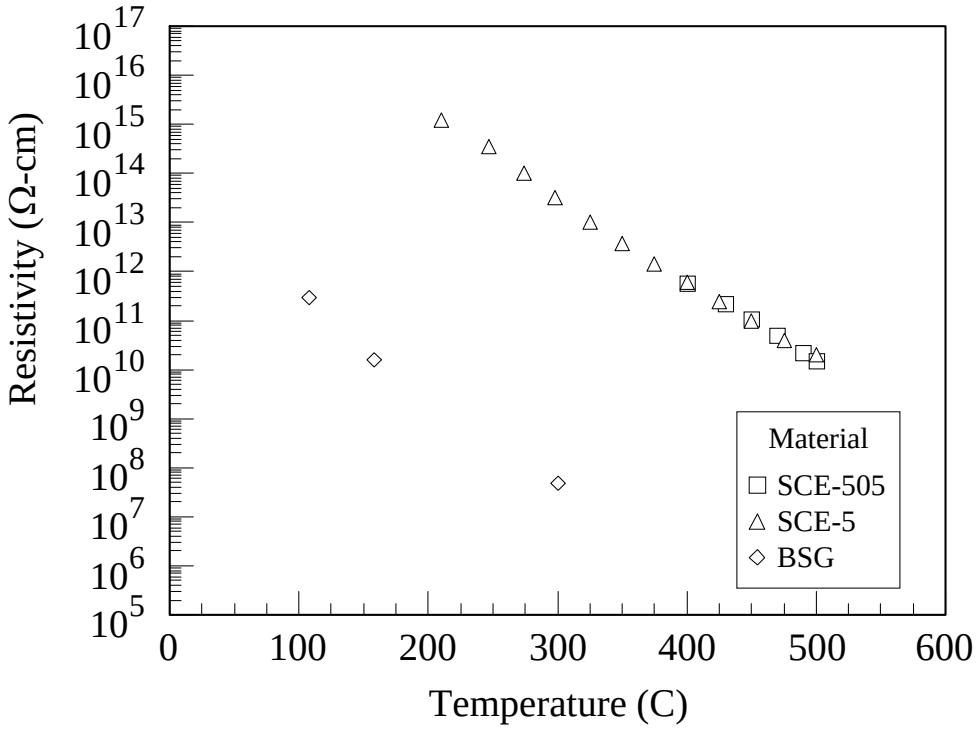

Figure 6.2. Electrical resistivity of some glass and glass-ceramic materials.

One problem with molybdenum is that it cannot be fired in air, as it would form a volatile oxide (molybdic oxide) above 500°C. Another issue that must be dealt with is the adhesion of the glass-ceramic coating. Except for the large CTE mismatch between the glass-ceramic and stainless steel, the glass-ceramic adhered very well. One explanation[82] is that the good adhesion between the glass and the steel is due to an adherent oxide on the surface of the parent metal or alloy that serves as the "glue"

between the two layers. Stainless steel alloys derive their resistance to oxidation from the formation of a strong, stable, hermetic film of chromium oxide on the surface. This oxide film is what the glass "sees" and not the underlying metal alloy, and thus forms a very strong bond with the substrate. Therefore, a method must be found to reproduce this adherent oxide on the molybdenum surface

Electroplating of Ni or Cu and Cr

Unlike stainless steel, molybdenum does not form an adherent oxide layer on its surface such that it was necessary to "engineer" the surface of the substrate to recreate the surface condition found in stainless steel. This was achieved by electroplating[83,84] either nickel or copper on the substrate followed a second layer of chromium. Depositing an initial layer of Ni (or Cu) made the electroplating of Cr easier than when it was done on bare Mo. Electroplating can be carried out in a cell consisting of an anode and a cathode immersed in an aqueous medium containing the ions of the metal to be plated. Since the electroplating reaction is not autogenous or self-initiating, an external current source is used to drive the plating reaction. The schematic of the plating cell used for nickel is shown in Figure 6.3. The anode is made of nickel (or copper) and is slowly eaten away during the plating process. The article being plated, in this case the Mo chuck substrate, serves as the cathode. Adhesion of nickel (or copper) to molybdenum in the as-plated condition was moderate such that the plated substrate was initially annealed at 600°C in He-H_2 for 1 hour to improve the bonding between nickel and molybdenum before plating the substrate with chromium. Electroplating of chromium was done in a similar cell with little modification. It did require a much higher plating current density (200 mA) for plating to proceed and an anode other than Cr can be used such as 93Pb-7Sn alloy, which was cheaper.

Casting of Glass-ceramic Coating and Sintering

The slurry was prepared in the same way as described in Chapter 3. It was applied to the molybdenum substrate using a doctor blade or casting knife. A copper ring collar, basically a flat copper gasket, with an inner diameter similar to that of the substrate diameter was attached to the substrate to extend the casting surface and move

the tapering effect away from the substrate edge. The casting knife was set to produce a sintered thickness of 75 to 125 μm. Previous tests showed that the film shrinks to about 30 to 35% of the doctor blade setting during drying. The extent of shrinkage during sintering will depend on the initial density of the tape or film. The green or unfired coatings were found to have densities of around 60 % of the theoretical density of the crystallized form of the glass-ceramic.

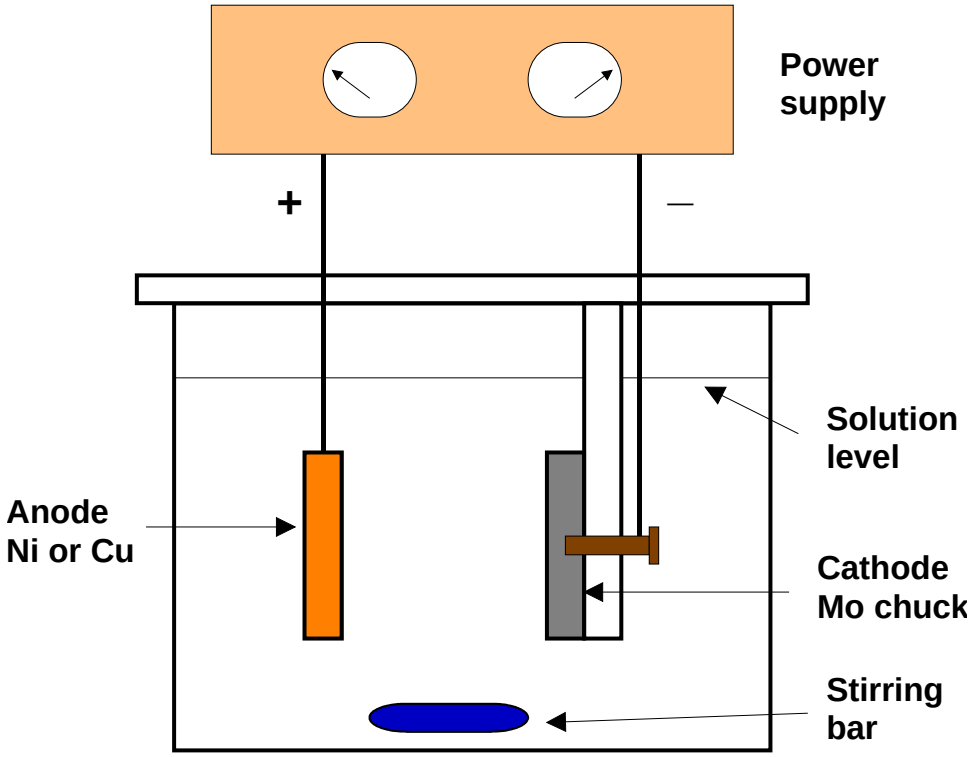

Figure 6.3. Schematic of the electroplating cell used to deposit the metal layers.

The coating was fired in a tube furnace with a reducing atmosphere of helium and hydrogen mixture. This was necessary because molybdenum oxidizes readily above 550^{o}C. A mixture containing 10% H_2 was found to be adequately reducing to prevent undesired oxidation of the substrate. Higher hydrogen partial pressures, e.g., 90 % or pure hydrogen, caused deterioration in the mechanical properties of the glass-ceramic. Adhesion is also poor, perhaps due to the reduction of the oxide layer at the interface. The firing procedure used is as follows: The temperature is slowly raised (~2^{o}C/min) to 450 or 500^{o}C for binder burnout. This is carried out in air to ensure a sufficient supply of oxygen to burn off the organics in the green tape. This stage typically lasted for 3 hours.

After binder burnout, the furnace was covered and purged with the reducing gas and the temperature raised to 950°C to sinter and crystallize the glass. This stage lasted 3 hours. Most of the densification actually takes place in the first 30 minutes but a longer sintering time is necessary to maximize the formation of the crystalline phase. Sintering is immediately followed by cooling to room temperature. A chuck made using this process is shown in Figure 6.4 after polishing the SCE-505 glass-ceramic coating. The grooves on the surface are intended for the flow of cooling gas. The measured electrical resistivities of the coating with temperature are plotted in Figure 6.5. If the downward trend continues and a resistivity of 10^8 Ω-cm is taken as the minimum, then the chuck should be able to perform above 500°C, possibly up to 600°C.

Figure 6.4. Fired glass-ceramic/molydenum electrostatic chuck after polishing of the glass-ceramic (SCE-505) layer.

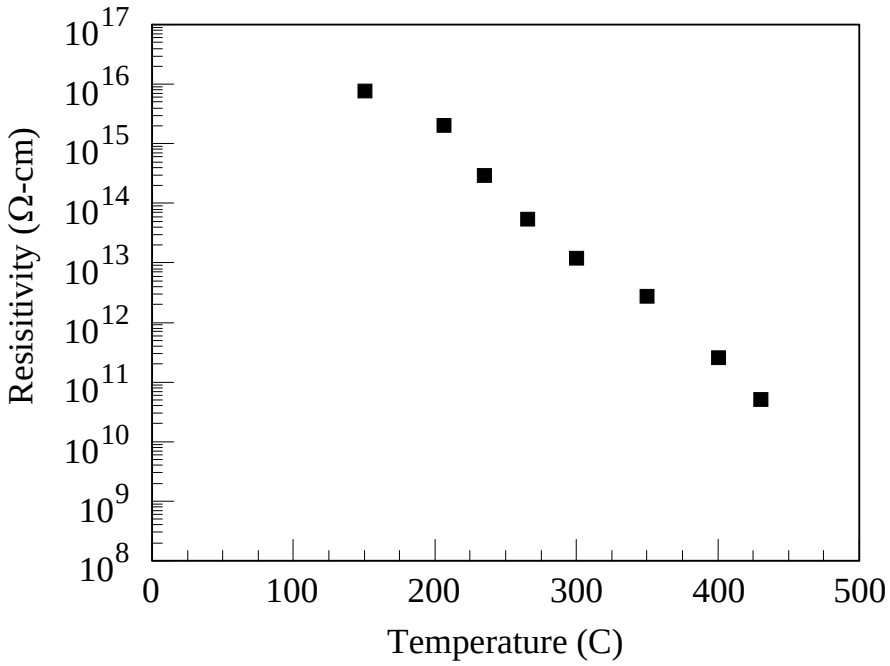

Figure 6.5. Electrical resistivity of the SCE-505 glass-ceramic coating on the Cr/Ni-plate molybdenum substrate.

The images in Figure 6.6 show the layered structure at the interface region between the electroplated Mo substrate and the glass-ceramic. The image on the left (Figure 6.6(a)) is a glass-ceramic coated substrate with Ni and Cr metallization while the other image is that of a coated substrate with Cu and Cr metallization. The boundary between the metal layers is not visible due to interdiffusion of the elements. This is clearly seen in the elemental plots in Figure 6.7 and Figure 6.8. In the case of the Ni/Cr metallization, the nickel layer was penetrated by both Cr and Mo. On the other hand, there appears to be little alloying in the copper layer although some Cr atoms seemed to have crossed the Cu layer and deposited in front of the Mo substrate. To the right, away from the substrate, the plots show a transition layer about 1 μm consisting of Cr oxide and the glass-ceramic components. This structure was found to produce a fired coating with unusually strong adhesion to the substrate which allows the chuck withstand extreme temperature swings (e.g., immersion in liquid nitrogen followed by exposure to 300°C). If Mo managed to diffuse to the surface due to insufficient metallization thickness, the adhesion was poor.

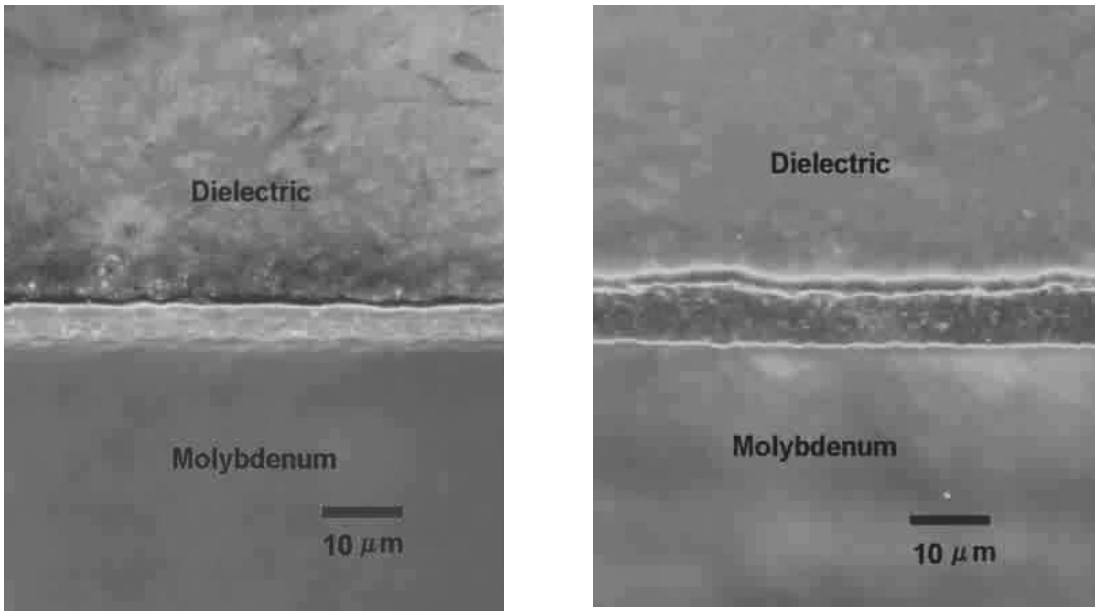

(a) (b)

Figure 6.6. Cross-sections of the dielectric/molybdenum substrate interface showing the (a) Ni-Cr and (b) Cu-Cr metal layers.

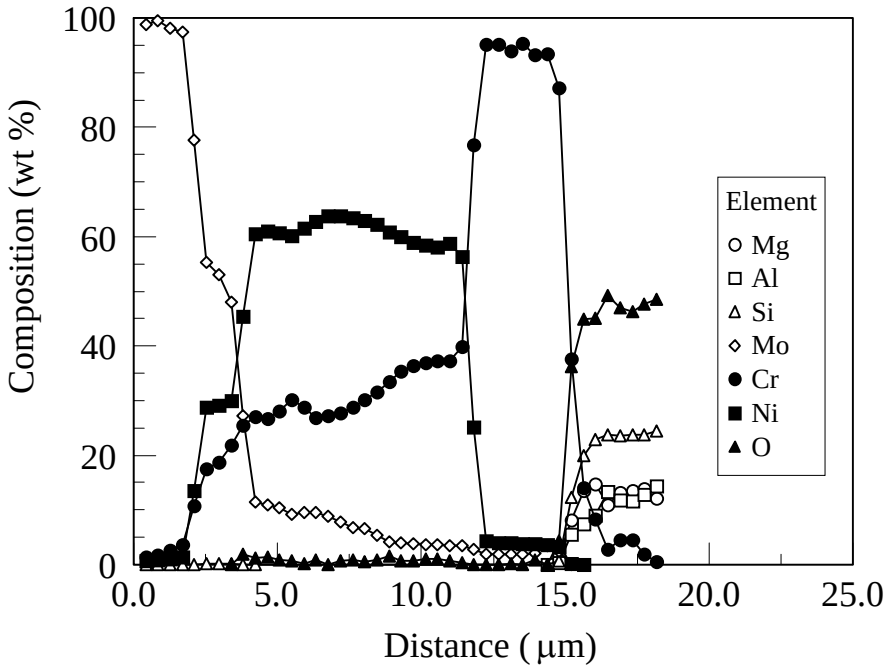

Figure 6.7. Elemental analysis of the region between the glass-ceramic and the molybdenum substrate showing the Ni and Cr layers.

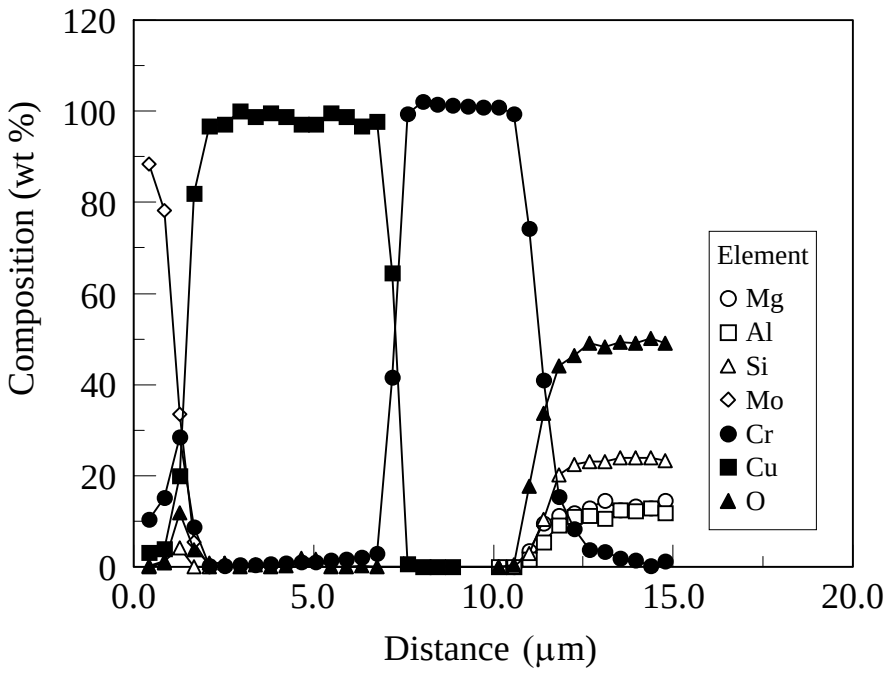

Figure 6.8. Elemental analysis of the region between the glass-ceramic and the molybdenum substrate containing the Cu and Cr metal layers.

The performance of an electrostatic chuck design is gauged by the clamping force (or pressure) that can be developed when a high voltage is applied across the dielectric layer. An inexpensive apparatus was designed and assembled to measure the clamping force in the demonstration chucks. The representative schematic of the assembly is shown in Figure 6.9. It consists of a large-diameter quartz tube chamber mounted between two stainless steel plates that can be evacuated to under 10 mtorr. The chuck is mounted on top of a disk-shaped heater that can heat the chuck rapidly to the desired temperature. The upper electrode consists of a copper-plated alumina disk that is clamped to an aluminum plate. The structure is in turn attached to a load cell that can be moved up and down as required by means of a motorized screw micrometer holding the load cell-electrode assembly. The voltage source is attached to the upper electrode while the chuck substrate is set to ground. Previously, a silicon wafer attached to an aluminum disk with a conductive epoxy had been used as the top electrode to simulate the actual wafer-chuck contact. However, the distortion of the wafer that occurs when the epoxy is

cured caused inconsistent results. The wafer also tended to debond at higher operating temperatures.

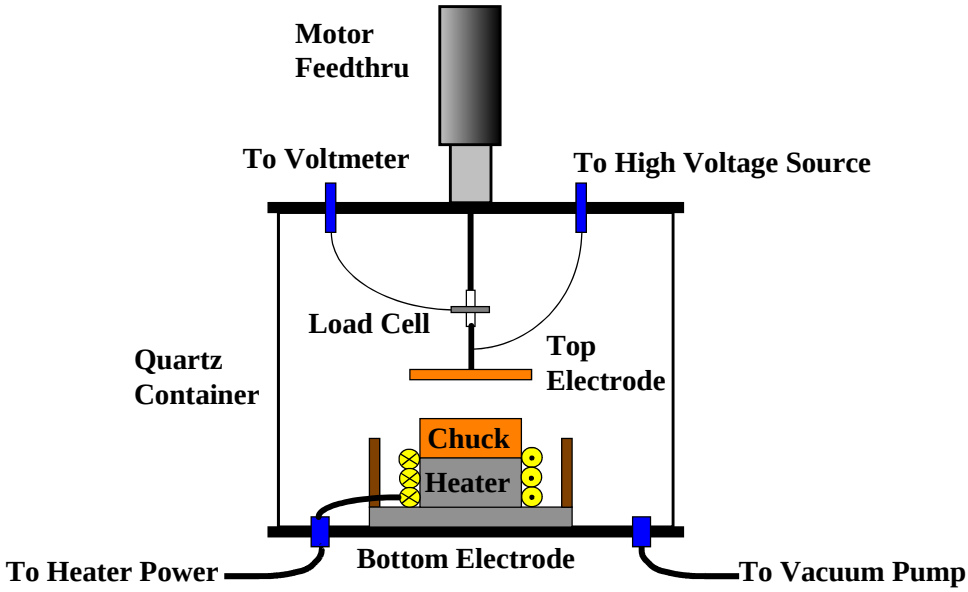

Figure 6.9. Apparatus used for measuring the clamping force of the electrostatic chuck.

Measurements of the clamping pressure at several temperatures are shown in Figure 6.10. The chuck was not tested at higher temperatures due to limitations on the equipment's ability to withstand higher temperatures. The curves generally followed a parabolic shape as predicted in Eqs. (6.1) to (6.5). A slight deviation at higher voltages at 300°C was probably caused by slippage of the connecting rod to the load cell and adhesive on the load cell cover softening due to the heat. The clamping pressure also increased with increasing temperature but was only realized above 200^{o}C, perhaps 250^{o}C. The increase in the clamping force with temperature may be attributed to the following. The dielectric constant, κ, of the glass-ceramic coating was found to increase with temperature (Figure 6.11) and this increase becomes noticeable above 250°C. In Eq. (6.3), an increase in the dielectric constant reduces the denominator resulting in an increase in the clamping pressure. Another effect that could come into play is the change in the flatness of the chuck surface. At the sintering temperature, the chuck surface is flatter than it is at room temperature because the effect of thermal coefficient of expansion (TCE) mismatch is absent. By raising the temperature, this flatness can partly be recovered resulting in an increase in the contact area and thus in the observed

clamping force. Polishing can only partially eliminate the curvature of the chuck at room temperature unless it is done for a very long time. Still another possibility is the faster diffusion of ionic species in the dielectric due to the increase in temperature, thus increasing the charge separation and shortening the time to reach the equilibrium value.

The declamping curve for the chuck is shown in Figure 6.12. The average of the damped oscillation curve is also plotted. With the equilibrium at 10 mV, the declamping time would be less than 1 ms. The declamping time is an important characteristic of the electrostatic chuck. A short declamping time would translate to a higher processed wafer throughput. Sticking occurs when residual electrostatic forces remain after the electrode voltage is turned off. The decay rates of these forces depend on how fast the separated charges can recombine. In highly insulating dielectric layers, recombination through the dielectric can be a very slow process due to the low mobility of ions in the film. Simply zapping the charge off through the wafer with a conductor may not necessarily work, especially if the wafer backside has an insulating layer. Even if this were possible, damage to the circuits may occur.

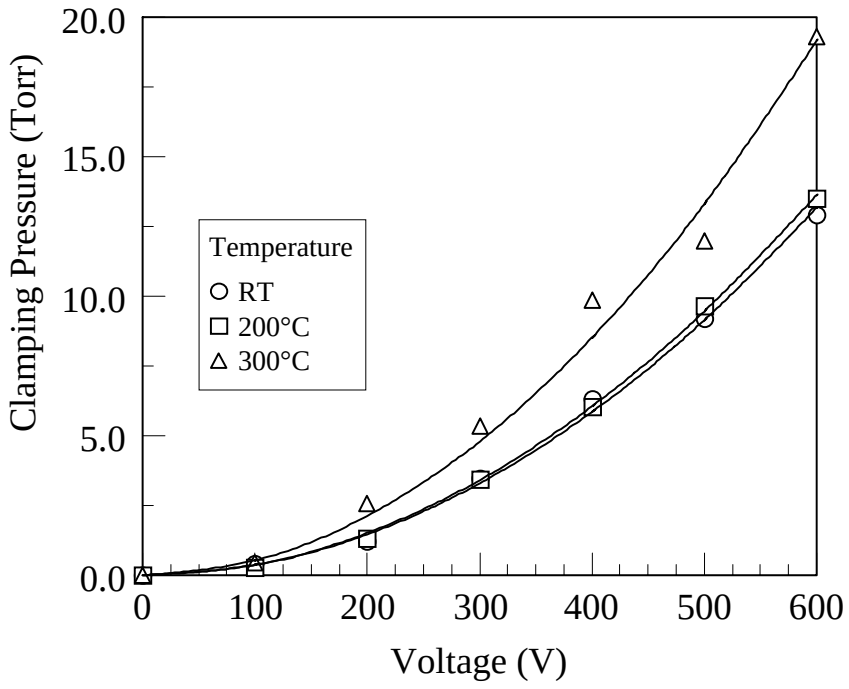

Figure 6.10. Clamping pressure at different applied voltages and operating temperatures for the glass-ceramic coated molybdenum chuck.

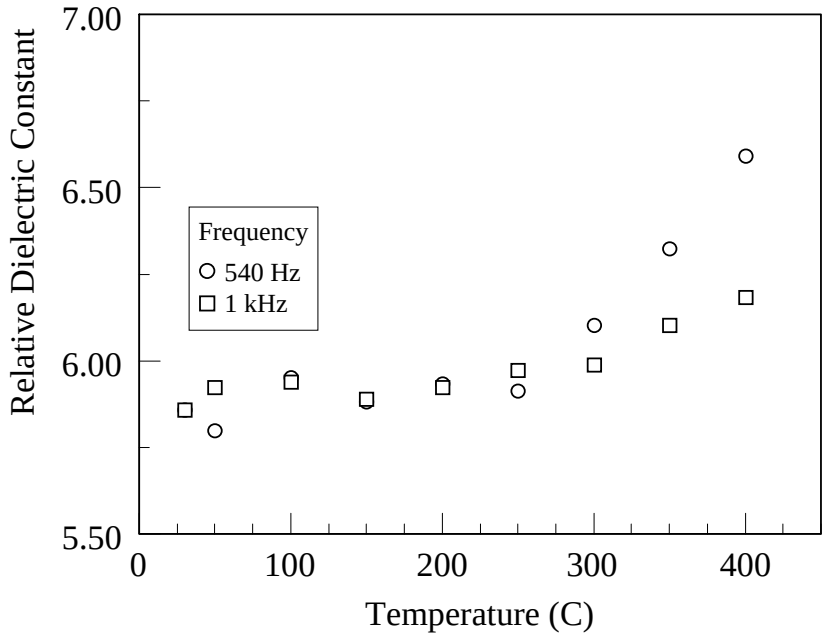

Figure 6.11. Dielectric constant of the SCE-505 cordierite glass-ceramic versus temperature.

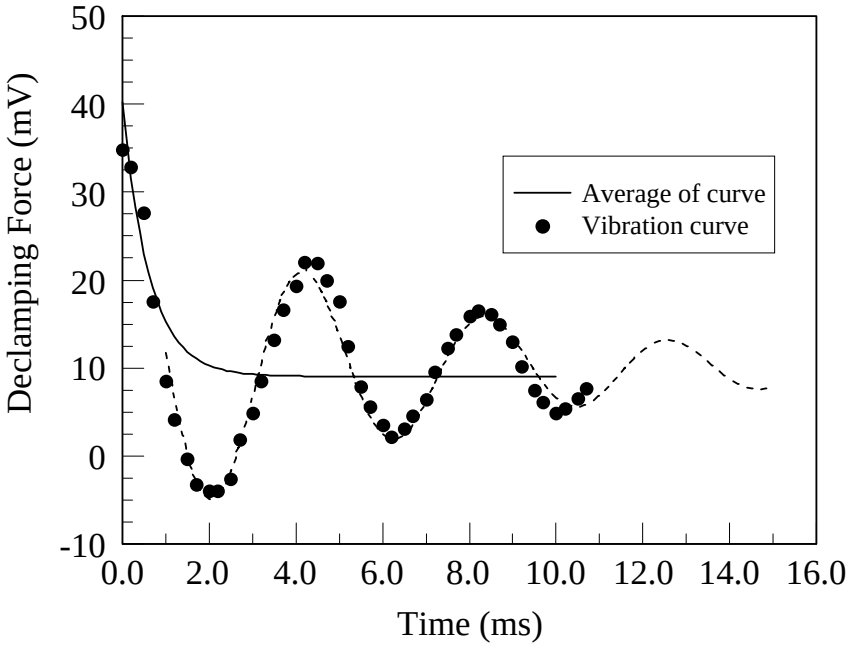

Figure 6.12. Experimental clamping force decay curve at room temperature for an applied voltage of 600 volts.

Glass-Ceramic Electrostatic Chucks

The ceramic chuck was constructed using alumina as the substrate and an alumino-silicate glass (SCE-5, Sem-Com Co. Toledo, OH) as the dielectric coating. SCE-5 was selected over SCE-505 because it has a higher CTE and, thus, a better match for the alumina substrate. A silver-palladium paste (DuPont 6023) was used as the electrode material over plain silver paste, which had a higher tendency to diffuse into the glass during firing based on the observed discoloration of the glass. The coating scheme for the chuck is shown in Figure 6.13. A three-layer structure was adopted because the Ag-Pd/alumina structure was susceptible to debonding, especially for a wide-area electrode pattern. The procedure for making the chuck is briefly described below.

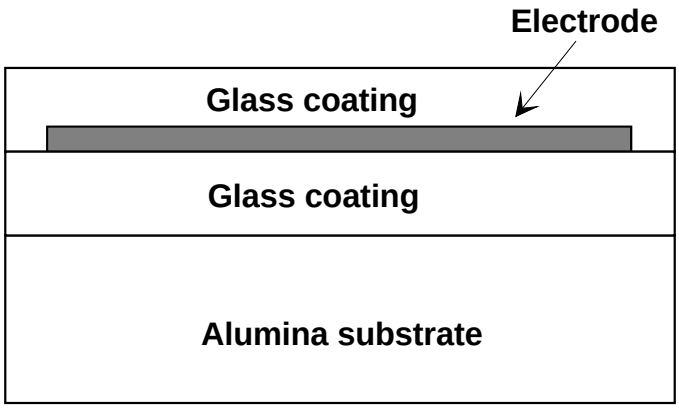

Figure 6.13. Schematic of the three-layer coating structure on the alumina substrate used for the fabrication of ceramic electrostatic chucks.

Alumina substrates with pre-machined through-holes were used as the base substrate. The glass was converted into slurry form following the same procedure described in Chapter 3. The slurry was cast on the substrate with a doctor blade and allowed to dry in air. Excess material was trimmed off and the through-holes cleared of the dried slurry. Grooves were carved out of the dried layer and the electrode paste was screen printed on the glass. The through-holes were also filled with the paste. The coatings were sintered at 900°C for 3 hours in air using a firing schedule similar to that for the glass-ceramic on Mo chuck. The through-holes intended for electrical connection to the backside of the substrate were refilled with the electrode paste before the final or top layer of glass was cast on the sintered coating. The through-hole for the cooling gas

was cleared of the dried slurry and the top layer was sintered at 900°C for 3 hours using the same firing profile.

Chucks made using the procedure above are shown in Figure 6.14. The smaller devices are 4 inches in diameter while the larger chuck is 6 inches in diameter. The dark areas have embedded Ag-Pd electrodes from the printed metal paste. The orthogonal strips running across the diameter contain grooves through which cooling gas can flow from the inlet in the center of the disk. The electrical connectors are mounted in the back either as a cofired metal bump or metallized surface, and, if necessary, a metal wire such as silver is run through the via hole, which can be cofired with the structure. A schematic of the cross-sectional structure can be seen in Figure 6.15. Note how the glass dielectric coatings completely seal the Ag-Pd electrode to prevent any arcing when a voltage is applied either in a monopolar or dipolar configuration. The glass layers are reduced to a thickness of around 125 μm (5 mil) each after firing, which can be reduced by polishing to increase the chucking strength. The electrode had a fired thickness of 12 to 25 μm (0.5 to 1 mil).

Figure 6.14. Glass-coated alumina electrostatic chucks. The dark areas contain the embedded Ag-Pd electrode.

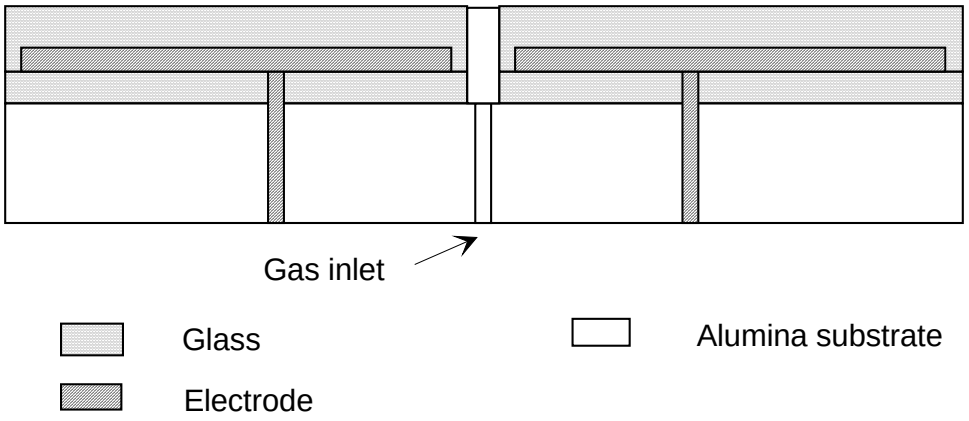

Figure 6.15. Schematic of the cross-section of the ceramic chuck design showing the various materials present.

6.2 Ceramic Plate Heaters

Another application of the sintering of constrained films that has commercial importance is for making ceramic heaters. Ceramic heaters have components that can withstand higher temperatures than metal heaters and are not susceptible to oxidizing atmospheres such that they make better heaters for higher temperatures and harsh environments than metal heaters. In a ceramic heater, a resistive pattern is applied to the substrate and isolated with an overglaze of glass. The ceramic substrate can provide a more uniform temperature over a large area.

To demonstrate the concept, a ceramic heater with an alumina substrate was fabricated. Other substrates may also be used such as aluminum nitride or beryllium oxide if high thermal conductivity is desired, although BeO may not be desirable because of its toxicity. The materials requirements necessary to successfully make the structure are similar to those of the electrostatic chucks. The CTE of the glass coating(s) must be close enough to that of the substrate to prevent the formation of a camber. For example, although the cordierite-base glass ceramic adheres very well to alumina, its low CTE causes a visually observable camber. The firing temperature of the glass must also be compatible with the resistor material and must be tolerant of the sintering atmosphere necessary to prevent oxidation of the resistor metal or alloy, if one is needed.

The prototype was constructed out of the same material as the ceramic chuck in the previous section. Instead of a wide-area electrode print, a narrow serpentine pattern was deposited to form the resistor. Silver-palladium was used as the electrode but other conductive materials that can be cofired with the glass should work as well. A plate heater fabricated through this method is shown in Figure 6.16. The open holes do not have a function in this design although they may be used as portholes for a thermocouple, if desired. The layered structure is illustrated in Figure 6.17 and, except for the discrete electrodes, looks similar to the ceramic chuck. The back surface may be used as the heated surface for additional temperature uniformity.

Figure 6.16. Ceramic plate heater with an alumina substrate, SCE-5 glass dielectric layers and Ag-Pd alloy for the resistor pattern.

Figure 6.17. Layered structure of the ceramic plate heater showing the dielectric and metal layers that were successively fired on the alumina substrate.

A similar process is used to make commercial ceramic heaters such as those manufactured by Watlow (Watlow Electric Manufacturing Co., St. Louis, MO, http://www.watlow.com). In the process, layers of a glass, resistor and glazing are successively fired on the substrate, as illustrated in Figure 6.18, to obtain the functional structure. The process resembles the technique that was developed for making the chuck and ceramic heater previously discussed above.

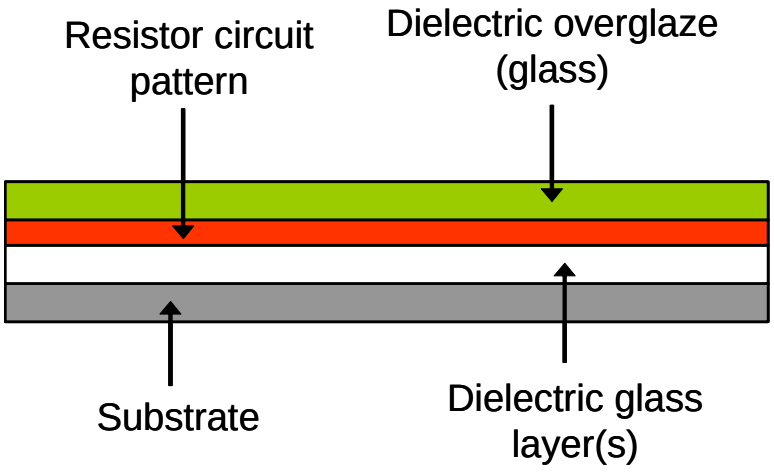

Figure 6.18. Layering scheme used for fabricating the commercial ceramic heater.

Chapter 7
Conclusions

The study on the densification behavior of constrained films of zinc oxide and cordierite-base crystallizable glass showed an unmistakable difference in the response to constraint between the two. The densification of zinc oxide was significantly reduced by the substrate constraint with the calculated activation energies of densification, indicating different densification mechanisms operating for the same range of relative densities. The crystallizable glass was not significantly affected by the substrate constraint and the calculated activation energy for densification indicated that the dominant mechanism was still by viscous flow. Except for the rise in the in-plane stress towards the end of the 950°C sintering cycle in the glass, the in-plane stresses in the constrained ZnO films were much higher than in the corresponding glass-ceramic films, which was consistent with other observations. The densification of constrained films by sintering was successfully applied to the fabrication of devices and articles such as glass and glass-ceramic coated electrostatic chucks and ceramic heaters. These conclusions are further elaborated below.

7.1 Sintering of Zinc Oxide on Rigid Substrate

Zinc oxide films were isothermally sintered at temperatures between 900°C and 1050°C and the results showed that the densification of films constrained on substrates is severely reduced compared to the freestanding film. The microstructure evolution was also affected by the constrained. The freestanding film had a structure with equiaxed grains joined by wide grain boundaries whereas the constrained film consisted of particles joined together by narrower necks that resulted in a more open structure. The densification mechanisms were affected by the constraint based on the calculated activation energies of densification. For the density range of 60 to 64%, apparent

activation energy is 242 ± 21 kJ/mole for the freestanding film while the constrained film had an activation energy of 391 ± 34 kJ/mole, indicating that the dominant densification mechanism was different for each condition, grain boundary diffusion for the freestanding film and lattice diffusion for the constrained film. Significant levels of in-plane stresses, up to around 800 kPa, were observed during the sintering of the constrained films. Yielding of the film, in which either the stress dropped slight or remained unchanged, was observed at relative densities below 60%, which could be explained as the result of particle rearrangement to reduce the stress. The yielding phenomenon persisted to higher densities at higher sintering temperatures. After yielding, the stress climbed linearly with increasing density with a maximum increase of 800 kPa observed at 1050°C before gradually relaxing and retaining a substantial amount of the stress after cooling.

7.2 Sintering of Crystallizable Glass on Rigid Substrate

Constrained films of the cordierite-base crystallizable glass (glass-ceramic) were sintered between 900°C and 1000°C and the densification curves indicate that the substrate constraint did not have a significant effect on the densification except perhaps at very high densities. The free and constrained sintering curves were similar until the constrained film underwent expansion. Calculations of the densification activation energy showed that, on average, it was close to the activation energy of 1077 kJ/mole that was obtained from the annealing and softening points of the glass, indicating that the prevailing densification mechanism was still by viscous flow. Film expansion was observed during sintering and was traced to the formation of pores at the interface with the silicon substrate. It was significantly reduced when the silicon substrate was oxidized at 900 to 950°C before it was coated with the glass-ceramic slurry, leading to the conclusion that the pore formation at the silicon substrate interface was due poor wetting, which in turn was caused by the loss of the thin native oxide layer through a reaction with the glass.

7.3 Recommendations for Future Work

The effect of substrate constraint on the densification of crystalline ceramic and crystallizable glass was investigated and a clear difference was observed. It would be interesting to apply the same techniques to study a system that densifies by liquid phase sintering. Although the materials system is crystalline or remains crystalline after sintering, a liquid phase is available to facilitate matter transport. The addition of a non-sintering component such as particle inclusions will also be an interesting phenomenon to study both for scientific and practical reasons as it can provide a framework for synthesizing materials such as powder composites for various applications.

The manufacture and utilization of nanomaterials have become hot topics. Extending the study on the effect on constraint to nanoscale powders of metals, glasses and ceramics would be an interesting area of research with practical implications on the use of these materials in various applications such as in microelectronics and composites. Specifically, it could provide the answer to the question of whether or not the observed effect of constraint on sintering of submicron to micron-range powders will apply to the nanosize materials.

In the sintering of ZnO, prolonged binder burnout caused an annealing effect that reduced the driving force for sintering and rendered the porous films more difficult to sinter to high density. When conducting sintering studies on submicron and nanoscale crystalline powder, it would be advisable to take steps to minimize this occurrence. Steps that could be taken include reducing the binder burnout time to the shortest time necessary and making use of a binder system more appropriate for the process.

The glass-ceramic that was studied had very high densification rates at temperatures at temperature more than 25°C above the softening point that only a narrow density range falls within the isothermal stage. Sintering at a temperature interval narrower, e.g. at 10 or 15°C intervals, than what was used here should give more densification curves where a sufficient range of densities are attained within the isothermal stage of sintering, thus providing more data to include in the analysis.

References

1 R. R. Tummala and E. J. Rymaszewski, Microelectronics Packaging - An Overview in *Microelectronics Packaging Handbook*, edited by R. R. Tummala and E. J. Rymaszewski (New York: Van Nostrand Reinhold, 1989).

2 T. J. Garino and H. K. Bowen, "Kinetics of Constrained-Film Sintering," *Journal of the American Ceramic Society*, Vol. 73, No. 2 (1990), pp. 251-257.

3 J. Bang and G.-Q. Lu, "Densification Kinetics of Glass Films Constrained on Rigid Substrates," *Journal of Materials Research*, Vol. 10, No. 5 (1995), pp. 1321-1326.

4 J. Choe, J. N. Calata, and G.-Q. Lu, "Constrained-film Sintering of a Gold Circuit Paste," *Journal of Materials Research*, Vol. 10, No. 4 (1995), pp. 986-994.

5 G.-Q. Lu, R. C. Sutterlin, and T. K. Gupta, "Effect of Mismatched Sintering Kinetics on Camber in a Low-Temperature Cofired Ceramic Package," *Journal of the American Ceramic Society*, Vol. 76, No. 8 (1993), pp. 1907-1913.

6 R. K. Bordia and G. W. Scherer, Sintering of Composites: A Critique of the Available Analyses in *Ceramic Transactions: Ceramic Powder Science II*, edited by G. L. Messing, E. R. Fuller, Jr., and H. Hausner (Westerville, Ohio: American Ceramic Society, 1988), Vol. 1, pp. 872-886.

7 *Ceramic Processing Before Firing*, edited by G. Y. Onoda and L. L. Hench (New York: Wiley, 1978).

8 J. S. Reed, *Principles of Ceramic Processing*, 2nd ed (New York: Wiley & Sons, 1995).

9 R. R. Tummala, Ceramic Packaging in *Microelectronics Packaging Handbook*, edited by R. R. Tummala and E. J. Rymaszewski (New York: Van Nostrand Reinhold, 1989).

10 *Handbook of Thick Film Technology*, edited by P. J. Holmes and R. G. Loasby (Ayr: Electrochemical Publications, 1976).

11 R. C. Sutterlin, G.-Q. Lu, and T. K. Gupta, Cosintering of Gold/LTCC Substrates:Development of Camber and Via Defects in *Ceramic Transactions: Materials in Microelectronic and Optoelectronic Packaging*, edited by H. C. Ling, K. Niwa, and V. N. Shukla (Westerville, Ohio: American Ceramic Society, 1993), Vol. 33, pp. 435-444.

12 R. K. Bordia and G. W. Scherer, "On Constrained Sintering - II. Comparison of Constitutive Models," *Acta Metallurgica*, Vol. 36, No. 9 (1988), pp. 2399-2409.

13 T. K. Gupta, "Application of Zinc Oxide Varistors," *Journal of the American Ceramic Society*, Vol. 73 (1990), pp. 1817-1840.

14 *Ceramic Transactions: Advances in Varistor Technology*, edited by L. M. Levinson (Westerville, Ohio: American Ceramic Society, 1988), Vol. 3.

15 W. D. Kingery, H. K. Bowen, and D. R. Uhlmann, *Introduction to Ceramics* (New York: Wiley-Interscience, 1976).

16 *Sintering and Related Phenomena*, edited by G. C. Kucynski, N. A. Hooten, and C. F. Gibson (New York: Gordon and Breach, 1967).

17 M. F. Yan, Solid State Sintering in *Engineered Materials Handbook* (Materials Park, Ohio: ASM International, 1991), Vol. 4, pp. 270-284.

18 M. F. Yan, Sintering of Ceramics and Metals in *Advances in Powder Technology*, edited by G. Y. Chin (Metals Park, Ohio: ASM, 1982).

19 D. W. Richerson, *Modern Ceramic Engineering: Properties, Processing and Use in Design*, 2nd ed. rev. and expanded (New York: Marcel Dekker, 1992).

20 G. W. Scherer, Constitutive Models for Viscous Sintering in *Mechanics of Granular Materials and Powder Systems*, edited by M. M. Mehrabadi (New York: ASME, 1992), Vol. 37, pp. 1-18.

21 M. N. Rahaman, *Ceramic Processing and Sintering*, 2nd ed (New York: Marcel Dekker, 2003).

22 O.-H. Kwon, Liquid Phase Sintering in *Engineered Materials Handbook* (Materials Park, Ohio: ASM International, 1991), Vol. 4, pp. 285-303.

23 R. M. German, *Liquid Phase Sintering* (New York: Plenum Press, 1985).

24 R. M. German, Fundamentals of Sintering in *Engineered Materials Handbook* (Materials Park, Ohio: ASM International, 1991), Vol. 4.

25 C. Herring, "Effect of Change of Scale on Sintering Phenomena," *Journal of Applied Physics*, Vol. 21 (1950), pp. 301-303.

26 W. D. Kingery and M. Berg, "Study of the Initial Stages of Sintering Solids by Viscous Flow, Evaporation-Condensation, and Self-Diffusion," *Journal of Applied Physics*, Vol. 26 (1955), pp. 1205-1212.

27 G. C. Kuczynski, "Self-diffusion in Sintering of Metallic Particles," *Transactions of the American Institute of Mining, Metallurgical and Petroleum Engineers*, Vol. 185, No. 2 (1949), pp. 169-178.

28 R. L. Coble, "Initial Sintering of Alumina and Hematite," *Journal of the American Ceramic Society*, Vol. 41 (1958), pp. 55-62.

29 D. L. Johnson and I. B. Cutler, "Diffusion Sintering. I. Initial Stage Sintering Models and their Application to Shrinkage of Powder Compacts," *Journal of the American Ceramic Society*, Vol. 46, No. 11 (1963), pp. 541-545.

30 J. Frenkel, *J. Phys. (Moscow)*, Vol. 9, No. 5 (1945), pp. 385.

31 R. L. Coble, "Sintering of Crystalline Solids. I. Intermediate and Final State Diffusion Models," *Journal of Applied Physics*, Vol. 32 (1961), pp. 787-792.

32 D. L. Johnson, *Journal of the American Ceramic Society*, Vol. 53 (1970), pp. 574.

33 W. Beere, "Unifying Theory of the Stability of Penetrating Liquid Phases and Sintering Pores," *Acta Metallurgica*, Vol. 23, No. 1 (1975), pp. 131-138.

34 G. W. Scherer, "Sintering of Low-Density Glasses: I. Theory," *Journal of the American Ceramic Society*, Vol. 60, No. 5-6 (1977), pp. 236-239.

35 R. L. Coble, Mechanisms of Densification During Hot Pressing in *Sintering and Related Phenomena*, edited by G. C. Kuczynski, N. A. Hooten, and C. F. Gibson (New York: Gordon and Breach, 1967), pp. 329-350.

36 R. L. Coble, *Journal of Applied Physics*, Vol. 41 (1970), pp. 4798.

37 J. K. Mackenzie and R. Shuttleworth, "A Phenomenological Theory of Sintering," *Proceedings of the Royal Society (London)*, Vol. 62, No. 12-B (1949), pp. 833-852.

38 C. H. Hsueh, A. G. Evans, R. M. Cannon et al., "Viscoelastic Stresses and Sintering Damage in Heterogeneous Powder Compacts," *Acta Metallurgica*, Vol. 34 (1986), pp. 927-936.

39 M. N. Rahaman, L. C. De Jonghe, and R. J. Brook, "Effect of Shear Stress on Sintering," *Journal of the American Ceramic Society*, Vol. 69, No. 1 (1986), pp. 53-58.

40 K. R. Venkatachari and R. Raj, "Shear Deformation and Densification of Powder Compacts," *Journal of the American Ceramic Society*, Vol. 69, No. 6 (1986), pp. 499-506.

41 J. D. Hansen, R. P. Rusin, M. H. Teng et al., "Combined-stage Sintering Model," *Journal of the American Ceramic Society*, Vol. 75, No. 5 (1992), pp. 1129-1135.

42 W. D. Kingery, in *Kinetics of High Temperature Process*, edited by W. D. Kingery (New York: Technology Press of MIT and J. Wiley & Sons, 1958).

43 R. Raj, "Analysis of the Sintering Pressure," *Journal of the American Ceramic Society*, Vol. 70, No. 9 (1987), pp. C-210-C-211.

44 R. K. Bordia and A. Jagota, "Crack Growth and Damage in Constrained Sintering Films," *Journal of the American Ceramic Society*, Vol. 76, No. 10 (1993), pp. 2475-2485.

45 R. M. Christensen, *Theory of Viscoelasticity, An Introduction*, 2nd ed (New York: Academic Press, 1982).

46 G. W. Scherer, *Relaxation in Glasses and Composites* (New York: Wiley-Interscience, 1986).

47 R. K. Bordia and G. W. Scherer, "On Constrained Sintering. I. Constitutive Model for a Sintering Body," *Acta Metallurgica*, Vol. 36, No. 6 (1988), pp. 2393-2397.

48 G. W. Scherer, "Sintering Inhomogeneous Glasses: Application of Optical Waveguides," *Journal of Non-crystalline Solids*, Vol. 34, No. 2 (1979), pp. 239-256.

49 G. W. Scherer and T. J. Garino, "Viscous Sintering on a Rigid Substrate," *Journal of the American Ceramic Society*, Vol. 68, No. (1985), pp. 216-220.

50 G. W. Scherer, "Sintering with Rigid Inclusions," *Journal of the American Ceramic Society*, Vol. 70, No. 10 (1987), pp. 719-725.

51 G.-Q. Lu, G. B. Kromann, B. Mogilevsky et al., "Evaluation of Die-attach Adhesives by Curvature Measurements," *Third Intersociety Conference on Thermal Phenomena in Electronic Systems (I-THERM III)* (1992), pp. 155-158.

52 A. Witvrouw and F. Spaepen, "Determination of the plane stress elastic constants of thin films from substrate curvature measurements: Applications to amorphous metals," *Journal of Applied Physics*, Vol. 73, No. 11 (1993), pp. 7344-7350.

53 J. Bang and G.-Q. Lu, "Constrained-Film Sintering of a Borosilicate Glass: *In situ* Measurement of Film Stresses," *Journal of the American Ceramic Society*, Vol. 78, No. 3 (1995), pp. 813-815.

54 M. Ohring, *The Materials Science of Thin Films* (San Diego: Academic Press, 1992).

55 C. G. Bergeron and S. H. Risbud, *Introduction to Phase Equilibrium in Ceramics* (Columbus, OH: American Ceramic Society, 1984).

56 S. H. Knickerbocker, A. H. Kumar, and L. W. Herron, "Cordierite Glass-Ceramics for Multilayer Ceramic Packaging," *American Ceramic Society Bulletin*, Vol. 72, No. 1 (1993), pp. 90-95.

57 P. Fernandez, N. de Diego, J. del Rio et al., "A positron study of sintering processes in ZnO-based ceramics," *Journal of Physics: Condensed Matter*, Vol. 1 (1989), pp. 4853-4858.

58 J. Choe, "Constrained Sintering of Gold Circuit Films on Rigid Substrates." MS Thesis, Virginia Polytechnic Institute and State University, 1994.

59 O. Sudre and F. F. Lange, "Effect of Inclusions on Densification: I, Microstructural Development in an Al_2O_3 Matrix Containing a High Volume Fraction of ZrO_2 Inclusions," *Journal of the American Ceramic Society*, Vol. 75, No. 3 (1992), pp. 519-524.

60 O. Sudre, G. Bao, B. Fan et al., "Effect of Inclusions on Densification: II, Numerical Model," *Journal of the American Ceramic Society*, Vol. 75, No. 3 (1992), pp. 525-531.

61 L. C. De Jonghe, M. N. Rahaman, and C. H. Hsueh, "Transient Stresses in Bimodal Compacts During Sintering," *Acta Metallurgica*, Vol. 34, No. 7 (1986), pp. 1467-1471.

62 R. K. Bordia, "Sintering of TiO_2-Al_2O_3 Composites: A Model Experimental Investigation," *Journal of the American Ceramic Society,* Vol. 71, No. 4 (1988), pp. 302-310.

63 C. P. Ostertag, "Technique for Measuring Stresses Which Occur During Sintering of a Fiber-Reinforced Ceramic Composite," *Journal of the American Ceramic Society,* Vol. 70, No. 12 (1987), pp. C355-C357.

64 O. Sudre and F. F. Lange, "The Effect of Inclusions on Densification: III, The Desintering Phenomenon," *Journal of the American Ceramic Society,* Vol. 75, No. 12 (1992), pp. 3241.

65 L. P. Martin and M. Rosen, "Constant heating-rate analysis of densification kinetics in sintering zinc oxide," *Journal of Materials Synthesis and Processing,* Vol. 4, No. 6 (1996), pp. 371-375.

66 L. Perazolli, J. A. Varela, and E. Longo, "Coarsening kinetics of ZnO during constant heating rate sintering," *Science of Sintering,* Vol. 28, No. 2 (1996), pp. 85-90.

67 L. Perazolli, E. Longo, and J. A. Varela, presented at the Sintering Technology, University Park, PA, 1995.

68 T. K. Gupta and R. L. Coble, "Sintering of zinc oxide. I. Densification and grain growth," *Journal of the American Ceramic Society,* Vol. 51, No. 9 (1968), pp. 521-525.

69 N. Ono, K. Kitamura, K. Nakajima et al., "Measurement of Young's Modulus of Silicon Single Crystal at High Temperature and its Dependency on Boron Concentration Using the Flexural Vibration Method," *Japanese Journal of Applied Physics,* Vol. 39, No. 2A (2000), pp. 368-371.

70 H. Over, O. Knotek, and E. Lugscheider, "Elastische Eigenschaften von einkristallinem Silicium in Abhangigkeit von der Temperatur und der Versetzungsdichte," *Z. Metallkde.,* Vol. 73, No. 9 (1982), pp. 552.

71 J. Bang, "Sintering of Glass Films on Rigid Substrates Studied by Optical Techniques." Ph. D. Dissertation, Virginia Polytechnic Institute and State University, 1996.

72 S. R. Scholes, *Modern Glass Practice*, 7th rev. ed. ed (Boston: Cahners Books, 1975).

73 R. Zallen, *The Physics of Amorphous Solids* (New York: Wiley, 1983).

74 J. Bang, G.-Q. Lu, and J. N. Calata, "Determination of shear viscosity of borosilicate glass + silica powder compacts by an optical system," *Journal of Materials Research*, Vol. 14, No. 3 (1999), pp. 1062-1068.

75 L. L. Hench and J. K. West, *Principles of Electronic Ceramics* (New York: Wiley, 1990).

76 A. J. Moulson and J. M. Herbert, *Electroceramics: Materials, Properties, Applications* (London: Chapman and Hall, 1990).

77 M. Nakasuji and H. Shimizu, "Low voltage and high speed operating electrostatic wafer chuck," *Journal of Vacuum Science and Technology A*, Vol. 10, No. 6 (1992), pp. 3573-3578.

78 Sematech, *Electrostatic Chuck Tutorial, Technology Transfer Number 93031533A-GEN* (Sematech, Inc., 1993).

79 L. D. Hartsough, "Electrostatic Wafer Holding," *Solid State Technology*, Vol. 36, No. 1 (1993), pp. 87-90.

80 J. Field, "Electrostatic wafer clamping for next-generation manufacturing," *Solid State Technology*, Vol. 37, No. 9 (1994), pp. 91-98.

81 J.-F. Daviet, L. Peccoud, and F. Mondon, "Electrostatic Clamping Applied to Semiconductor Plasma Processing, I. Theoretical Modeling," *Journal of the Electrochemical Society*, Vol. 140, No. 11 (1993), pp. 3245-3255.

82 G. Partridge, C. A. Elyard, and M. I. Budd, Glass-ceramics in substrate applications in *Glasses and Glass-ceramics*, edited by M. H. Lewis (London; New York: Chapman and Hall, 1989), pp. 226-271.

83 N. V. Parthasaradhy, *Practical Electroplating Handbook* (New Jersey: Prentice Hall, 1989).

84 W. H. Safranek, *The Properties of Electrodeposited Metals and Alloys* (New York: Elsevier, 1974).

Appendix A
Borosilicate Glass-Coated Stainless Steel Electrostatic Chucks

Electrostatic chucks (ESC) are important components in semiconductor wafer processing equipment. Using electrostatic force to hold wafers during processing reduces reduce wafer bowing and contamination problems which are common in mechanical wafer-handling systems. This study was done to demonstrate the feasibility of using tape casting method and sintering to fabricate borosilicate glass-coated stainless steel chucks for low-temperature applications. The fired glass coatings on the substrates ranged from 100 μm to 150 μm thick. The adhesion of the coating was excellent such that it was able to withstand moderate drop tests and temperature cycling to over 300^{o}C without cracking or peeling off. The electrostatic clamping force generally followed the theoretical voltage-squared curve, except at elevated temperatures when deviations were observed at higher applied voltages. The results indicate that this is a viable technique for manufacturing low-cost electrostatic wafer chucks.

Introduction

Electrostatic wafer clamping is an improvement over mechanical clamping devices used in semiconductor processing equipment. A mechanical chuck holds the wafer in place through a clamping ring around the wafer periphery[1,2]. This allows non-reactive gas to be introduced under pressure between the wafer and susceptor for efficient cooling. However, mechanical clamps produce uneven force distribution that causes the wafer to bow, leading to non-uniform temperature distribution and lower heat dissipation. Electrostatic chucks (ESC) do not suffer from this limitation since the

electrostatic force is distributed uniformly over the chuck area covered by the electrode, which for practical purposes may be considered to be the entire chuck surface.

An electrostatic chuck has an advantage over a mechanical system mainly because of the absence of moving parts. In its simplest form, it consists of an electrically insulating layer covering an electrically conductive substrate. The elimination of mechanical parts such as the clamping ring minimizes particle contamination while increasing the available wafer area. The applied clamping force is sufficiently high to prevent bowing of the wafer and can even be used to flatten bowed wafers. Increased contact with the chuck surface also provides uniform heat transfer over the entire wafer area. While numerous variations in the design exist, electrostatic chucks can be classified into three basic configurations, namely: the monopolar, bipolar, and Johnsen-Rahbek (J-R)[1,3]. The monopolar configuration is the simplest and is similar to a parallel plate capacitor, with the wafer acting as the second electrode. The plasma over the wafer serves as a conductor to complete the electrical circuit. Theoretically, it also produces the largest clamping force among the three types. For other applications, variants of the bipolar design are better suited because they do not require the presence of the plasma in order to function. Because of its simple design, the monopolar design was selected for the chucks that were fabricated in this study.

The research was conducted to demonstrate the feasibility of fabricating electrostatic chucks using glass coatings on metal. Glasses have lower firing temperatures than materials such as alumina and silica. The fabrication method borrows heavily from the tape casting process that is used in the production of microelectronics packaging substrates and multilayer ceramic capacitors, which is already a mature technology[4-6].

Experimental Procedure

The insulating layer of the electrostatic chucks consisted of a sodium borosilicate glass (BSG) obtained from Sem-Com Co., Inc. (Toledo, OH) with a softening point of 710^{o}C. The substrates were made of austenitic stainless steel. The glass has a lower

coefficient of thermal expansion (CTE), 5.6 x 10^{-6}/C, than the steel (about 11 x 10^{-6}/C), such that it will be under compression at any temperature below the firing temperature. The slurry was prepared from the glass powder using a two-stage milling procedure[4,5]. In the first stage, the powder was mixed with fish oil and solvents and milled for 24 hours. In the second stage, the polyvinyl butyral (PVB) binder and plasticizer were added and the slurry was milled for an additional 24 hours. The slurry was de-aired and cast on the substrates using an adjustable casting knife (doctor blade) to form dried green films roughly 150 to 250 μm thick. The coatings were allowed to dry in air for 24 hours before trimming of excess material. The dried coatings had an initial relative density of 60% of the theoretical density of 2.32. The stainless steel substrates were pre-oxidized above 500^{o}C before being coated with the glass slurry to improve adhesion. The BSG-coated substrates were fired in air at 710^{o}C for 3 hours after binder burnout at 500^{o}C. The fired coatings were polished with diamond paste to improve the flatness of the chuck and eliminate the surface roughness. The coating of the test chuck had a thickness of 125 μm after final polishing with 1 μm diamond paste.

Clamping force measurements were obtained using a custom-built vacuum chamber with a disk heater and a load cell attached to a motor-driven micrometer screw as shown in Fig. 1. The glass-coated substrate was mounted directly on the disk heater with a hollow screw to accommodate a thermocouple, which is inserted into the substrate through the screw hole such that the tip is as close as possible to the dielectric layer. The metal substrate served as the bottom electrode and a rigid alumina plate that was electroless-plated with a thin layer of copper served as the top electrode. A machinable ceramic rod attached to the load cell linked to the top electrode through loose joint enabled the electrode to achieve maximum contact with the chuck surface while serving to electrically isolate the electrode from the body of the chamber. The voltage was applied to the top electrode as shown schematically and the data acquisition was done through attached to the system. The electrode was lowered onto the chuck and charged at the set voltage for 5 minutes before it was slowly lifted to break it free from the chuck.

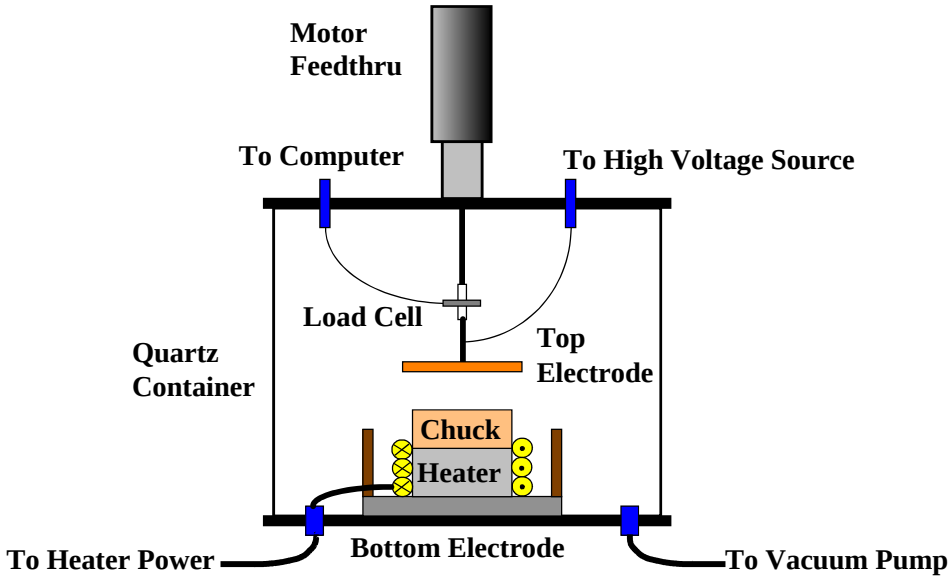

Figure 1. Schematic diagram of the apparatus for clamping force measurement.

Results and Discussion

The adhesion of the glass coating on the substrate is essential to the reliability and life of the electrostatic chuck, which was the reason that the stainless steel substrate was pre-oxidized. A more detailed discussion of the mechanism involved is described elsewhere[7]. For stainless steel, the native oxide layer provides a chemical bond that maintains the continuity of the electronic and atomic structure across the interface. This approach will not work if the oxide layer is only weakly bonded to the base metal. In stainless steel, the chromium on the surface is readily oxidized to form an adherent layer, although an added pre-oxidation seemed to enhance adhesion. Excessive oxidation is not desirable either, as was observed along the edges of the coating, which resulted in weaker adhesion. This can be remedied by switching to a non-oxidizing atmosphere during the sintering stage.

Clamping force measurements were obtained at room temperature, 100^{o}C and 150^{o}C at applied voltages up to 550^{o}C. The results, plotted as clamping pressure, are shown in Fig. 2. The superimposed dashed lines are non-linear least square fits based on

a more realistic model[8,9] that includes an air gap between the electrode and the insulating layer. The model is represented by an equation of the form

$$P = \frac{\varepsilon_o V^2}{2\left(\frac{h_d}{k} + h_{gap}\right)^2} \quad (1)$$

where P is the clamping pressure and V is the applied voltage. ε_o is the permittivity of a vacuum; k is the relative dielectric constant of the coating; h_d and h_{gap} are the coating thickness and airgap, respectively. For the room temperature measurements, the clamping pressure closely followed the V^2 relationship as predicted by Eq. (1). The average airgap obtained by curve-fitting ranged from about 1.3 μm at room temperature to 2.5 at 150°C. The increase in the airgap with increasing temperature, roughly 1 μm/100°C, was caused by the relatively large CTE mismatch between the glass and the substrate. Measurements obtained at higher temperatures revealed some interesting results. At 100°C, the clamping pressure was consistently higher than at room temperature for all voltages. This trend is similar to the results obtained from glass-ceramic coatings on metal substrates[10], which was attributed to increased flatness of the dielectric and higher dielectric constant at elevated temperature. However, in this instance, the insulating layer was already polished flat such that the increase can only be accounted for in Eq. (1) by an increase in the dielectric constant. The data also followed the pressure-voltage relationship although it started to deviate at 300 volts. At 150°C, the trend was reversed and the clamping pressure was lower than at 100°C, although still clearly higher than at room temperature. The deviation was also distinct above 250 volts and moved quickly towards the room temperature curve. The deviation may be due to increased leakage current at higher temperature and applied voltage as the electrical resistivity drops. Insufficient charging time, although not very likely, is also a possibility under such conditions. The resistivity of the glass drops below 10^{10} ohm-cm at 150°C and below 10^8 ohm-cm at 200°C, as shown in Fig. 3, such that its useful operating temperature should be no higher than 200°C. Replacement of the glass with a high-expansion and zero or low-alkali composition should increase the useful temperature range.

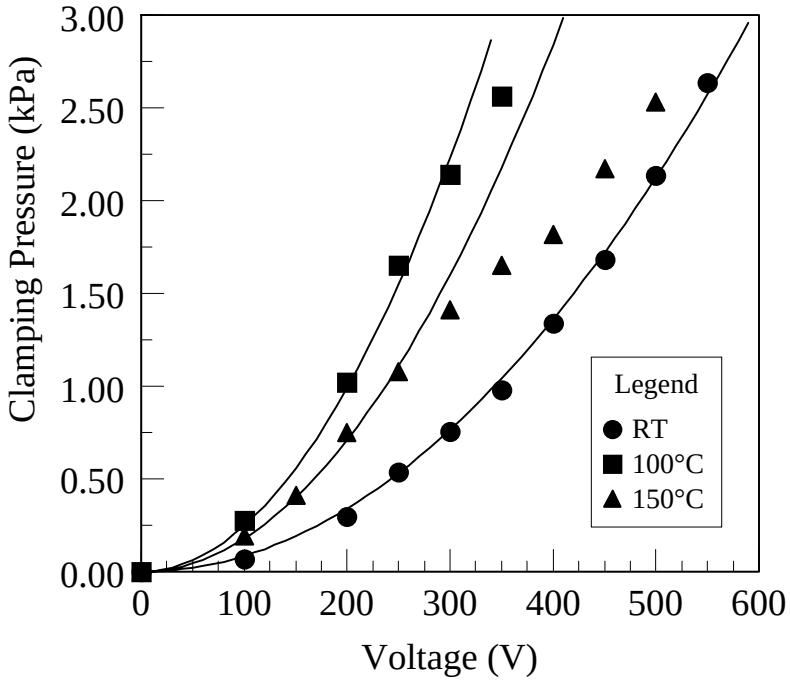

Figure 2. Clamping pressure of borosilicate glass/stainless steel chuck at various temperatures.

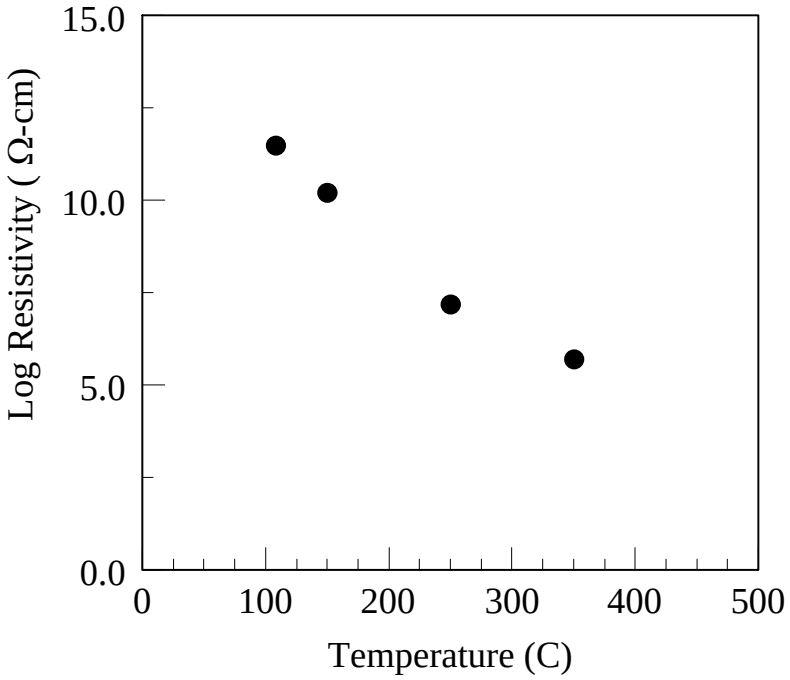

Figure 3. Electrical resistivity of the borosilicate glass coating.

Conclusion

Electrostatic chucks were successfully produced by casting glass slurry on stainless steel substrates and sintering at a temperature at 710°C. The clamping force tests showed that the chuck has a maximum operating temperature of around 200^{o}C, making it suitable for low temperature chucking applications. Measurements showed an overall increase in clamping pressure as the temperature is increased, which may be due to increased surface flatness and dielectric constant. Deviations from the clamping pressure-applied voltage relationship were observed above room temperature at higher applied voltages and may be the result of increased leakage current due to decreasing resistivity of the insulating layer.

Acknowledgment

This project was funded by Triad Investors Corp.and was also partially supported by the National Science Foundation, under the Faculty Early Career Development (CAREER) program, DMR-9502326.

References

1 J. Field, “Electrostatic wafer clamping for next-generation manufacturing,” *Solid State Technology*, 91-98 Sept. 1994.

2 J.-F. Daviet, L. Peccoud and F. Mondon, “Electrostatic Clamping Applied to Semiconductor Plasma Process I. Theoretical Modeling,” *J. Electrochem. Soc.* **140**, 3245-3255 (1993).

3 L. D. Hartsough, “Electrostatic Wafer Holding,” *Solid State Technology*, 87-90, Jan. 1993.

4 J S. Reed, *Principles of Ceramic Processing*, 2nd ed. Wiley, New York, 1978.

5 G. Y. Onoda and L. L. Hench (eds.), *Ceramic Processing Before Firing*, Wiley, New York, 1978.

6 R. R. Tummala, Ceramic Packaging, in *Microelectronics Packaging Handbook*, (R. R. Tummala and E. J. Rymaszewski, eds.), Van Nostrand Reinhold, New York 1989.

7 G. Partridge, C. A. Elyard, and M. I. Budd, Glass-ceramics in substrate applications, in *Glasses and Glass-Ceramics*, edited by M. H. Lewis (Chapman and Hall, London 1989) Chapter 7.

8 M. Nakasuji and H. Shimizu, "Low voltage and high speed operating electrostatic wafer chuck," *J. Vac. Sci. Technol*. A **10** [6] 3573-3578 (1992).

9 Sematech, *Electrostatic Chuck Tutorial, Technology Transfer Number 93031533A-GEN*, Sematech, Inc., 1993.

10 G-Q. Lu, J. N. Calata, J. Bang, T. Kuhr, A. Amith, *Final Project Report to Triad Investors Corp*., 1997.

Appendix B
Multifunctional Ferroelectric-Ferrite Nanocomposite Material for Integrated Passive Components

Ferroelectric-ferrite nanocomposite material was synthesized from sol-gel derived barium titanate mixed with nanosize nickel zinc ferrite powder. The barium titanate had a Ba/Ti ratio of 1/0.975 and LiF was added at 2% of the $BaTiO_3$ as sintering aid. The nanocomposite contained around 45 to 50 volume percent of the ferrite nanopowder. Unlike a nanocomposite with stoichiometric $BaTiO_3$ (Ba/Ti ratio of 1) and without LiF, it can be sintered to high density below 1000°C. The material contained both $BaTiO_3$ and ferrite phases after firing, as indicated by x-ray diffraction (XRD) and as observed by transmission electron microscopy (TEM). The fired nanocomposite exhibited high dielectric constant (around 250 to 300) and the Curie temperature was apparently shifted to near room temperature. Magnetic property measurements in a superconducting quantum interference device (SQUID) showed that the magnetization (1.1 to 1.2 x 10^5 A/m) is dependent on the volume fraction of the NiZn ferrite in the nanocomposite, It can be cofired with Ag metal conductor with no apparent detrimental effect on the densification of the material and the integrity of the fired structure. Details of the process and results are discussed in the following sections.

Introduction

Passive components tend to occupy large amounts of space resulting in packages and modules. One way to reduce the overall size is to integrate or embed these components into the package substrate to free up space on the substrate for the active

devices. In addition, if materials that are simultaneously useful for making capacitive and inductive components were available, these devices can be constructed in the same space or volume, thus further reducing the physical size of these components. Multifunctional materials in the form of ferroelectric-ferrite composites are now being used to manufacture devices such as EMI filters wherein the composite is made by firing powder mixtures of barium titanate and ferrite [1-4]. The usual method of making these materials is by mixing powders of dielectric and magnetic components, e.g., barium titanate and ferrite, to form a composite that exhibits relatively high dielectric constant and permeability. With the proper electrode configuration, the material is fired to a temperature sufficient to attain high relative density without extensive reaction between the two components. However, because the firing temperatures of the components tend to be high, above 1000°C, inexpensive metals such as silver and copper are not suitable conductor materials, unless sintering aid is added to lower the firing temperature significantly.

An alternative approach would be to use "nanomaterials" and their corresponding processing techniques to synthesize multi-functional composites out of dielectric and magnetic materials. Novel structures with enhanced properties and functionalities can be developed through such technologies. By utilizing nanomaterials, functional properties can be incorporated in the material in the form of distinct components in the nanocomposite. Materials with nanometer-size particles normally require lower processing temperature thus reducing potentially adverse reactions between components of a composite. Colloidal chemistry also allows for more uniform and intimate mixing of the individual components.

In this research, barium titanate was synthesized from precursors by a sol-gel processing technique [5,6]. The goal was to isolate the ferrite nanoparticles, that were added at a later stage, and produce a uniform dispersion of them in a $BaTiO_3$ matrix. Lowering the sintering temperature of the resulting mixture can be achieved by the addition of a sintering aid to densify the colloidal $BaTiO_3$ precursor. It has been shown that adding LiF to a non-stoichiometric composition with excess barium can significantly reduce the sintering temperature of barium titanate to well below 1000°C [7,8]. The low-temperature densification is attributed to the formation of a low-melting temperature

phase that facilitates the transport of ions to fill in the pores instead of the slower high-temperature solid state diffusion processes.

The main objective of the research is to synthesize a multifunctional ferroelectric-ferrite composite with nanoscale structural features using colloidal processing techniques and nanometer size particles to take advantage of unique properties not available in larger scale structures. The desired microstructure of the composite material consists of nanometer size particles of the ceramic ferrite phase coated with or embedded in a matrix of the dielectric phase. Isolation of the ferrite particles will prevent their growth, thus minimizing losses due to domain wall rotation, and keep the electrical resistivity high. Such composite was expected to have a densification temperature below 1000°C and thus be compatibility with existing metallization materials and packaging processes. It should be available in powder form making it suitable for conversion into paste or tape form.

Experimental Method

Nanocomposite Powder Preparation

The nanocomposite powder was composed of $BaTiO_3$ and NiZn ferrite ($Ni_{0.5}Zn_{0.5}Fe_2O_4$) nanometer sized particles. The $BaTiO_3$ was produced in solution by sol-gel while the NiZn ferrite was added as an off the shelf nanopowder (NanoProducts Corp., Longmont, CO 80504). For the preparation of $BaTiO_3$ by sol-gel, anhydrous $Ba(OH)_2$ with 94-98% purity (Alfa Aesar) was dissolved with methanol-methoxyethanol solvent (60-40) in an inert atmosphere. The solution was stirred for at least one hour before titanium isopropoxide (97%) (Alfa Aesar) was added. The solution was further stirred for at least one hour before being mixed with a suspension of NiZn ferrite nanopowder in methanol-methoxyethanol. The mixture was further agitated in an ultrasonic chilled water bath to enhance the mixing and dispersion of the components. Deionized water was then added and the mixture stirred to distribute the water. Agitation was stopped before the solution started to gelate, which happens a few minutes after adding the water, and the suspension was set aside undisturbed for up to 5 days to allow

hydrolysis and condensation to proceed [6]. The suspension was heated in a water bath at around 90°C to evaporate the solvent.

Samples with stoichiometric and nonstoichiometric $BaTiO_3$ were prepared. For the stoichiometric $BaTiO_3$, $Ba(OH)_2$ and Ti isopropoxide were added at a proportion of 0.62:1 by weight to achieve a Ba:Ti ratio of 1. The $BaTiO_3$ precursor concentration in solution was around 0.1 M with the water to Ba molar ratio equal to 100. The NiZn ferrite content in the dried mixture was estimated to be between 45 to 50 volume percent.

The nonstochiometric $BaTiO_3$ had a Ba/Ti ratio of around 1/0.975. The $Ba(OH)_2$ to Ti isopropoxide proportion was adjusted to 0.638 by weight to obtain this ratio. The molar concentration of the $BaTiO_3$, water to Ba ratio, and ferrite volume fraction remained the same. Lithium fluoride (LiF) was added to the suspension before completely drying at a dosage of 2 weight percent of the $BaTiO_3$ to serve as the sintering aid.

Sintering and Characterization

The resulting composite powders were pressed into pellets and fired in air from 3 to 6 hours at temperatures of 800 to 1200°C for the samples without LiF and from 800 to 1000°C for the samples with the LiF to determine sinterability. Green powder and fired powder, along with the fired pellets were analyzed by x-ray diffraction (XRD) to verify the formation of the barium titanate phase and to check for any potential reaction between the barium titanate and ferrite after firing. Powder samples were observed by transmission electron microscopy (TEM) and were prepared by dropping and drying dilute suspensions of the powders on the TEM grids. Samples for dielectric characterization were made by cofiring silver paste on both surfaces of pellets with the nonstoichiometric $BaTiO_3$ pre-fired at 950°C for 6 hours. This temperature was chosen as the firing temperature for the samples because it produced sufficiently dense pellets while still below the melting temperature of silver, which was used later on as the buried metallization in the cofiring tests. Magnetic property characterization was done in a liquid helium-cooled SQUID instrument (Quantum Design MPMS XL). Cofiring tests with metal conductors were done by embedding partially sintered preforms from nanoscale silver paste in nanocomposite powder pressed at 60 to 100 MPa (10 to 15 ksi). The paste was prepared by mixing 30 nm silver powder with binder and thinner to obtain

a uniformly dispersed mixture. The silver preforms were cut from the partially sintered silver sheet with a thickness of 70 to 100 µm. The silver sheets were made by stencil printing several layers and fired at 300°C.

Results and Discussion

Synthesis of Nanocomposite Material

Barium ethoxide was initially used as the source of Ba for the $BaTiO_3$ component to successfully synthesize the compound. However, $Ba(OH)_2$ was found to be equally suitable as a precursor and was used in all subsequent mixtures [9]. The ferrite nanopowder suspension was mixed into the $BaTiO_3$ precursor solution before it started to set and allowed to age for at least 5 days after which the solvent was evaporated by heating at 90°C. The resulting powder was ground by hand using a glass mortar and pestle. Portions of the powder were heated at various temperatures to determine whether $BaTiO_3$ would form and to find out if the two components would react. Previous tests using powders of both materials showed little reaction when heated up to around 1000°C but there was a possibility that this new mixture could be more reactive. X-ray diffraction patterns taken of the green and fired powder samples of stoichiometric $BaTiO_3$ + ferrite are shown in Figure 1. The green powder produced the characteristic NiZn ferrite peaks but not the barium titanate. However, upon heating, the peaks started to show up, even at 600°C (not shown in figure), the lowest firing temperature tested. The peaks also became stronger with increasing temperature indicating more conversion to the crystalline phase. The peaks are particularly prominent up to 1000°C but seem to have deteriorated at 1200°C with some new peaks beginning to appear, a possible indication of increased reaction between the component phases.

TEM observation of the green powder showed the presence of the two distinct components. In Figure 2, the dark particles correspond to the ferrite while the lighter particles are made of the $BaTiO_3$ precursors. They are initially irregularly shaped and mostly encapsulate the ferrite particles. Under beam illumination, the $BaTiO_3$ particles

exhibited sensitivity to heating by transforming into faceted structures, possibly undergoing *in situ* crystallization.

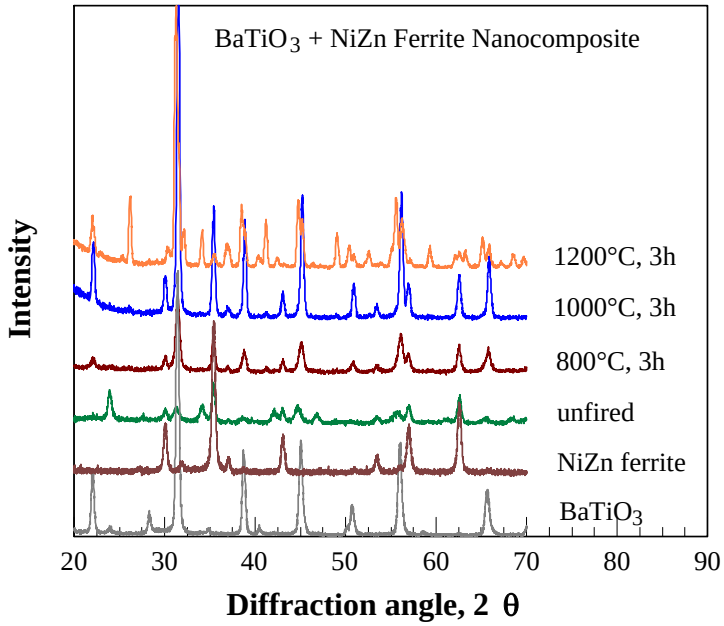

Figure 1. X-ray diffraction patterns from stoichiometric $BaTiO_3$ + NiZn ferrite at various firing temperatures.

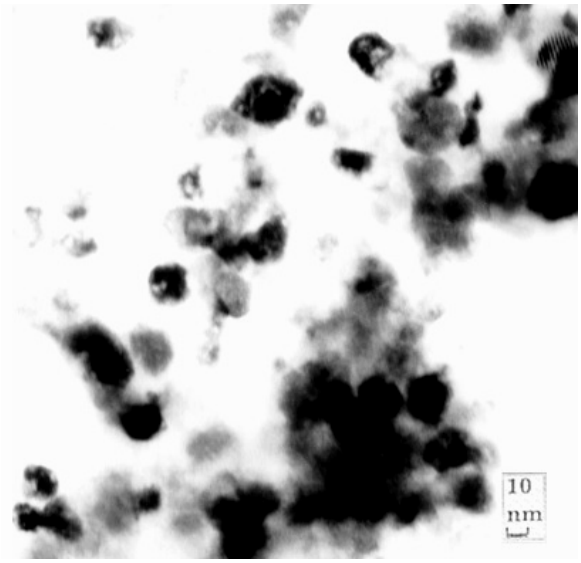

Figure 2. TEM image of green off-stoichiometric sol-gel $BaTiO_3$ + NiZn ferrite composite powder. Light particulates are $BaTiO_3$ and dark particulates are NiZn ferrite.

Sintering of Nanocomposite Powder Compacts

Nanocomposite powder with the stoichiometric $BaTiO_3$ was pressed into 12.5 mm (0.5 inch) pellets and sintered in air at temperatures ranging from 800 to 1200°C for up to 6 hours to determine the temperature at which significant shrinkage, and hence high density, could be achieved. The results are shown in Figure 3. At 900°C, the linear shrinkage was less than 5 % corresponding to a volume shrinkage of 11%. Given an estimated relative green density close to 60%, this is less than 70% of theoretical density. Significant shrinkage could only be attained at 1100°C where a linear shrinkage of 13 to 14% was observed (~35 % equivalent volume shrinkage) for a fired density greater than 90%. Near theoretical density was possible at 1200°C where a volume shrinkage of around 40% was obtained. The nanoscale particle size of the sol-gel-derived $BaTiO_3$ precursor in the mixture was expected to have helped to lower the sintering temperature. However, it is believed that the presence of large amounts of the ferrite nanoparticles, far in excess of the critical volume fraction for percolation for 3-D systems of 0.16 [10], retarded the densification process [11] and essentially nullified any such advantages. This composite, as formulated, depends on solid state diffusion processes to densify [12], and achieving high density under moderate temperatures would be extremely difficult at best.

A solution around the problem was to switch to a different sintering mechanism, specifically liquid phase sintering [13], through the addition of a sintering aid as discussed previously [6-7]. The liquid phase forms at a much lower temperature than the typical sintering temperature of the material being fired. Under the right conditions, the liquid can provide a path for rapid transport and therefore rapid sintering. Following this approach, nanocomposite powder with a modified Ba/Ti ratio and LiF was made and sintered under similar conditions to the previous samples. The results of the sintering of these pellets in air are plotted in Figure 4. Comparing both linear and volume shrinkages to those in Figure 3, it is evident that a substantial drop in the sintering temperature was achieved. At 900°C, a linear shrinkage of around 13% and corresponding volume shrinkage of 35% was obtained, which is equivalent to at least 90% density. The linear shrinkage alone is around 3 times that of what was obtained from the composite without

sintering aid. Increasing the temperature further yields a diminishing return with the density gradually approaching the theoretical density. If silver is to be cofired with the material as the internal metallization, a practical limit is 950°C.

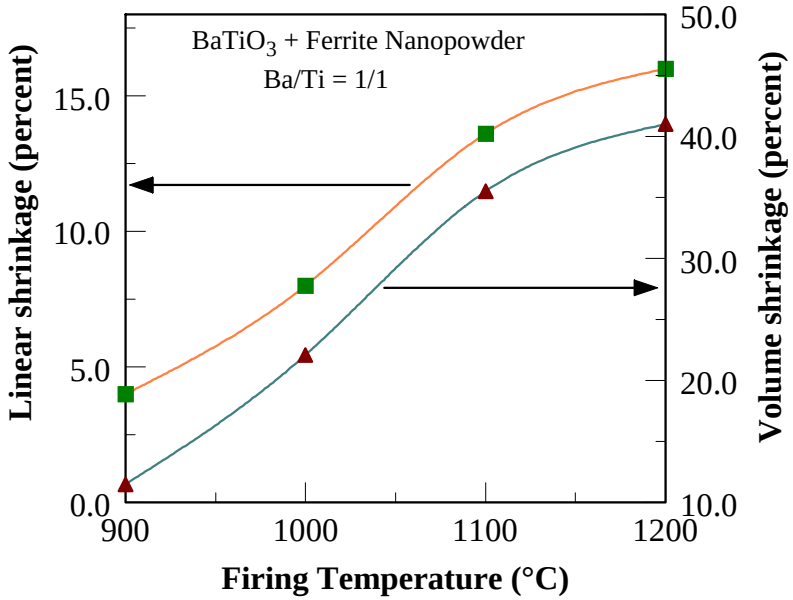

Figure 3. Linear and volume shrinkages of stoichiometric $BaTiO_3$ + NiZn ferrite nanocomposite sintered at various temperatures for 6 hours.

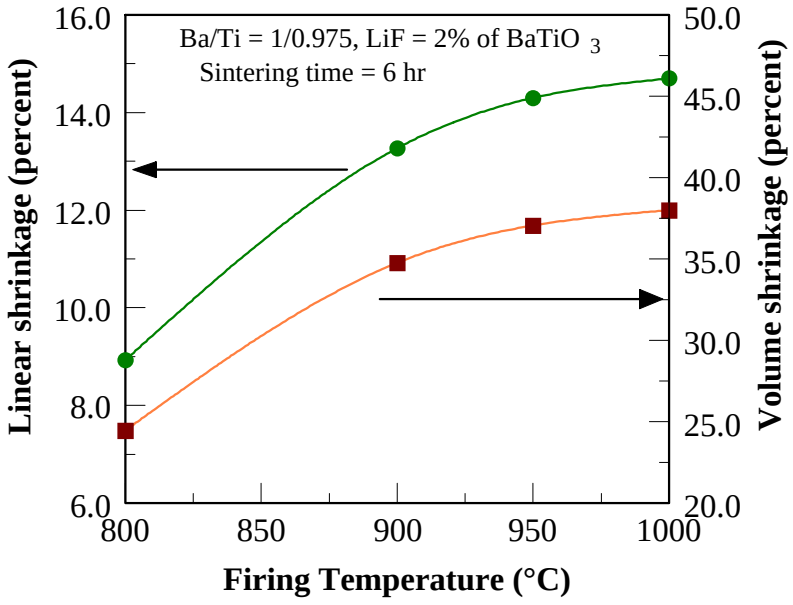

Figure 4. Linear and volume shrinkages of $BaTiO_3$ + NiZn ferrite with a Ba/Ti ratio of 1/0.975 and 2 % LiF (of $BaTiO_3$ content).

Changing the stoichiometry of the $BaTiO_3$ and adding LiF to the composite did not appear to be detrimental to the formation of crystalline $BaTiO_3$ and the retention of the ferrite structure. The XRD patterns in Figure 5 show the presence of the ferrite component at all temperatures. The $BaTiO_3$ peaks, as in the previous case, appeared after heating with the intensity becoming stronger with increasing firing temperature.

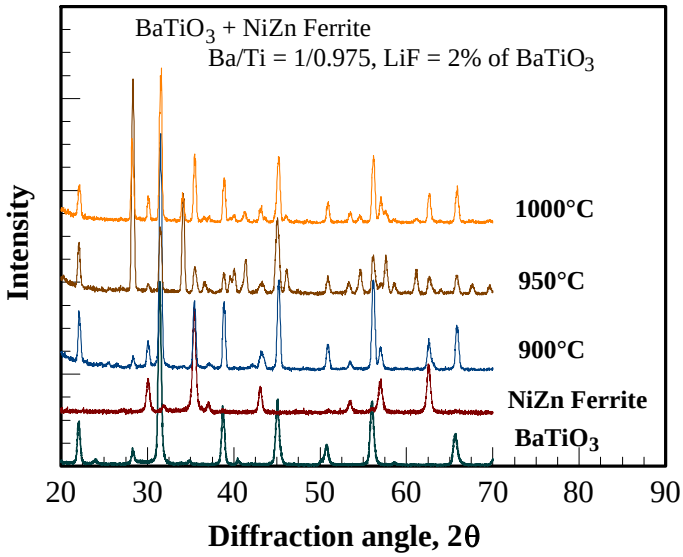

Figure 5. X-ray diffraction patterns of non-stoichiometric $BaTiO_3$ + ferrite nanocomposite powder compacts containing LiF fired at different temperatures.

Dielectric and Magnetic Characterization

The room temperature dielectric constant (κ) and loss tangent (tan δ) of the nanocomposite for a range of frequencies is shown in Figure 6. The dielectric constant is about 300 but exhibits some frequency dispersion resulting in a gradual drop with increasing frequency. This is substantially lower than the dielectric constant of a ceramic $BaTiO_3$ which is in the thousands depending on the grain/crystal size [14]. There could be several reasons for the lower value. To begin with, the material contained only 50 - 55 volume percent barium titanate. The firing temperature may not have been sufficiently high to completely transform the $BaTiO_3$ from the cubic, lower κ phase to the higher-κ tetragonal phase. The extremely small particle size of the starting colloid

(nanoscale), pinned by the presence of a large amount of ferrite particles may have made the formation of larger grains during firing difficult, thus keeping the grains in the highly stressed cubic structure. The unrelieved stress during cooling with the ceramic grain size well below 1 μm could have reached values where the tetragonality is suppressed and the permittivity decreases. In spite of all that, the dielectric constant still compared favorably to a polycrystalline thin film with the tetragonal structure 370 [15].

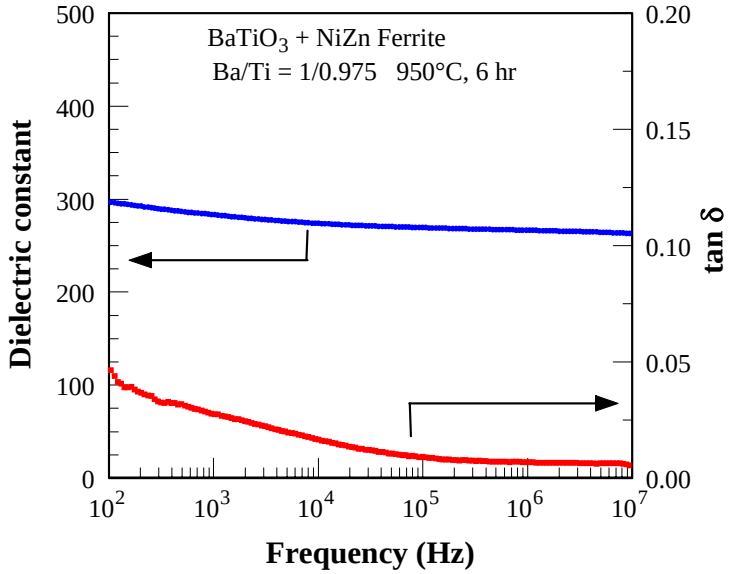

Figure 6. Room temperature dielectric constant and loss tangent of the nanocomposite with LiF sintered at 950°C for 6 hours.

The dielectric constant of the sintered nanocomposite at various temperatures is shown in Figure 7. There are several features in the plotted curves worth noting, other than the values of the dielectric constant. In a typical $BaTiO_3$ ceramic, a Curie peak occurs at around 120°C. Two other smaller peaks occur at 10°C and –80°C. These peaks correspond to transitions in the structure from cubic to tetragonal, orthorhombic and rhombohedral, respectively, just like in a single crystal. However, with the nanocomposite, a peak occurs at around 20 to 25°C but none at 120°C. The Curie peak was either completely eliminated or shifted down to around 20°C. Certain additions are known to completely destroy the Curie peak such as Nb along with Co, Mg, Ni or Mn, tantalum, and small amounts of iron oxide [16], the latter being the only additive that could be present in the material due to the ferrite. These additions inhibit crystal growth.

On the other hand, some non-isovalent substituents can depress the Curie point to varying degrees [17]. They include Ni^{+2}, Zn^{+2} and Fe^{+3}, all components of the ferrite phase. Ni^{+2} and Zn^{+2} have a marked effect on the Curie point while Fe^{+3} has an intermediate effect. They depress the other peaks as well (10°C and –80°C) which could explain the absence of the other peaks in their expected locations.

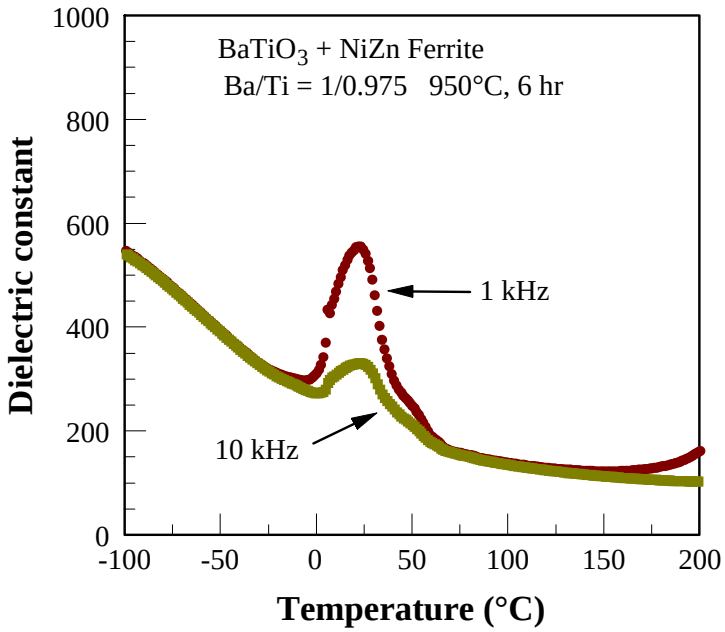

Figure 7. Dielectric constant of the sintered nanocomposite versus temperature.

Plotted in Figure 8 is the room temperature volume magnetization (M) of the nanocomposite which was fired at 950°C for 6 hours. The saturation magnetization is 1.1 to 1.2 x 10^5 A/m (110-120 emu/cm^3) which occurs at an applied field of around 1.2 x 10^5 A/m (1500 Oe). This is roughly half of the magnetization in the pure NiZn ferrite, which was found to be around 2.3 to 2.35 x 10^5 A/m (230 - 235 emu/cm^3) at a comparable applied field using the same apparatus. The pure ferrite was sintered at 1200°C in air for 6 hours to attain high density. This means that the magnetization of the nanocomposite is dependent on the volume fraction of the ferrite component. It also implies that there was no extensive reaction between the two components, which could have destroyed the ferrite structure responsible for the measured magnetic moment. The relative permeability of the nanocomposite was estimated from AC susceptibility measurements to be around 7. This value is rather low but so is the pure ferrite judging from the magnetization curve in Figure 9. Replacement of the NiZn ferrite with another

composition chemically adjusted for higher permeability should yield a nanocomposite material with better permeability than the test material(s) used in this study.

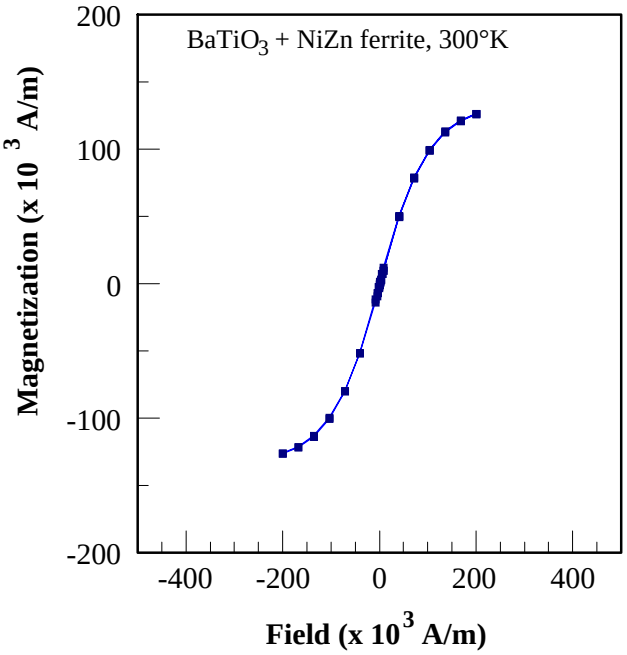

Figure 8. Magnetization of the fired $BaTiO_3$ + NiZn ferrite nanocomposite at 300°K.

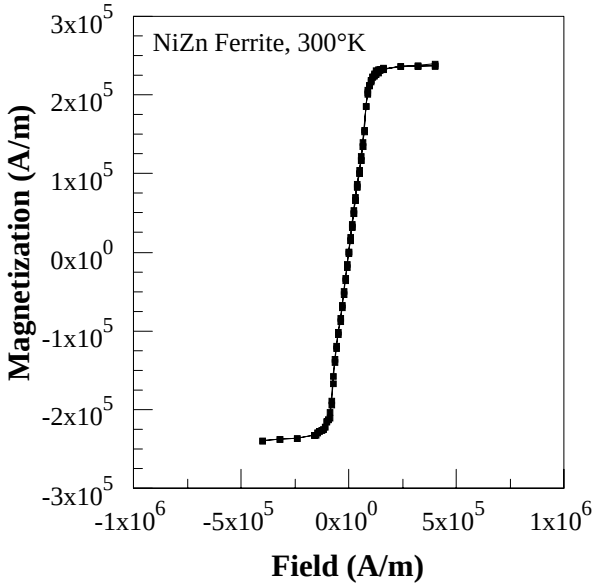

Figure 9. Room temperature (300°K) magnetization curve of the pure NiZn ferrite fired at 1200°C.

Cofiring with Silver

While the nanocomposite can be sintered to high density under 1000°C, it is equally important that it can be cofired with metal conductors if it is to be used in passive components and other applications requiring some form of metal pattern. There are several issues that have to be dealt with when cofiring layers of different materials into a single structure [18]. Embedded or printed metal should not react chemically with the surrounding material, as this will reduce the effective cross section of the metal while also reducing the effective thickness of the adjacent layers. This is particularly important in structures such as those of capacitors. Occasionally, some interface reaction may be beneficial to improve the adhesion between the component materials. Another concern relates to the mechanical integrity of the cofired structure. Differential shrinkage, different sintering temperatures and coefficient of thermal expansion (CTE) mismatch can lead to defects and distortions.

To test the cofirability with silver, partially sintered silver was made by repeated printing of nanometer-size particle silver paste on a carrier substrate to form thick films. The dried films were heated to 300°C to drive off the binder and sintered to gain sufficient strength to withstand handling and cutting into the desired patterns. The partial sintering process leads to an estimated relative density of 80 %. The films were then cut into the desired strip or rectangular patterns and embedded in the nanocomposite powder. The powder containing the metal patterns was pressed into pellets at a pressure of 12 to 15 ksi (80 to100 MPa) in a 1-inch diameter mold. The pellets were fired at temperatures ranging from 900°C to 950°C. Embedded metal patterns included strips of 2 mm to 2.5 mm width and rectangular films at least 1 cm wide. Some of the fired pellets with embedded silver are shown in Figure 10. Except for some distortion due to differential shrinkage, there was no apparent detrimental effect on the densification and on the integrity of the embedded silver patterns.

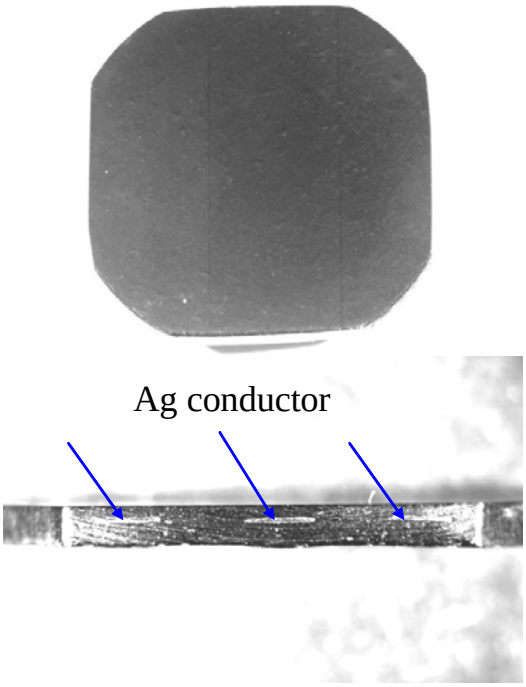

Figure 10. Sintered nanocomposite pellets with Ag metal conductors embedded by cofiring. The lower image is a cross section exposing the embedded metal conductor strips.

Conclusions

Ferroelectric-ferrite nanocomposite was synthesized from sol-gel barium titanate and NiZn ferrite nanopowder. The nanocomposite, with the addition of LiF and adjustment of the Ba/Ti ratio to 1/0.975, can be sintered to high density below 1000°C making it cofirable with silver. TEM images of the unfired powder showed the presence of two distinct components with the sol-gel $BaTiO_3$ coating most of the ferrite nanoparticles. After sintering, the barium titanate precursor transformed to the crystalline state as revealed by x-ray diffraction which also indicates little reaction with the ferrite nanoparticles. The dielectric constant of fired nanocomposite was 300, which gradually decreased with increasing frequency. The nanocomposite material exhibited a magnetization (1.1 to 1.2 x 10^5 A/m) roughly half of the magnetization of the pure ferrite (2.3 to 2.35 x 10^5 A/m), indicating a dependence on the volume fraction of the ferrite

component in the composite. This material can be cofired with embedded silver conductor patterns below the melting temperature of silver. There was no apparent detrimental effect on the densification of the nanocomposite (e.g. reduced sintered density), and on the mechanical integrity of the fired structure. The technique used to synthesize the nanocomposite should be applicable to other $BaTiO_3$-based ferroelectric-ferrite compositions with enhanced dielectric and magnetic properties compared to those of the test system used in this study, thus making the composite potentially more suitable for a variety of applications.

Acknowledgments

This work was supported primarily by the ERC Program of the National Science Foundation under Award Number EEC-9731677. The author would like to thank Li Yan for helping with the XRD measurements, Hu Cao for assistance with the dielectric and SQUID measurements, Dr. Gordon Yee for the use of the SQUID apparatus, Thomas Lei and Steve McCartney for their assistance with the TEM and John Bai for providing the nanosilver thick film preforms.

References

1 C. M. Callewaert, J. V. Mantese, A. L. Micheli, N. Schubring, D. A. Messuri, W. T. Phillips, S. A. Musick, "Distributed-Element Multipole EMI Filters: Material and Design Considerations," *Compliance Engineering*, Sept/Oct 2000.

2 J. V. Mantese, et al., "Applicability of Effective Medium Theory to Ferroelectric/Ferrite Composition and Frequency-Dependent Complex Permittivities and Permeabilities," *Journal of Applied Physics*, **79** (3) (1996), pp. 1655-1660.

3 G. W. Milton, D. J. Eyre, and J. V. Mantese, “Finite Frequency Range Kramers Kronig Relations: Bounds on the Dispersion,” *Physical Review Letters* **79** (1997), pp. 3062.

4 T. Y. Yamamoto et al. “Evaluation of Ferroelectric/Ferromagnetic Composite by Micro-composite Designing,” Ferroelectrics **95** (1989), 175.

5 C. J. Brinker and G. W. Scherer, *Sol-Gel Science: The Physics and Chemistry of Sol-Gel Processing*, Boston: Academic Press, 1990.

6 M. Kuwabara, K. Miki, S. Takahashi, and H. Shimooka, “Preparation of monolithic barium titanate xerogels by sol-gel processing and the dielectric properties of their sintered bodies,” *Appl. Phys. Lett.* **66** (13), (1995) pp. 1704-1706.

7 J. M. Haussonne, G. Desgardin, Ph. Bajolet, and B. Raveau, “ Barium Titanate Perovskite Sintered with Lithium Fluoride,” *J. Am. Ceram. Soc*., **66** (11) (1983), pp. 801-807.

8 D. A. Tolino, J. B. Blum, “Effect of Ba:Ti Ratio on Densification of LiF-Fluxed $BaTiO_3$,” *J. Am. Ceram. Soc.*, **68** [11] (1985) C-292-C-294.

9 C. Lemoine, B. Gilbert, B. Michaux, J-P. Pirard, and A. J. Lecloux, “Synthesis of barium titanate by the sol-gel process,” *Journal of Non-Crystalline Solids*, **175** (1) (1994) pp. 1-13.

10 H. Scher and R. Zallen, “Critical density in percolation processes,” *J. Chem. Phys.* **53** (9), 3759 (1970)

11 M.N. Rahaman, *Ceramic Processing and Sintering*, 2nd ed., New York: Marcel Dekker, 2003, pp. 702-723.

12 W.D. Kingery, H.K. Bowen, and D.R. Uhlmann, *Introduction to Ceramics*, 2nd ed., New York: John Wiley & Sons, 1976.

13 R. M. German, *Liquid Phase Sintering* , New York: Plenum Press, 1985.

14 J. Herbert, *Ceramic Dielectrics and Capacitors, Vol. 6*, New York: Gordon and Breach, 1985, Ch. 5.

15 H. B. Sharma and A. Mansingh, “Phase transition in sol-gel derived barium titanate thin films,” *J. Phys. D: Appl. Phys.* **31** (1998) pp. 1527-1533.

16 H. I. Oshry, Barium Titanate Capacitor. U.S. Pat. No. 2,695,239 (1954).

17 H. Ihrig, “The phase stability of $BaTiO_3$ as a function of doped 3d elements,” *J. Phys. C: Solid State*, **11** (1978), pp. 819-827.

18 M. N. Rahaman, *Ceramic Processing and Sintering*, 2nd ed., New York: Marcel Dekker, 2003, pp. 723-733.

Vita

Jesus N. Calata Tel: (540) 231-8423 (Office)
(540) 552-8643 (Home)
1507 Poplar Ridge Cir Email: jcalata@vt.edu
Blacksburg VA 24060

Education

- B. S. Metallurgical Engineering, *cum laude*, 1983, University of the Philippines Diliman, Quezon City, Philippines
- M. S. Metallurgical Engineering, 1989,University of the Philippines Diliman, Quezon City, Philippines
- Ph.D. Student, Materials Science and Engineering, Virginia Polytechnic Institute and State University, Blacksburg VA

Work Experience

- Faculty member, Department of Mining and Metallurgical Engineering, College of Engineering, University of the Philippines Diliman, Quezon City, Philippines, 1985 – 1992)
- Graduate research assistant, Department of Materials Science and Engineering, Virginia Polytechnic Institute and State University, Blacksburg Virginia, 1996 – Present

Research and Related Accomplishments

- Study of the densification behavior of ceramic and glass-ceramic powder coatings and films constrained on rigid substrates using optical techniques
- Electroless deposition of copper metal stripes inside alumina tubes for possible use in particle accelerator assemblies
- Development of and fabrication of glass/metal and glass-ceramic/metal electrostatic wafer chucks for semiconductor processing with moderate to high-temperature capability

- Development processing technique for fabricating glass-ceramic/ceramic and glass/ceramic electrostatic chuck with high-temperature capability and with potential application to ceramic heaters
- Investigated the use of fired metal paste/powder as joining material for glass, ceramic and metal components
- Developed an apparatus for lining inner tube walls with glass slurry to provide abrasion and chemically resistant coatings (Patent granted)
- Investigated the processing and fabrication of insulated substrates for use as electronics packaging substrates with integrated heat sink
- Investigated the feasibility of cofiring silver-palladium with low-temperature firing zinc oxide formulations in order to produce commercially viable zinc oxide varistors
- Assisted in the design and fabrication of mock-up structures of proposed packaging for large-area micro-mirror array for the next generation space telescope
- Investigated the comparative reliability of wire and ribbon bond, solder ball and area solder interconnections for power semiconductor packaging application
- Synthesize nanoscale ferroelectric-ferrite composite material for integrated passive components using the sol-gel process

Awards, Patents and Professional Activities

- Member, International Microelectronics and Packaging Society (IMAPS)
- Member, Materials Research Society
- Member, Virginia Academy of Science
- Member, American Society of Mechanical Engineers
- Joint Member, ACerS, ASM, TMS
- Department of Science and Technology (DOST) Undergraduate Scholarship Award, Philippines, 1978-83
- Japan Society for the Promotion of Science (JSPS) Exchange Scientist Program, March 1990, Tokyo Institute of Technology
- DOST – Engineering and Science Education Program (ESEP) Fellowship, 1992-96
- U.S. Patent No. 5855676, “Tube Lining Apparatus”, Inventors: Guo-Quan Lu, Jesus N. Calata, January. 5, 1999.

- Refereed papers for Metallurgical and Materials Transactions and Intersociety Conference on Thermal and Thermomechanical Phenomena in Electronic Systems (ITHERM)

Journal and Conference Publications

1. Jesus Noel Calata, Allen Matthys, Guo-Quan Lu, "Constrained-film sintering of cordierite glass-ceramic on silicon substrate," *J. Mater. Res.* **13** (8) 2334-2340 (1998).
2. Jesus Noel Calata, Sihua Wen, Guo-Quan Lu, "Densification and crystallization kinetics of cordierite glass-ceramic coatings on rigid substrates," *Mater. Res. Soc. Symp. Proc.* **481** 483-488 (1998).
3. Jesus Noel Calata, Sihua Wen and Guo-Quan Lu, "Borosilicate glass-coated stainless steel electrostatic chucks for wafer handling system," Dielectric Ceramic Materials, *Ceram. Trans*. 100 517-523 (1999).
4. Jesus Noel Calata, Guo-Quan Lu, and Tze-Jer Chuang, "Constrained sintering of glass,glass-ceramic and ceramic coatings on metal substrates," *Surf. Interface Anal*, **31**, (7), 673-681 (2001) (Special Issue)
5. Guo-Quan Lu, Jesus Noel Calata, "Adhesion strength of cordierite glass-ceramic coatings on molybdenum substrates," *J.Mater.Res.* **15** (12) 2857-13 (2000).
6. Jesus Noel Calata, Guo-Quan Lu, Christoph Luechinger, "Evaluation of Interconnect Technologies for Power Semiconductor Devices," *Proc. CPES Power Electronics Seminar*, Blacksburg Virginia, 96-105, April 2002.
7. JoonWon Choe, Jesus Noel Calata, Guo-Quan Lu, "Constrained-film sintering of a gold circuit paste," *J. Mater. Res.* **10** (4)986-994 (1995).
8. G-Q. Lu, J.C. Bang, J.N. Calata, and J.W. Choe, "Densification Behavior of Thick Metal and Ceramic Films," *Ceram. Trans.* **53**, 121-135 (1995).
9.. Jaecheol Bang, Guo-Quan Lu, Jesus Noel Calata, "Determination of shear viscosity of borosilicate glass + silica powder compacts by an optical system," *J. Mater. Res.* **14** (3) 1062-1068 (1999).
10. Xingsheng Liu, Jesus N. Calata, Jinggang Wang, Guo-Quan Lu, "The Packaging of IPEM Using Flip Chip Technology," *Proc. 17th Annual VPEC Seminar, Blacksburg, Virginia*, 361-367, September 1999.

11. Xingsheng Liu, Jesus Noel Calata, Houyun Liang, Wangzhou Shi, Xuanyin Lin, Kuixun Lin, and G.G. Qin, "Photoluminescence and Photoluminescence Excitation Mechanisms for Porous Silicon and Silicon Oxynitride," *Mater. Res. Soc. Symp. Proc.* 588 141-148 (1999).
12. G-Q. Lu, J. Calata, S. Wen, S. Dutta, Y. Zheng, C. Stahl, and P. Shu, "Packaging of Large-Area, Individually Addressable, Micro-mirror Arrays for the Next Generation Space Telescope," *Proceedings of International Conference on Microfabrication, Integration, and Packaging of MEMS*, France, May, 2002
13. Jesus Noel Calata, Guo-Quan Lu, and Christoph Luechinger, "Evaluation of Interconnect Technologies for Power Semiconductor Devices" *Proc. ITHERM 2002*, May 29-June 1, 2002.
14. Jesus Noel Calata, John G. Bai, Guo-Quan Lu, Christoph Luechinger, "Evaluation of the Reliability of Interconnect Technologies for Power Semiconductor Devices," *Proc. CPES Power Electronics Seminar*, 172-181, April 2003.
15. G-Q. Lu, X. Liu, S. Wen, J. N. Calata, J. G. Bai, "Strategies for Improving Reliability of Solder Joints on Power Semiconductor Devices," in Proceedings of ASME International Mechanical Engineering Congress and Exposition (IMECE), November 16-21, 2003; Soldering and Surface Mount Technology, Vol.16, No. 2, 27-40 (2004).
16. Zhiye (Zach) Zhang, Jesus Noel Calata, Carlos Suchicital, Guo-Quan Lu and D.P.H. Hasselman, "Comparison of the Thermal Interfacial Resistance Contribution from Silver and Solder Die-attach Using Laser Flash Technique," Proc. Intersociety Conference on Thermal and Thermomechanical Phenomena in Electronic Systems (ITHERM), Vol. 1, 45-49, Las Vegas, NV, June 1-4, 2004.
17. John G. Bai, Zhiye (Zach) Zhang, Jesus Noel Calata, Guo-Quan Lu, D. P. H. Hasselman, "Determination of the Interfacial Thermal Resistivity by Finite Element Modeling of the Flash Measurements, Proc. Intersociety Conference on Thermal and Thermomechanical Phenomena in Electronic Systems (ITHERM), Vol. 1, 389-393, Las Vegas, NV, June 1-4, 2004.

18. Zhiye Zhang, Jesus Noel Calata, John G; Bai, Guo-Quan Lu, “Nanoscale Silver Sintering for High-Temperature Packaging of Semiconductor Devices, “ presented at 2004 TMS Annual Meeting & Exhibition, March 14-18, 2004.
19. G. Bai**,** J. Calata, G-Q. Lu, “Comparative Thermal and Thermomechanical Analyses of Solder-Bump and Direct-Solder Bonded Power Device Packages Having Double-Sided Cooling Capability, “ Presented at 2004 APEC.
20. Jesus N. Calata, Guo-Quan Lu, Carlos T. A. Suchicital, “ Multifunctional Ferroelectric-Ferrite Nanocomposite Material for Integrated Passive Components,” Proceedings of 2005 Annual Power Electronics Conference, Virginia Tech, Blacksburg, VA, pp 13-19.
21. John G. Bai, Zach Z. Zhang, Jesus N. Calata, Guo-Quan Lu, “Characterization of Low-Temperature Sintered Nanoscale Silver as a Novel Power Device Interconnect Material,” Proceedings of 2005 Annual Power Electronics Conference, Virginia Tech, Blacksburg, VA, pp 181-185.
22. Jesus N. Calata, John G. Bai, Xingsheng Liu, Sihua Wen, and Guo-Quan Lu Three-Dimensional Packaging for Power Semiconductor Devices and Modules, Transactions on Advanced Packaging (accepted).